UNIVERSITY OF CALIFORNIA, SAN DIEGO

Assessment, Analysis, and Applications of Geomagnetic Paleointensity for 0-2 Ma

A dissertation submitted in partial satisfaction of the
requirements for the degree Doctor of Philosophy
in
Earth Sciences

by

Leah B. Ziegler

Committee in charge:

Catherine Constable, Chair
Catherine Johnson
Guy Masters
Dimitris Politis
Lisa Tauxe

2011

The dissertation of Leah B. Ziegler is approved, and it is acceptable in quality and form for publication on microfilm:

_____

_____

_____

_____

_____

Chair

University of California, San Diego

2011

In thanksgiving for my parents, brave, wise.

In thanksgiving for my children, genuine, jubilant.

In thanksgiving for my husband, loving, dear.

In thanksgiving to the Creator, for the world without and within.

TABLE OF CONTENTS

LIST OF FIGURES

LIST OF TABLES

ACKNOWLEDGMENTS

I am grateful to my doctoral committee, many of whom are my co-authors and collaborators, for their support of me and their role in this body of work. I admire them as amazing scientists. My advisor Cathy Constable has been an excellent teacher and mentor, and I appreciate the work she put in to making this dissertation happen and helping make me a scientist. I am also grateful for her patience with me as I took multiple leaves during my tenure to grow my family and maintain a work-life balance. Catherine Johnson also served as an advisor to me for the early part of my graduate studies, before her subsequent move. I had many fruitful discussions with her and lessons from her. She, even when far away, had an active interest in my science, my career, and in helping me become a part of the greater scientific community. Lisa has also been instrumental as a collaborator, taken me along for paleomagnetic field work experience, and additionally has put much time and effort into creating community amongst the numerous paleomag/geomag scientists at SIO by organizing group meetings and other interactions which I have appreciated and benefited from. Guy I am grateful to for being the first to show me, in Earth Science 103, that Earth's interior is a dynamic, amazing place. He also advised my undergraduate research pursuits which eventually led to my decision to pursue a graduate degree. My outside committee member, Dimitris, taught me in a useful statistics class, and has been available, punctual, and positive in all his duties on my committee (thanks for taking the trips down to SIO!)

The community at SIO has been supportive as well. There are pretty much too many people to count or name. I am grateful to Miriam Kastner for giving me my first job at SIO while I was an undergrad, which included two fun and educational research cruises. I am grateful to Frank Vernon and his group for an enjoyable and educational work experience after undergrad. The student body at SIO is pretty awesome, and in my 12 years at SIO I have met and loved more of them I can name here. I would specifically thank my officemates & barnyard-mates

through the years (Robin, Meng, Danny, Sylvain, Urska, Lindsay, Valerie, Ashlee, Xiaowei, Laura, and Judy G.) for all the work and fun we shared. I have had useful discussions and good times with fellow students in geomag. and paleomag. including Lindsay, Joseph, Kristin, Roi., Julie B., and Mitra, among others. I thank Cheryl and Hubert for the opportunity they gave me in my final year to be a part of the SIO GK-12 program, where I greatly enjoyed and benefited from my educational/outreach adventures with Paula, Dave, and Ryan. I am grateful to Peter S., a skilled educator as well as scientist, for having me as a T.A. Thank you Debi Kilb for the many ways you've supported me, and for so many happy work-related and non-work-related memories. Thank you to Sofia Akber for mentoring and for the much used mini-fridge in my office. Thank you to Dave Stegman for mentoring, and thank you Stegman hottub for helping me relax during the stressful last leg of my phD work. Thanks to Robert for several hours of aid formatting my dissertation.

I am blessed with a loving and supporting family. My parents are not only encouraging and supportive, but are themselves truly inspirational role models to me. I am motivated by their examples of dedication, will, generosity, contemplativeness, faith, and more. Thank you Angie and Matt for being awesome. Thank you Rich for being awesome as well.

I am especially grateful for my husband Jon, who long before he was my husband was my best and most loyal, supportive friend. Thank you for being my physics study group in college, and for continuing to be my personal calculator when I'm too lazy to punch in numbers. Thank you for being an excellent father to our children and life partner to me. Thank you Gabe and Danni Lu for hugs, kisses, smiles, memories, and for all the meaning and love you add to my life, which inspires and motivates me.

Chapter 2, in full, is a reprint of the material as it appears in L. B. Ziegler, C.G. Constable and C. L. Johnson (2008), Testing the robustness and limitations of 0-1 Ma absolute paleointensity data, Physics of Earth and Planetary Interiors.

The dissertation author was the primary investigator and author of this paper. The dissertation author was the primary investigator and author of this paper.

Chapter 3, in full, is a reprint of the material as it appears in L. B. Ziegler, C.G. Constable, C. L. Johnson, and L. Tauxe (2011), PADM2M: A Penalized Maximum Likelihood Model of the 0-2 Ma Paleomagnetic Axial Dipole Moment, Geophysical Journal International. The dissertation author was the primary investigator and author of this paper.

Chapter 4, in full, has been submitted for publication to Earth and Planetary Science letters as: L. B. Ziegler and C. G. Constable, Asymmetry in growth and decay of the geomagnetic dipole. The dissertation author was the primary investigator and author of this paper.

VITA

2002	B.S., Physics with Earth Science specialty, *cum laude*, University of California, San Diego
2002-2004	Staff Research Associate Scripps Institution of Oceanography, University of California, San Diego
2004-2010	Graduate Student Researcher Scripps Institution of Oceanography, University of California, San Diego.
2010	Teaching Assistant University of California, San Diego.
2010-2011	NSF GK-12 Fellow Scripps Institution of Oceanography, University of California, San Diego.
2011	Ph.D., Earth Sciences Scripps Institution of Oceanography, University of California, San Diego.

PUBLICATIONS

L. B. Ziegler and C. G. Constable (*submitted*), Asymmetry in growth and decay of the geomagnetic dipole. *Earth Planet. Sci. Lett.*

Smith-Boughner, L.T., Ziegler, L and Constable, C. (*submitted*), Changing pattern of geomagnetic intensity variations in a 12 My record from the Oligocene with inconvenient gaps. *Phys. Earth Planet. Int.*

L. B. Ziegler, C.G. Constable, C. L. Johnson, and L. Tauxe (2011), PADM2M: A Penalized Maximum Likelihood Model of the 0-2 Ma Paleomagnetic Axial Dipole Moment. *Geophys. J. Int.*, **184**, 1069-1089. doi: 10.1016/j.pepi.2008.07.027

L. B. Ziegler, C.G. Constable and C. L. Johnson (2008), Testing the robustness and limitations of 0-1 Ma absolute paleointensity data. *Phys. Earth Planet. Int.*, **170**, 34-45.

PRESENTATIONS

Ziegler, L.B., C. G. Constable, (2011) *upcoming*. Maximum likelihood modeling of paleomagnetic axial dipole moment: insights and applications, IUGG July 2011 meeting, Melbourne. *invited talk*

Ziegler, L.B., C. G. Constable, (2009) An examination of dipole moment variations for 0-2 Ma. Eos Trans. AGU, 90(52), Fall Meet. Suppl., Abstract GP32A-07.

Ziegler, L.B., C. G. Constable, C. L. Johnson, L. Tauxe, (2009). A time-varying model of paleomagnetic axial dipole moment for 0-2 Ma. Geological Society of America Abstracts with Programs, vol. 41, no. 7, p. 47. *invited talk*

SELECTED POSTER PRESENTATIONS

Ziegler, L. B., D. Van Dusen, R. Benedict, P. R. Chojnacki, C. L. Peach, H. Staudigel, C. G. Constable, G. Laske (2010). A Solid Earth educational module, co-operatively developed by scientists and high school teachers through the Scripps Classroom Connection GK12 Program, presented at 2010 Fall Meeting, AGU, San Francisco, Calif., 13-17 Dec.

Smith, L.T., Constable, C. G., Ziegler, L. , (2010). A Re-evaluation of an 11 Myr record of geomagnetic intensity variations with inconvenient gaps. Study of the Earths Deep Interior (SEDI) 2010 Meeting. Santa Barbara, CA, USA

Korte, M.; Constable, C.; Holme, R.; Donadini, F.; Frank, U.; Ziegler, L. (2010): A geomagnetic field model for the past 10 kyrs. Study of the Earths Deep Interior (SEDI) 2010 meeting. Santa Barbara, CA, USA.

Ziegler, L., C. G. Constable, C. L. Johnson, L. Tauxe, (2008). PADM2M: A time-varying model of Paleomagnetic Axial Dipole Moment for 0-2 Ma. Eos Trans. AGU, 89(53), Fall Meet. Suppl., Abstract GP21A-0774.

Ziegler, L., C. G. Constable, C. L. Johnson, (2007). Robustness and limitations of 0-1Ma absolute paleointensity data. Eos Trans. AGU, 88(52), Fall Meet. Suppl., Abstract GP43A-093.

Ziegler, L.B., C. G. Constable, C. L. Johnson, (2006). A Statistical Assessment of 0-1 Ma Absolute Paleointensity Data. Study of the Earths Deep Interior (SEDI) 2006 meeting. Prague, Czech Republic.

HONORS AND AWARDS

Summer Undergraduate Research Fellowship, SIO - UCSD (2001)
Phi Beta Kappa (2002)
Regents Fellowship, SIO - UCSD (2004-2005)
NSF GK12 Fellow (2010-2011)
NSF Postdoc Fellow (2011-)

ABSTRACT OF THE DISSERTATION

Assessment, analysis, and applications of geomagnetic paleointensity for 0-2 Ma

by

Leah B. Ziegler

Doctor of Philosophy in Earth Sciences

University of California, San Diego, 2011

Professor Catherine Constable, Chair

Earth's magnetic environment is dominated by its mainly dipolar internally generated magnetic field. The ancient field has permanently magnetized surface rocks and sediments, and these materials yield information about the field direction and strength through time. I explore recently compiled databases of paleomagnetic field intensity to assess uncertainty and bias in the data, create time-varying models of paleomagnetic axial dipole moment, and constrain field generation processes. First, I examine the statistics of absolute paleointensity data for 0-1 Ma. Virtual axial dipole moments (VADMs) from lavas are on average about 10% higher and show greater dispersion than those from archeological materials. Combining data from all igneous sources reveals an apparent bimodality in the VADMs probability density function. An analysis of stochastic models of the geomagnetic field spectrum demonstrate that the bimodality likely arises from long term changes in field strength.

Both absolute and relative paleointensity data and a new penalized maximum likelihood approach are used to construct PADM2M, a time-varying model for Paleomagnetic Axial Dipole Moment (PADM) over the past 2 million years. PADM2M has a lower mean than existing VADM reconstructions but has similar long-period variability. The average axial dipole moment over 0-2 Ma is 53 ZAm^2 with a standard deviation of 15 ZAm^2. The Brunhes chron average (62 ZAm^2) is higher than for earlier epochs of the Matuyama chron (48 ZAm^2). PADM2M

is used to study rates of change over the past two million years revealing that for periods longer than about 25 ky there is a clear asymmetry in the statistical distributions for growth versus decay rates of the dipole strength. At 36 ky period, average growth rate is about 20% larger than the decay rate, and the field spends 54% of its time decaying, but only 46% growing. These differences are not limited to times when the field is reversing, suggesting that the asymmetry is controlled by fundamental physical processes underlying all paleosecular variation. Finally, I use these techniques to make regional models of axial dipole moment (RADMs) based on geographically clustered data. These have similar long period behavior, but some major differences, especially around geomagnetic excursions.

Chapter 1

Introduction

1.1 Preface

The deep interiors of Earth and other planetary bodies are hidden forever from direct observation. All knowledge of these depths are gained through indirect geophysical techniques which measure surface observables and interpret them in terms of their source processes at depth. Churnings of molten iron in Earth's outer core layer almost 2900 kilometers below the surface, with some influences from the solid metal inner core, give rise to a strong, long-lived, distinctive magnetic field surrounding the planet.

Although knowledge of the Earth's magnetic field core source wouldn't come until the mid- to late 20th century, William Gilbert (1544-1603) was able to establish that the Earth's magnetic field was internal, and that it was dipolar in nature (like a bar magnet's, see figure 1.1). In the following centuries direct observations of primarily field direction were made both for scientific purposes and for practical, applied purposes such as navigation. These lent more details to the magnetic field description, including the idea that the magnetic poles (not aligned perfectly with the Earth's rotational poles) were not static, but changed with time.

Not only is the magnetic field measurable at Earth's surface today, it has imprinted iron-bearing rocks throughout Earth's history, leaving an accidental

record of magnetic field characteristics and changes over the ages. The permanent magnetization imparted on rocks, sediments, and other materials by the Earth's magnetic field through several natural mechanisms is referred to as a Natural Remanent Magnetization (NRM). The field of paleomagnetism studies the ancient magnetic field captured in the rock record by various measurements of NRM (see Tauxe (2005); Merrill (2007)). It has proven useful for many applications related to uncovering Earth history.

Early 20th century studies in paleomagnetism focused on paleofield directions and found that occasionally and irregularly, the north and south magnetic poles switched. With a mid-20th century rise in radiometric dating techniques, paleomagnetic studies became more abundant, and through their efforts (e.g. Hospers (1951)), a chronology of 'polarity reversals' was thoroughly mapped out. Again magnetic field observations proved to be a useful tool: the mapping of the polarities of sea-floor NRM led to strong evidence to support plate tectonics theory (Vine and Matthews, 1963) and further to reconstruct plate motions. The growing body of observations was also establishing the very dynamic nature of the field.

In parallel to these efforts in the early to mid 20th century, theorists were investigating the nature of the source of the geomagnetic field. Larmor (1919) suggested that the dynamic nature of the field meant that the internal source of Earth's magnetic field was generated by fluid motions in the internal Earth. By the 1950s theoretical dynamo mechanisms established the possibility of a geodynamo in the core (see e.g. Jones (2007)), and by 1995 the first computer-generated model of dynamo action made from magneto-hydrodynamics equations (Glatzmaier and Roberts, 1995).

Recent efforts flesh out our understanding of ancient magnetic field fluctuations - referred to as paleosecular variation, or PSV - through the increased measurements of paleofield intensity, as well as direction. The picture painted by paleointensity shows an ever-changing field, with both short term and long term growth and decay. The results of recent paleomagnetic field intensity studies un-

derscore the dynamic nature of the Earth's magnetic field, and have led to new constraints and more detailed understandings of the core processes responsible for field generation.

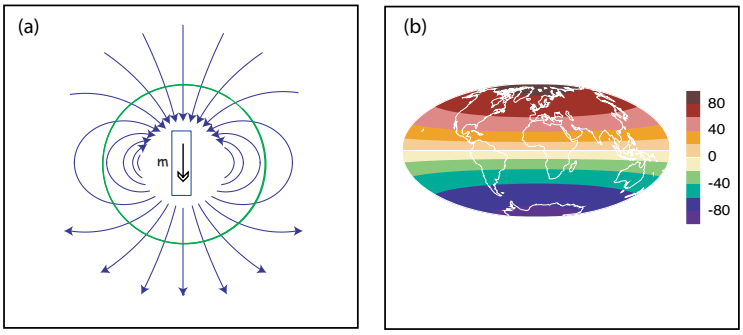

Figure 1.1: (a) Illustration of magnetic lines of force for a dipole field surrounding a bar magnet source. (b) Illustration of vertical field component at the surface of the earth for an internal dipole source, with color contours showing field magnitude. Positive and negative values denote lines of force pointing toward or away from the surface respectively (see (a)). Adapted from (Tauxe, 2005)

1.2 Motivations for this work

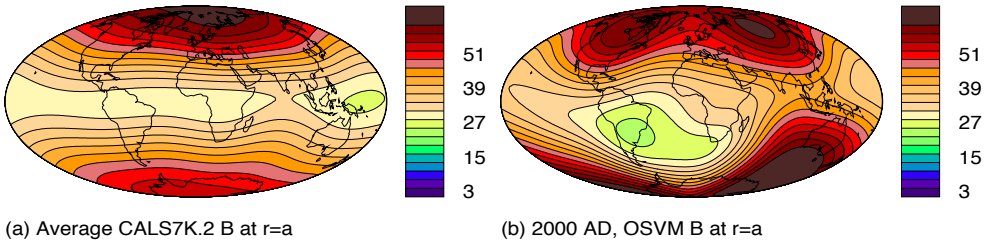

Figure 1.2: (a) Scalar magnetic field at Earths surface in μT for the average of the CALS7K.2 model over the 0-7 ka time interval, and (b) from Olsen's (2002) Oersted secular variation model, OSVM. Reproduced from Constable (2007)

The magnetic field is a shield, protecting life on Earth from potentially harmful solar wind radiation. The magnetic field is currently stronger than average, sheltering a growing number of satellites in an amply large region of protection

called the magnetosphere. However, regional features of the field, which depart from the globally dominant dipole field, include some regions of low field strength such as the south Atlantic anomaly seen in figure 1.2(b) over South America and the south Atlantic ocean. These regions pose greater hazard to spacecraft and satellites in particular. The evolution and longevity of such features are a relevant topic for this technologic age. The modern field is well measured by satellite and land based observatories, but must be contextualized through paleomagnetic studies of the ancient field. Understanding of the field evolution over millions of years can lead to better estimates of potential hazards related to geomagnetic field fluctuations.

Also, the record of magnetic field behavior is a crucial key to understanding deep earth processes and ancient Earth development. As more data become available on the historical and ancient field and its (paleo)secular variation, core flow and core evolution studies have made strides in describing the hidden workings of the deepest layers of our Earth.

Yet much progress remains to be made in understanding the ancient magnetic field. Data are comparably plentiful for recent ages, and become scarcer as we look further back in time. For the most recent few centuries direct observations of field intensity and direction are recorded and can be exploited for magnetic field and core studies. Beyond that we rely on the natural remanent magnetization of rocks, sediments and archeologic objects for indirect observations.

The amount of potentially useful paleomagnetic data from a given time in Earth's history is fundamentally related to typical ages of Earth's crust. Younger surface rocks and sedimentary deposits available to be sampled and measured for paleomagnetic information are simply more plentiful, as older rocks may become buried or altered in their lifetime. Additionally, older rocks and sediments which are available at the surface for sampling are more likely to have minor alterations or episodes of re-heating and re-magnetization at points in their long lifetimes. And finally, the ages of rocks millions of years old become increasingly hard to

determine precisely.

In the last few decades, ocean drilling projects have greatly expanded the database of paleomagnetic field observations (Sager et al., 2006). Long cores of sediment represent tens of thousands to millions of years of deposition, and record magnetic field data during that same span. Whereas individual rocks, typically igneous rocks formed in volcanic eruptions, could provide only spot recordings of field strength and direction/polarity, these cores provided time series of field behavior: a rich source of new observations. These time series have additional limitations as well, as the depositional magnetization process is less understood and includes time averaging effects which need to be accounted for in interpretation of the observations.

As the amount of paleomagnetic data has been systematically increasing, several groups have undertaken efforts to compile and maintain databases for shared use by the scientific community, namely the PINT databases (e.g. Perrin and Schnepp (2004) Biggin et al. (2009)), the Geomagia50 database (Donadini et al., 2009), and the MagIC database (http:/earthref.org/MAGIC), which hosts many data related to rock magnetism and paleomagnetism, including a compilation of relative paleointensity data assembled in Tauxe and Yamazaki (2007)). Now, as these have grown to a global compilation of data, a few opportunities are ripe for taking. First, statistical investigations can be undertaken given large data sets. Additionally, comprehensive models made from the data can synthesize the individual observations into a big picture of the global axial dipole field through time.

Using paleomagnetic observations of the ancient field in these and other applications requires careful efforts to consider the many sources of error and uncertainty in these imperfect natural recorders. Uncertainties and potential biases in paleointensity determinations, along with uncertainties in their corresponding ages both need to be addressed when analyzing and interpreting the data. Research efforts examining the effects of these uncertainties are helping resolve what

can and cannot be robustly learned from these data sources given these limitations.

A primary open question to address is how dominant the dipole is over the span and resolution of the data set. That the dipole is the primary component is well established. The task at hand is to describe in greater detail axial dipole variations on million year timescales and to take preliminary steps in understanding the feasibility of recovering non-axial-dipole field details from the relatively scarce, uncertain data.

1.3 Outline

The research contributions of this dissertation are laid out in chapters 2-5. Given the above mentioned recent gains in paleointensity data and the opportunities they afford, these analyses will deal exclusively with paleointensity data.

First, I address questions related to observations of absolute paleofield intensity as recorded in igneous rocks, archeomagnetic artifacts, and submarine basaltic glasses. I create a bootstrap technique for resampling the dataset which accounts for the over-represented nature of young data to produce an estimate of mean field strength, and other statistical characteristics of 0-1 million year old paleointensities. The field intensities recorded by different paleomagnetic materials are compared.

In Chapter 3 I build a comprehensive model of paleointensity variations over the last 2 million years. A major part of this work was the development of a robust maximum likelihood inverse modeling method for use in modeling axial dipole field strength from a joint set of absolute and relative paleointensity data. This method is then applied to a large compilation of paleointensity data from the databases cited above to create the PADM2M model of paleomagnetic axial dipole moment for 0-2 Ma. Results and implications from this model are also discussed in chapter 3.

I investigate paleosecular variation on million year timescales through

analysis of the PADM2M model derivatives, in a study on the rate of change of the field. The study explores the difference between rates of field growth and rates of field decay, showing disparity between the two on average.

Finally in Chapter 5, I compare relative paleointensity data derived from sediments clustered geographically through the construction of regional paleomagnetic axial dipole models. These models are constructed with the same methods developed in Chapter 3 applied to regional (not global) relative paleointensity data. We find some some features in paleointensity distinctive to geographic regions, and attribute them to non-axial-dipole field components.

Conclusions are discussed separately in each chapter. Chapter 6 has a very brief summary of all the conclusions along with a discussion of implications of these findings for future directions of investigations.

1.4 Appendix: Brief description of geomagnetic measurement elements

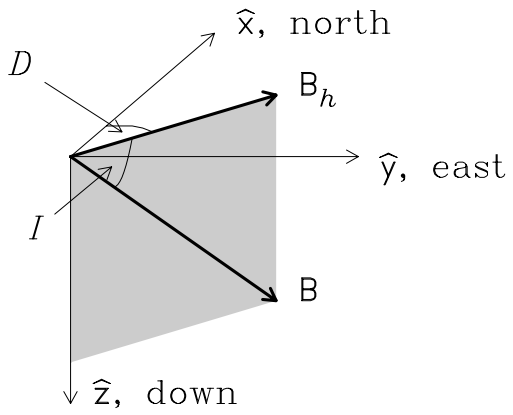

Figure 1.3: Geomagnetic elements in a local coordinate system. D is declination, I inclination, B magnetic field strength, B_h horizontal component of magnetic field. Reproduced from Constable (2007)

A magnetic field is a vector field, with magnitude and direction describing an observation of the field at a particular location. It can be measured and expressed in terms of its north, east, and down vector components (see fig. 1.3). Alternatively and most commonly, field components are expressed in terms of declination, inclination, and magnitude (intensity). The mathematical conversion between systems is not elaborated here, but a visual representation of the relationship of these systems is shown in figure 1.3.

When a geocentric axial dipole source is assumed, the field inclination and intensity vary systematically with latitude through a straightforward relation. Figure 1.1(a) illustrates a dipole source as a bar magnet at the center of a sphere (e. g. Earth) and the resulting field; figure 1.1(b) the variation of vertical field component with latitude. Under this approximation, where the magnetic pole axis is aligned with the Earth's geographic (spin) axis, the intensity at any given site is a function only of latitude and of the strength of the magnetic dipole producing the field. Global intensity are often converted into Virtual Axial Dipole Moment (VADM) data by calculating what moment aligned with the Earth's rotation axis would produce the observed intensity at the latitude of their location. Thus, geographically diverse intensity measurements which are not directly comparable due to their latitudinal dependence become directly comparable as VADM data for use in field strength studies which assume a geocentric axial dipole source.

The equation relating paleomagnetic VADM (V) to intensity (B) and co-latitude (θ) is

$$V = \frac{4\pi r^3}{\mu_0(1 + 3\cos^2\theta)^{1/2}}B$$

where μ_0 is the permeability of free space and r is the Earth's radius (see e.g. (Tauxe, 2005).

References

Biggin, A., Strik, G., and Langereis, C., 2009: The intensity of the geomagnetic field in the late-Archaean: new measurements and an analysis of the updated IAGA palaeointensity database. *Earth Planets and Space*, **61**(1), 9–22.

Constable, C., 2007: Centennial- to millennial-scale geomagnetic field variations. In *Geomagnetism*, editor M. Kono and G. Schubert, volume 5 of *Treatise on Geophysics*, 337–372. Elsevier, Amsterdam.

Donadini, F., Korte, M., and Constable, C. G., 2009: Geomagnetic field for 0-3 ka: 1. New data sets for global modeling. *Geochem. Geophys. Geosyst.*, **10**, Q06007, 10.1029/2008GC002295. doi:10.1029/2008GC002295.

Glatzmaier, G. A., and Roberts, P. H., 1995: A 3-Dimensional self-consistent computer-simulation of a geomagnetic field reversal. *Nature*, **377**(6546), 203–209.

Hospers, J., 1951: Remanent magnetism of rocks and the history of the geomagnetic field. *Nature*, **168**(4287), 1111–1112.

Jones, C., 2007: Geodynamo. In *Encyclopedia of Geomagnetism and Paleomagnetism*, editor D. Gubbins and E. Herrero-Bervera, Encyclopedia of Earth Sciences, 287–294. Springer, Dordrecht.

Larmor, J., 1919: How could a rotating body such as the Sun become a magnet? *Reports of the British Association*, **87**, 159–160.

Merrill, R., 2007: Rock magnetism. In *Encyclopedia of Geomagnetism and Paleomagnetism*, editor D. Gubbins and E. Herrero-Bervera, Encyclopedia of Earth Sciences, 871–874. Springer, Dordrecht.

Perrin, M., and Schnepp, E., 2004: Iaga paleointensity database: distribution and quality of the data set. *Physics Earth Planet. Int.*, **147**, 255–267.

Sager, W., Acton, G., Clement, B., and Fuller, M., 2006: Paleomagnetism in the ocean drilling program. *Phys. Earth Planet. Int.*, **156**(3-4), 159–161.

Tauxe, L., 2005: Lectures in Paleomagnetism. *http://earthref.org/MAGIC/books/Tauxe/2005/*.

Tauxe, L., and Yamazaki, T., 2007: Paleointensities. In *Geomagnetism*, editor M. Kono and G. Schubert, volume 5 of *Treatise on Geophysics*, 509–563. Elsevier, Amsterdam.

Vine, F. J., and Matthews, D. H., 1963: Magnetic anomalies over oceanic ridges. *Nature*, **199**(489), 947.

Chapter 2

Testing the Robustness and Limitations of 0–1 Ma Absolute Paleointensity data

Abstract

Absolute paleomagnetic field intensity data derived from thermally magnetized lavas and archeological objects provide information about past geomagnetic field behavior, but the average field strength, its variability, and the expected statistical distribution of these observations remain uncertain despite growing data sets. We investigate these issues for the 0-1 Ma field using data compiled in Perrin and Schnepp (2004), 1124 samples of heterogeneous quality and with restricted temporal and spatial coverage. We accommodate variable spatial sampling by using virtual axial dipole moments (VADM) in our analyses. Uneven temporal sampling results in biased estimates for the mean field and its statistical distribution. We correct for these effects using a bootstrap technique, and find an average VADM of $7.26 \pm 0.14 \times 10^{22} Am^2$. The associated statistical distribution appears bimodal with a subsidiary peak at approximately $5 \times 10^{22} Am^2$. We evaluate a range of potential sources for this behavior. We find no visible evidence for contamination by poor quality data when considering author–supplied uncertainties in the 0–1 Ma data

set. The influence of material type is assessed using independent data compilations to compare Holocene data from lava flows, Submarine Basaltic Glass (SBG), and archeological objects. The comparison to SBG is inconclusive because of dating issues, but paleointensity estimates from lavas are on average about 10% higher than for archeological materials and show greater dispersion. Only limited tests of geographic sampling bias are possible. We compare the large number of 0-0.55 Ma Hawaiian data to the global data set with no definitive results. The possibility of over-representation of typically low intensity excursional data is discounted because exclusion of transitional data still leaves a bimodal distribution. No direct test has allowed us to rule out the idea that the observed pdf results from a mixture of two distinct distributions corresponding to two identifiable intensity states for the magnetic field. We investigate an alternative possibility that we were simply unable to recover a hypothetically smoother underlying distribution with a time span of only 1 Myr and the resolution of the current data set. Simulations from a stochastic model based on the geomagnetic field spectrum demonstrate that long period intensity variations can have a strong impact on the observed distributions and could plausibly explain the apparent bimodality. Our 0-1 Ma distribution of VADMs is consistent with that obtained for average relative paleointensity records derived from sediments.

2.1 Introduction

Absolute paleointensity data are important constraints on our knowledge of the geodynamo. They allow the possibility of exploring how geomagnetic field strength has varied over Earth's history and are essential for providing appropriate scaling to both time-averaged and time-varying magnetic field models that extend beyond the historical record. Time varying field models on centennial and millennial time scales already exist (Jackson et al., 2000; Korte and Constable, 2005), and have proved useful for studying prehistoric secular variation, but the extension

of such models to million year time scales has not yet been accomplished. They will, however, be important in understanding low frequency field variations, and giving better context to observations of the current and historical field.

Magnetic field models, generally derived by fitting mathematical functions to globally distributed observations of field intensity and direction, are limited in spatial and temporal resolution by the quality and abundance of available data. An ideal data set would include time series of intensity and directional variations of the magnetic field at many geographically diverse locations. In reality, we have two types of data: spot recordings of absolute field intensity, inclination, and declination found from magnetized igneous rocks and archeological objects, and time series of absolute inclination variations and relative intensity and declination variations from magnetized sediment cores. Field intensity data have been particularly sparse until fairly recently, and are still less abundant than directional data. Yet, with a gathering supply of absolute paleointensity data, modeling of field intensity variations on million year timescales should be possible - especially if these data can be used in conjunction with time series of relative intensity variations derived from sediment cores.

The SINT relative paleointensity stacks (Guyodo and Valet, 1996, 1999; Valet et al., 2005), which are formed by averaging some tens of globally distributed relative paleointensity records, have already hinted at interesting features of long term field variations worth further investigation - for instance intensity lows at excursions and the proposed sawtooth paleointensity pattern near reversals (Valet and Meynadier, 1993). However, these stacks are limited in that they utilize only relative paleointensity data to create the model of field variations. The two most recent SINT curves (SINT800 and SINT2000 spanning the past 800 ka and 2 Ma, respectively) have used absolute paleointensity data to scale the SINT curves to represent absolute variations in virtual axial dipole moment (VADM), but different scaling procedures resulted in significantly different estimates of the mean VADM for the Bruhnes chron ($6 \times 10^{22} Am^2$ and $7.5 \times 10^{22} Am^2$ for SINT800 and SINT2000

respectively). The SINT curves also lack the predictive power of a mathematical model for the field: they cannot be expanded to geographic variability beyond that of an axial dipole field, cannot be downward continued to examine the field at the Core Mantle Boundary (CMB), and are not easily differentiated to show rate of change in the field.

Using paleointensity data for modeling, or even for other more basic inferences about the field is not necessarily straightforward. For example, various authors have found conflicting estimates of the mean field strength (e.g. (McFadden and McElhinny, 1982; Constable and Johnson, 1999; Selkin and Tauxe, 2000; Tauxe and Kent, 2004)). Differing estimates are often caused by including data based on variable standards of reliability (as determined by uncertainty, laboratory methods, materials used, and other factors) or which cover different age ranges. Since the process of determining paleointensities is far from standardized, with new developments still frequent in this field, the debate over what data are reliable is unlikely to be resolved soon. As mentioned above, progress still needs to be made on how to use both relative paleointensity records and absolute paleointensity data together to create time varying field intensity models. Since each type of data has different sources of noise, we need to look at each data source in detail in order to assess how they can be used together most appropriately to produce paleointensity models.

Here, we assess the current global absolute paleointensity data set to characterize its statistics and to evaluate it for its use in future modeling. We first review the data that are currently available, and some possible drawbacks of the data set. Then we use statistical techniques to test the consequences of restricting the available data based on certain criteria. We look specifically at data from 0-1 Ma, where both absolute paleointensity data and relative paleointensity data are adequately distributed in space and in time to make field intensity modeling potentially viable.

2.2 Data

A number of absolute paleointensity compilations have been made over the past few decades and subjected to detailed analyses to determine the average dipole moment, and the statistical distribution of the observations. We follow a precedent established in the 1980s (McElhinny and Senanayake, 1982; McFadden and McElhinny, 1982) when data sets for the 0-50 ka time interval were considered separately from those spanning million year time scales. For the 0-1 Ma time scale we use absolute paleointensity data derived from igneous geological materials, typically lava flows, that acquire a thermoremanent magnetization. The primary data set chosen is the PINT03 compilation (Perrin and Schnepp, 2004). To facilitate comparisons of results from different material types we use a subset of the more abundant archeomagnetic and lava data set from the 0-50 ka Geomagia50 database, and our own compilation of data from Submarine Basaltic Glass (SBG).

2.2.1 PINT03

The PINT03 database consists of 3128 globally distributed data from igneous and baked contact sources. More data have been published since this compilation, so it represents a minimum of igneous sourced data available at present. Perrin and Schnepp did not do quantitative analysis on the data compilation, citing some potential sources of biases in estimating paleointensity statistics with the currently available data (e.g., biased temporal and regional distributions of data, data quality variability) and the low density of data in time. However, for the 0-1 Ma time period there are 1124 data, and we feel that the number, temporal and spatial coverage (Figure 2.1) are sufficient to justify some quantitative analyses. Beyond 1 Ma, both absolute and relative paleointensity data are less plentiful. We also investigate the influence of some of the previously mentioned potential sources of bias on the resulting field intensity statistics.

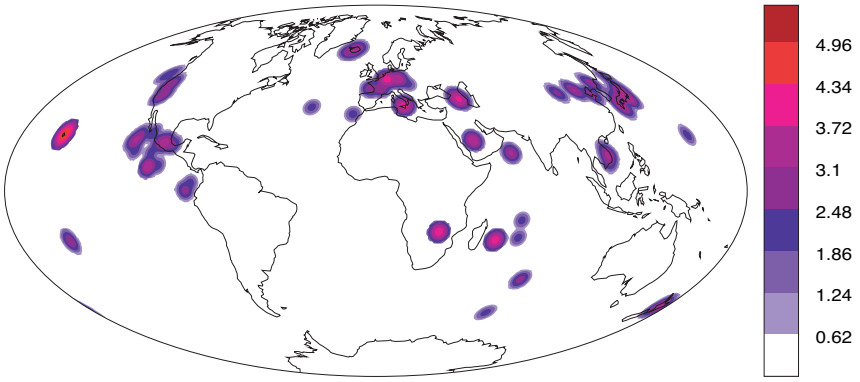

(a) 0–1 Ma Global Paleointensity Distribution

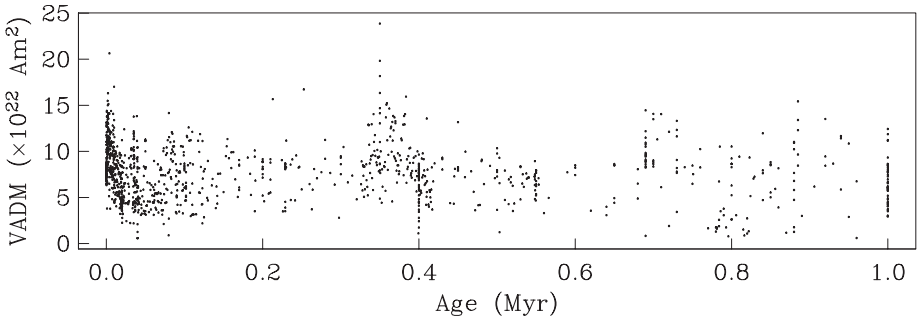

(b) 0–1 Ma Temporal Paleointensity Distribution

Figure 2.1: (a) Global distribution of 0-1 Ma absolute paleointensity plotted as a probability density function on a log scale (units of $(\times 10^{22} Am^2)^{-1}$). Red (purple) values show areas with a high (low) concentration of data. Blank (white) areas have no data. (b) Paleointensity data are converted to VADM (see text) and plotted vs. age.

2.2.2 Geomagia50

The Geomagia50 database (Donadini et al., 2006) compiles globally distributed data from both lava flows and archeological objects with ages in the range 0-50 ka. We specifically look at the time interval 0-7 ka, since data are concentrated in this range (2793 archeological data and 311 lava flow data). The PINT03 database contains data from igneous sources only. Absolute paleointensities can also be determined from archeological objects. For the purposes of evaluating the 0-1 Ma field, adding archeointensity data to the PINT03 compilation provides additional data in the small time interval over which data density is already highest.

For this reason, we stick to using only the PINT03 data compilation to evaluate the 0-1 Ma field, and only use Geomagia50 to compare paleointensity data from archeological and igneous sources. Since these two data sources have different mineralogies and cooling rates, they could potentially give different results. We also use this database as a source of 0-7 ka lava data in this comparison, as it is a more recent compilation and with more data in this time range than the PINT03 database. Figure 2.2 shows the temporal and regional distributions of data from archeological and igneous sources with ages between 0 and 7 ka, plotted in the same fashion as Figure 2.1.

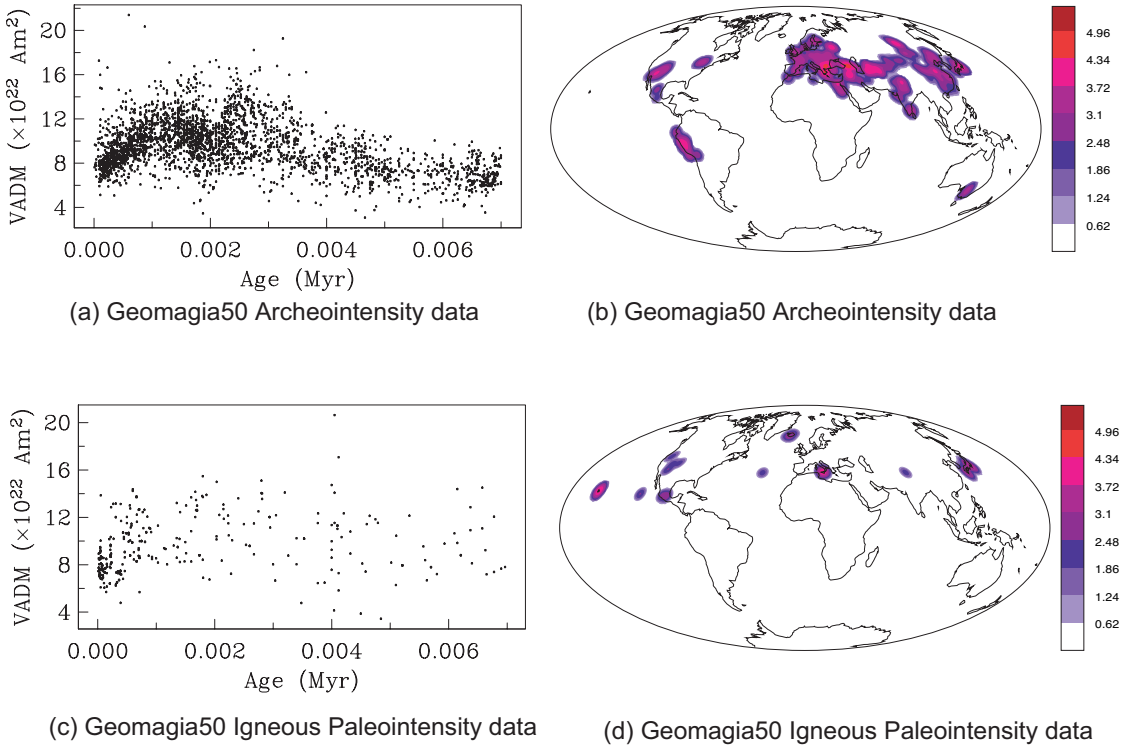

(a) Geomagia50 Archeointensity data

(b) Geomagia50 Archeointensity data

(c) Geomagia50 Igneous Paleointensity data

(d) Geomagia50 Igneous Paleointensity data

Figure 2.2: Distribution of data from the Geomagia50 database with ages of less than 7 ky. (a) and (c) show distributions in time of data from archeological and igneous sources respectively (with intensity converted to VADM). (b) and (d) show geographical distributions of data from archeological and igneous sources respectively (format as for Fig. 2.1).

Some statistical analysis has already been done using this data compilation to test the correlation of data found from differing material types and labora-

tory methods (Donadini et al., 2007). A comparison with their findings is included in our discussion.

2.2.3 Submarine Basaltic Glass

Within the category of igneous sources, we can also compare SBG data and other lava flow data. SBG has a distinct fabric and cooling history, and so could potentially provide different results than other igneous data, and has sometimes yielded average field strengths which differ from those computed from other igneous data (Selkin and Tauxe, 2000; Tauxe and Yamazaki, 2007; Heller et al., 2002; Valet, 2003). The PINT03 data set contains only a handful of SBG data, but more data can be added (i.e. (Bowles et al., 2006; Gee et al., 2000)). Before mixing these material types into a larger compilation, results obtained from the different material types should be quantitatively compared. The SBG data used in this study are a compilation of data from (Bowles et al., 2005, 2006; Carlut et al., 2004; Carlut and Kent, 2000; Gee et al., 2000; Mejia et al., 1996; Pick and Tauxe, 1993) yielding 313 data all with nominal ages less than 100 ka based on crustal ages calculated from spreading rates and distances from the ridge axis. The actual ages are likely to be much younger than 100 ka (Bowles et al., 2006), and we discuss this later.

2.2.4 Potential Drawbacks of the Data Set

Given that the Earth's magnetic field is predominantly dipolar, it is common to account for gross geographical variations in intensity data by converting to Virtual Axial Dipole Moments (VADM) (Barbetti, 1977). Temporal and spatial distributions of the PINT03 data are plotted in Figure 2.1. The global distribution is plotted as a probability density function on the globe, with higher values (indicated by the pink end of the color spectrum) indicating higher data density. The time distribution is shown by plotting VADM vs. age. Data are unevenly distributed in time, with a high concentration of young data. A bias toward Northern

hemisphere data is also clearly evident, as noted by Perrin and Schnepp (2004). Notably, over 512 data (almost half of the data set) are from Hawaii. In looking at global data sets of VADMs to calculate mean field strength, it is assumed that non-dipole components will be a source of noise, but contribute no bias in field statistics. However, if a large portion of data is from a single geographic region, the data compilation could potentially be biased toward reflecting any persistent non-dipole field components at that location (as shown by Korte and Constable (2005b)). To assess the accuracy of the assumption that the time averaged field is dipolar, we plot VADM vs. latitude (Figure 2.3), along with the mean field strength (black line) and average VADM values for 15^o latitude bins. If the dipole approximation is accurate, the time averaged VADM should be a constant, regardless of latitude. The bin averages show considerable scatter. Although this scatter could be attributed to non-dipole field effects, it is clear in Figure 2.3 that a few bins contain data from very small time ranges, which is likely the source of scatter: that is, each bin average reflects the average VADM over different time ranges.

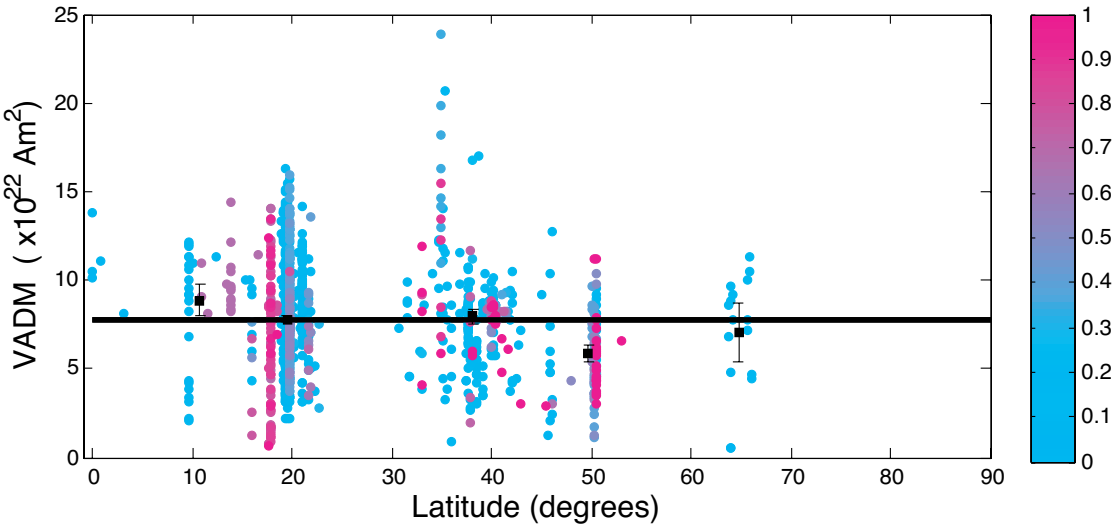

Figure 2.3: PINT03 0-1 Ma VADM data plotted by latitude, and colored to correspond to age (circles). Color scale in Ma. Black squares are mean VADM values for 15^o bins, with error bars showing 95% confidence bounds, calculated as $2\times$ standard error in the mean. Black line is the average VADM for 0-1 Ma.

Besides the uneven temporal and spatial distribution, variable quality

could also contribute to variance or bias in the currently available data set. The PINT03 database compiles all published data with no restrictions, but also contains fields of information which could be used to restrict data based on quality controls. One measure of data quality is the reported uncertainty in the paleointensity estimate, calculated as the standard deviation of the mean paleointensity of several specimens from a single cooling unit. However, paleointensity data are often only reported from a single specimen, in which case reported uncertainly is absent. Preferably, paleointensity estimates are made from more than one specimen, and have low reported uncertainty. Any reasonable restriction of this kind will significantly reduce the number of data.

Data quality can be checked or improved by employing laboratory methods which detect or minimize the potential for alteration. Paleointensity determinations could be inaccurate for this or other rock magnetic reasons. Several methods have been developed to specifically address these concerns, but debates over which methods are most appropriate still continue. Details of these topics are not discussed here; for more information see Tauxe and Yamazaki (2007) and Valet (2003). We note, however, that data obtained using the Thellier-Thellier method with pTRM checks (denoted T+ in the PINT03 intensity methods field) are often taken to be the most reliable, as they have built in heating steps which check for alteration. For this reason, we look at restricting the data by this criterion. An alternative method of guarding against data contaminated by alteration effects, the Shaw method, is not be evaluated here, because of the small number of data in PINT03 gathered using this technique.

Finally, we note that the estimated ages of paleointensity data are often poorly constrained, with large or absent age uncertainties. This can be a big issue when looking at time-varying field intensity, and can also be an issue when looking at average field strength and investigating how methods, geographic bias, and materials may influence average paleointensity determinations. When comparing paleointensities from different geographic locations, materials, and methods, these

paleointensities must be from the same time (or time span) so that differences in intensity results are not attributable to their simply sampling different field strengths.

2.3 Methods

We evaluate the 0-1 Ma absolute paleomagnetic data set with statistical methods, estimating the mean and variance as well as the probability distribution function (pdf) and empirical cumulative distribution function (ecdf). We use these properties to directly compare the original 1124 member data set with specific restricted subsets. Pdf estimation is done with an adaptive kernel method (i.e. kernel bandwidth varies with data density), using Abramsons square root law (Abramson, 1982) to determine bandwidth, as described by Silverman (1986). This non-parametric approach allows us to compare pdfs of subsets of data without imposing a potentially inappropriate parametric form. The empirical cdf (the probability that a value X will be less than or equal to x) is calculated directly from the data as a ratio of data less than or equal to x to total number of data, with linear interpolation to evaluate the function at evenly spaced values of x.

First, we need to address the uneven temporal distribution of the data. Since data concentration is heavily skewed toward young ages, our resulting statistics will be biased toward describing the recent field, instead of the 0-1 Ma field. If all paleosecular variation occurred with periods less than a few tens of kyr, it would not matter that the recent few kyr is so heavily represented, as it would not necessarily have a mean or other statistics which differed from a longer time range of data. However, long period variations are clearly evident in sedimentary relative paleointensity records (e.g. (Valet et al., 2005)). We cannot be sure that PSV with periods of longer than 1 Ma are not also occurring in the time varying field (see Discussion). Therefore, our results should be interpreted as describing the 0–1 Ma field only.

To correct for the uneven temporal distribution we use a variation of a bootstrap method (Efron and Tibshirani, 1993) to resample the original data set: we generate a set of n ages from 0-1 Ma randomly (with uniform probability) and from there choose from our original data set the paleointensity data whose ages most closely match each of the simulated ages as members of our new resampled data set. In this way, we bootstrap a distribution of n data from our original data set to create a resampled data set which is spread more evenly in time. We generate 1000 resampled sets of $n = 500$ data. Estimates of statistics do not change significantly with more than 1000 simulations (and actually converge with fewer simulations, so this is a conservative number). A mean VADM ($\bar{\mu}$) can be estimated by finding the average of the 1000 resampled means ($\bar{x}_i$). We can also calculate the standard error in the mean of $\bar{\mu}$, σ_μ. Variance $\bar{\sigma^2}$ and standard error of the variance σ_{σ^2} can be found analogously. Specifically, we calculate these statistics using:

$$\bar{\mu} = \frac{1}{k}\sum_{i=1}^{k} \bar{x}_i \tag{2.1}$$

$$\sigma_\mu = \sqrt{\frac{1}{(k-1)}\sum_{i=1}^{k} \left(\bar{x}_i - \bar{\mu}\right)^2} \tag{2.2}$$

$$\bar{\sigma^2} = \frac{1}{k}\sum_{i=1}^{k} \bar{s_i^2} \tag{2.3}$$

$$\sigma_{\sigma^2} = \sqrt{\frac{1}{(k-1)}\sum_{i=1}^{k} \left(\bar{s_i^2} - \bar{\sigma^2}\right)^2} \tag{2.4}$$

where $k = 1000$, $\bar{s_i^2}$ is the variance of a resampled distribution, and the other variables are described above. Using this method, we not only attempt to correct for the uneven temporal sampling, but we can also find a reliable estimate on the error or stability of our estimate of mean and variance.

Figures 2.4 (a) and (b) show histograms of the ages of the original 1124 data, and of one resampled data set. The resampled distribution has ages spread

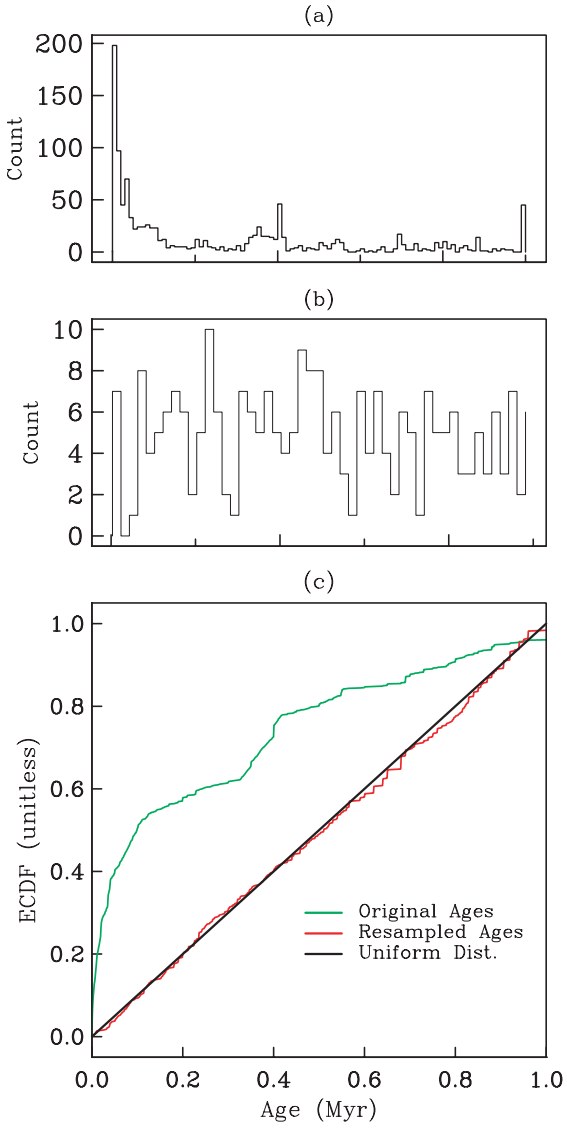

Figure 2.4: (a) Histogram showing the age distribution of the 1124 0-1 Ma data from Pint03. (b) Histogram of the age distribution of a resampled set of 500 data (see text). (c) Ecdfs of the original Pint03 0-1 Ma data set (green), a resampled set of 500 data (red), and a uniform distribution (black).

much more evenly in time. Figure 2.4 (c) illustrates this again by plotting the empirical cumulative distribution functions (ecdfs) of both data sets, along with the cdf of a uniform distribution for comparison. Since the 0-1 Ma data set has some gaps in time, we cannot truly create resampled data sets which are uniformly distributed in time. To test whether the temporal distribution of a typical resampled data set is distinguishable from a uniform distribution, we perform a Kolmogorov-Smirnov (KS) test, to quantify the difference between their ecdfs, see (Press et al., 1986). We find a KS significance level of 0.61, where the level is on a scale of 0 to 1 with small values indicating a low probability that the samples come from the same underlying distribution. This test shows that the resampled distributions are not distinguishable from a uniform distribution. This technique eliminates bias generated by the high concentration of young data. Our results, discussed below, show that resampling significantly affects our estimated mean, variance and pdf. Therefore, we use this temporal resampling in all comparisons of the original data set to subsets based on restrictive criteria to make sure differences we see are not attributable to time-sampling issues.

2.4 Results

2.4.1 0-1 Ma Field Statistics: Temporal Sampling Effects

As shown in Table 2.1, the mean VADM of the original 0-1 Ma data set is $7.71 \pm .09 \times 10^{22} Am^2$. Using our bootstrap procedure to simulate a temporally evenly distributed data set, the new estimate of the mean is $7.26 \pm 0.14 \times 10^{22} Am^2$. A t-test confirms that we can reject the null hypothesis that these means are the same at the $\alpha = .01$ level (i.e. if there were no difference, our observed difference would occur with a probability of less than .01). The lower mean is to be expected, since the procedure effectively reduces the influence of the higher than average young data. We also estimate the pdf and ecdf of the resampled data by averaging the 1000 distributions of data to find a mean distribution and 95% confidence

bounds. These are plotted in Figure 2.5 (a) and (b), respectively. Looking at the estimated distributions in comparison to the originals, the significant changes can be identified by noting where the original distribution (black) lies outside the confidence bounds we have estimated (red dashed). In Figure 2.5 (a), some of the high VADM tail seen in the original distribution is absent in the mean resampled distribution. On the other end, the resampled data pdf shows more low VADM values. There is a sidelobe in the pdf around $5\times10^{22}Am^2$ which is not removed by accounting for the uneven temporal distribution.

2.4.2 An abundance of Hawaiian data

The spatial distribution of data is limited with a high concentration of northern hemisphere data. The distribution is too uneven to allow us to correct for its inadequacies as we have done for the temporal distribution. However, as mentioned above, 512 out of the 1124 data are from Hawaii. Only 4 Hawaiian data are older than 0.55 Ma. In the 0-0.55 Ma age range, 508 out of 944 data are from Hawaii. For this reason, we investigate the influence of Hawaiian data by comparing data from Hawaii only, data from everywhere but Hawaii, and the combined data set (Hawaiian and non-Hawaiian data) over the time range 0-0.55 Ma. We again simulate 1000 distributions of 500 data points for each data set. Results are shown in Table 2.1 and Figure 2.5 (c) and (d).

The bootstrapped mean for the Hawaiian data is slightly lower than that of the combined data set. However, the combined 0-0.55 Ma data set has a mean virtually identical to the data set without any Hawaiian data. Though at first glance it seems unexpected that the combined data set has a mean very similar to the non-Hawaiian data set despite the fact that the Hawaiian data has a lower mean than the non-Hawaiian data, this is clarified by looking at the medians for these distributions (which are often more robust estimates for the expected value of distributions which are non-gaussian). The estimated median of the combined data set ($7.61\times10^{22}Am^2$) falls between the median of the Hawaiian data (7.35

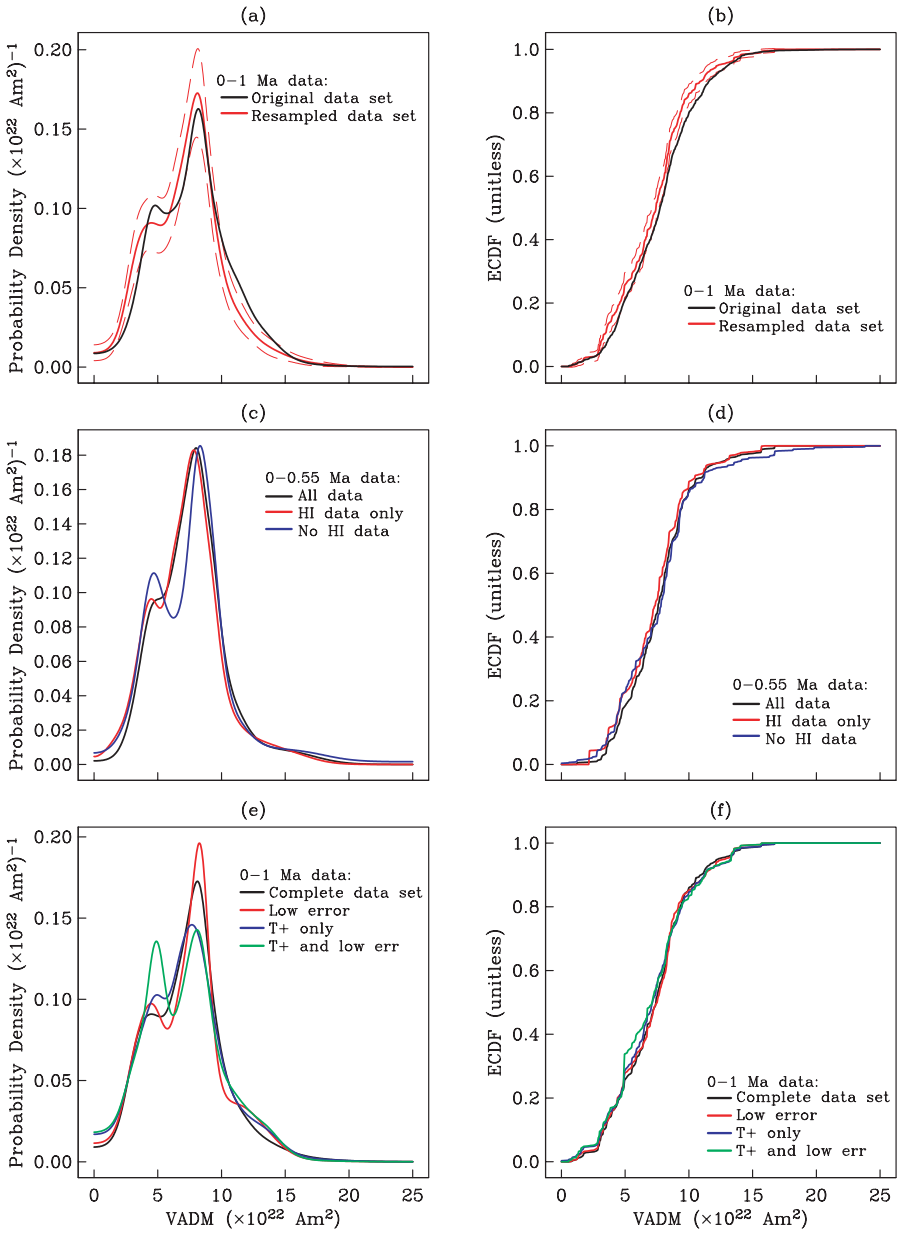

Figure 2.5: (a) Pdf of the original 0-1 Ma Pint03 data set (black), the mean pdf of the 1000 pdfs of the resampled (temporally evenly distributed) data sets (red), and 95% confidence bounds of the mean pdf (red dash). (b) Ecdfs of original and resampled data with same color coding as (a). (c) and (d) Mean pdfs and ecdfs respectively for the complete 0-0.55 Ma data set (black), Hawaiian data only (red), and all locations except Hawaii (blue). (e) and (f) Mean pdfs and ecdfs respectively for the complete 0-1 Ma data set (black), data with reported errors less than 20% or 5μT (red), data found using versions of the Thellier method with pTRM checks (blue), and data which are both reported to have low errors and which are found using Thellier methods with pTRM checks (green).

$\times 10^{22} Am^2$) and the median of the non-Hawaiian data set (7.80 $\times 10^{22} Am^2$), as one would expect, and t-tests show that we cannot reject the null hypotheses that the means of the subsets are the same as the mean of the combined data set. This indicates that little bias is introduced to the combined data set by having such an abundance of data from one small region. However, the medians of the Hawaiian data and non-Hawaiian data are significantly different from each other ($\alpha = .02$), which could be due to persistent non-dipole field contributions at the Hawaii location. It is difficult to quantify how much of the small but statistically significant difference in mean and median values between these two subsets is due to non-dipole field components and how much of it is a time sampling issue, since simulating uniform time distributions with these smaller data sets becomes increasingly difficult (see Discussion).

Mean pdfs and ecdfs from the resampled distributions are plotted in Figure 2.5 (c) and (d). They are not significantly different from each other, except for a more pronounced sidelobe in the 'No Hawaii' data set. We do not show the confidence bounds in these figures for ease of viewing, but they overlap, confirming that differences among these 3 data sets are insignificant.

2.4.3 Restricting Data Quality

We next investigate whether higher quality data has different properties from the complete 0 - 1 Ma data set. As we already noted, there is still considerable debate over how to judge data reliability, and this is further complicated by the heterogeneous reporting of data and uncertainties. For now, we assess the influence of restricting the data based on reported error (reported errors must be either less than 20% or less than 5 μT for each result, with each result and reported uncertainty supposed to represent a cooling unit of a determined age), separately restrict the original data set to include only data produced using the Thellier-Thellier method with pTRM checks, and finally apply both of these requirements. Each subset of data spans the time range 0-1 Ma. Again, we resample

1000 distributions of 500 data points to estimate statistics and pdfs for each data set. Results are shown in Table 2.1 and Figure 2.5(e) and (f).

Comparing $\bar{\mu}$ for each of these subsets to the $\bar{\mu}$ of the original data set, t-tests show we cannot reject the null hypothesis that they are the same ($\alpha > .05$ in each case). This result indicates that although including less reliable data in our estimates of field intensity statistics is not desirable, it does not significantly bias the results.

Pdfs for the various groups of observations are similar and all include the sidelobe seen in the complete data set, although the amplitude of the sidelobe varies for each data set. The subset of data which satisfy both the low error and Thellier-Thellier method with pTRM check criteria (green distribution in Figure 2.5(e), (f)) has a sidelobe with amplitude almost equal to that of the main peak. In this case, the exaggeration of the sidelobe is an artifact of our resampling procedure, which attempts to resample evenly in time, but runs into problems if large age ranges have little or no data. We find that there is a temporal gap for data meeting these strict requirements at around 0.6 Ma, and that on either side of the gap are data with values of about $5 \times 10^{22} Am^2$. Our procedure picks these two data points (on the edges of the gap) to represent the intensity over the entire time range of the gap in data, leading to an artificially large sidelobe at around $5 \times 10^{22} Am^2$. This issue is also evident in the lack of smoothness in the ecdf at the same VADM value: the sharp jump most likely is a result of a particular point or two being chosen many times for each resampled distribution. The effect this would have on the mean in this instance would be to bias it low (since $5 \times 10^{22} Am^2$ is a lower than average VADM). Indeed, the mean of the highly restricted data set is lower (though not significantly lower) than that of the complete data set and the subsets of data restricted based on method or reported error alone. Thus, the small differences between data sets in the investigation of using quality criteria restrictions reflect the limitations of the specific temporal sampling available rather than significant differences among the data sets themselves.

Table 2.1 Statistics of data sets used in this study.

	#	Mean	Var	$\bar{\mu}$	σ_μ	$\bar{\sigma^2}$	σ_{σ^2}
All 0-1 Ma	1124	7.71	9.38	7.26	0.14	8.58	0.57
Low err	783	7.67	8.29	7.23	0.14	8.77	0.55
T+ only	874	7.60	9.59	7.16	0.14	9.73	0.63
T+ and low err	574	7.60	9.07	7.06	0.14	9.73	0.57
All 0-0.55 Ma	944	7.84	8.92	7.64	0.12	7.41	0.57
HI 0-0.55 Ma	508	7.84	8.43	7.29	0.13	7.57	0.57
No HI 0-0.55 Ma	436	7.83	9.64	7.68	0.15	11.41	1.18
Arch. 0-7 ka	2793	9.54	5.07	8.74	0.10	5.00	0.36
Lava 0-7 ka	311	9.56	6.02	9.77	0.14	6.41	0.55
Lava 0-7 ka cr^*	311	8.31	4.55	8.50	0.13	4.87	0.42
SBG 0-100 ka**	313	8.33	7.74	-	-	-	-
SBG 0-10 ka**	158	9.40	2.61	-	-	-	-

Table 2.1: # is the number of data in data set, Mean and Var are of the original data sets, $\bar{\mu}$ is the mean mean value of the bootsrapped distributions, σ_μ is the standard error in the mean, $\bar{\sigma^2}$ is the mean variance of the bootstrapped distributions, σ_{σ^2} is one standard error of the mean variance. cr^* denotes the lava data after being adjusted for a hypothetical 15% high bias due to cooling rate. ** denotes ages calculated as crustal ages (see text)

2.4.4 Influence of material type

Archeological vs. Lava data

Compared to intensity estimates from igneous sources, archeointensity data may be more reliable. The mineralogy of archeological objects is generally more uniform (at least within site) than for igneous sources, and the magnetic carrier is more likely to be hematite in archeological objects, and so less prone to alteration during lab procedures. Additionally, archeological objects may cool more quickly (and uniformly within site) than lava flows, and so yield results less biased by large differences between the natural and lab cooling rates.

Here, we compare archeointensity data to paleointensities derived from igneous sources over the age range 0 - 7 ka (as compiled in Geomagia50). There are only 311 igneous paleointensities in this time range, compared to 2793 archeointensity data . Despite this, some meaningful comparisons can be made. Interestingly, the simple averages of VADMs of the two original data sets (without temporal resampling done) are almost identical. However, the picture changes after compensating for the uneven temporal sampling yielding a $\bar{\mu}$ of $8.74\times10^{22}Am^2$ for the archeointensity data set - significantly lower than the $9.77\times10^{22}Am^2$ obtained for the lava data set. We note that we have used $n = 300$ in the resampled igneous data distributions (instead of $n = 500$) due to the small size of the original data set. Igneous data have a higher variance both before and after correction for temporal sampling.

The mean pdfs and ecdfs of the corrected bootstrapped distributions (Figure 2.6 (a) and (b)) illustrate these differences. The igneous data pdf (black curve in Figure 2.6(a)) is broader than the archeointensity pdf, and is offset to higher values of VADMs. Similarly the ecdfs in (b) (archeological data set in red, igneous in black) show the significant difference between the two data sets. This large difference merits further investigation (see Discussion).

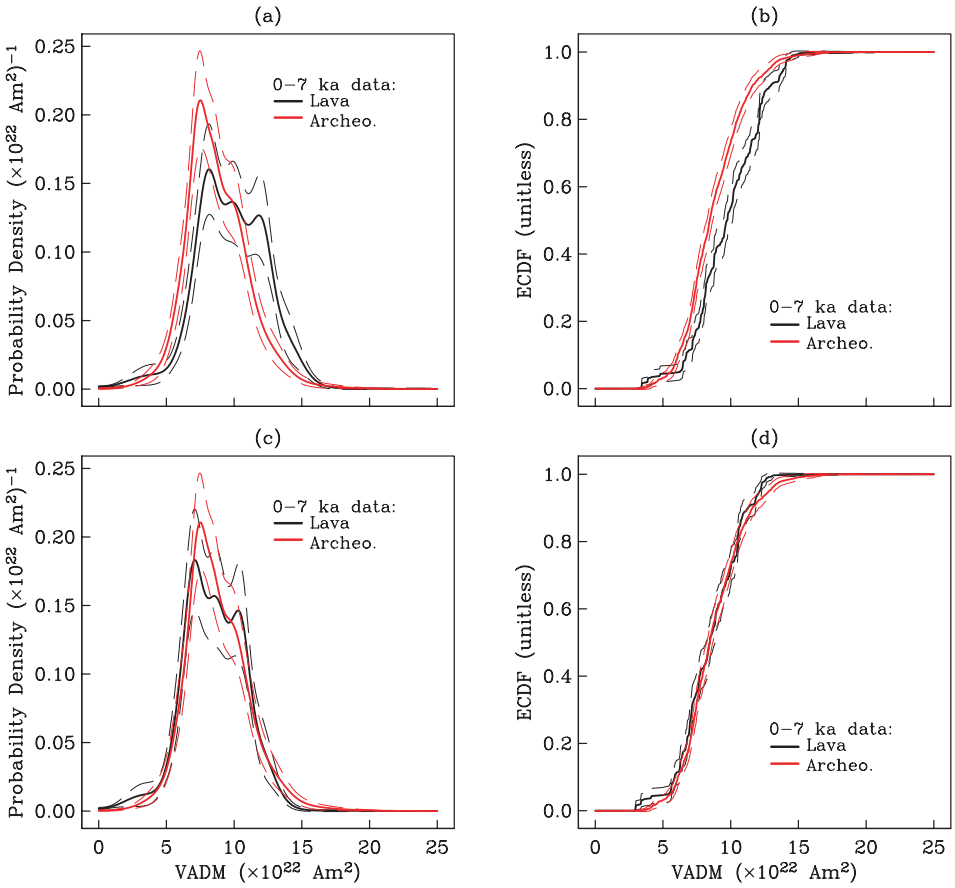

Figure 2.6: Mean pdfs (a) and ecdfs (b) (as in Fig. 2.5) for 0-7 ka archeointensities (red) and paleointensities from lava flows (black). (c) and (d) Mean pdf and ecdf respectively for archeointensities (red) and *adjusted* paleointensities from lava flows (black), for data whose ages of span 0-7 ka. Adjusted paleointensities calculated by reducing the actual paleointensities to account for a hypothetical 15% bias high due to lack of cooling rate corrections(see Discussion section).

Submarine Basaltic Glass

Some discussion has occurred about the reliability of SBG data (Heller et al., 2002; Valet, 2003; Tauxe and Yamazaki, 2007). Here, we attempt a comparison of SBG data to other igneous data and to archeointensity data over the same age range. However, this is not straightforward, as young SBG data are difficult to date. Many SBG data in our compilation have age estimates based on distance from the ridge axis (Mejia et al., 1996; Gee et al., 2000), so that the age corresponds to the crustal age, but is not necessarily the age of the uppermost lava

flow which is being sampled. Bowles et al. (2006) derived ages using correlation with global paleointensity variations, but for this study we have recalculated these ages based on distance from the ridge axis and spreading rate to have an independent age estimate. Some studies have only restrictions on age (i.e. "less than 10 ka"), with no exact ages reported (e.g. (Carlut et al., 2004; Bowles et al., 2005). Bowles et al. (2006), using paleointensities and geological features, showed that larger flows from the ridge axis and/or off-axis volcanism can lead to very young data ($<$ a few ka) derived from locations kilometers from the ridge. In this case, ages estimated by calculating crustal age based on spreading rates can be off by tens of kiloyears. Nominally, our SBG compilation ranges in age from 0-100 ka. However, the results of Bowles et al. (2006), indicate it is possible that the upper end of the range is much younger. To complicate the issue further, we cannot use our technique to resample evenly in time since the data ages are so uncertain. This is a real problem with the SBG compilation since data are heavily concentrated along the ridge axis.

To allow for these large uncertainties, we compared the SBG compilation to other data types in several age ranges, including lava data for 0-100 ka, 0-40 ka, and to lava data and archeointensities of ages 0-3 ka. By far, the best match in distributions for the SBG data is to compilations of paleo- and archeointensity data of 0-3 ka (Figure 2.7(a)) (note that again, the subaerial lava data show some high paleointensites not seen in archeointensity data, although the effect is not as pronounced in this smaller data set). This supports the idea that data within a couple of kilometers of the ridge axis (which comprise the majority of this data compilation) are only a few thousand years old, rather than sharing the crustal age of 20 ky. Data from Gee et al. (2000) and Bowles et al. (2006) are plotted vs. distance from ridge axis (Figure 2.7(b)). These account for 237 out of 313 of the SBG data in our compliation. Comparing the pattern of SBG paleointensities vs. distance from the ridge axis to a plot of paleointensities (from other lava sources) vs. age in Figure 2.7(c), the SBG paleointensities vs. distance plot looks like a

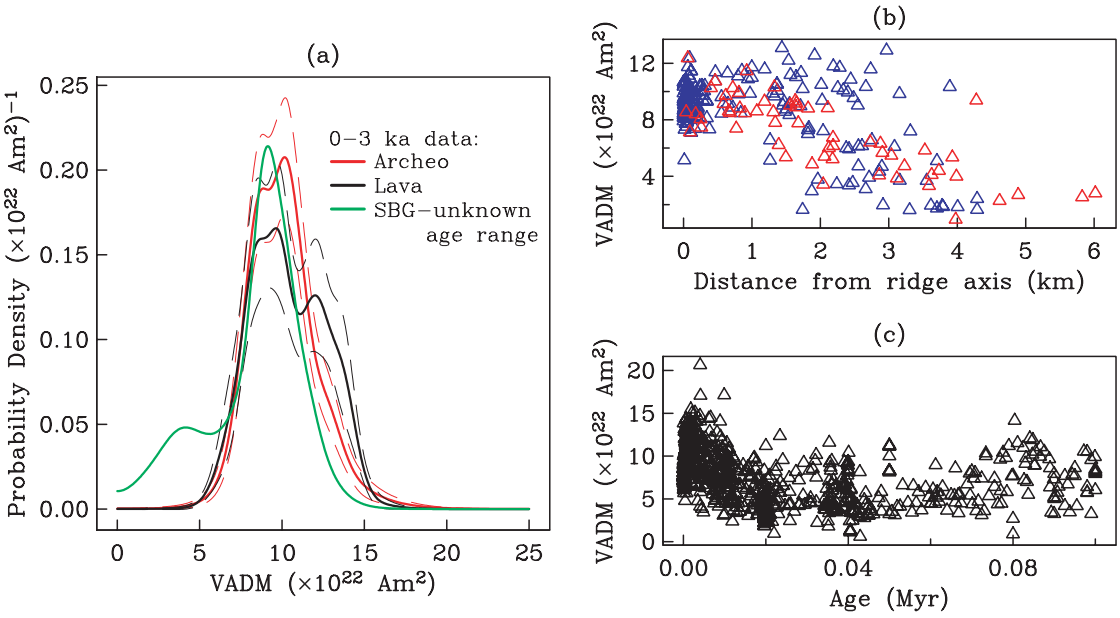

Figure 2.7: Pdfs of archeointensities (red) and paleointensities from lava flows (black) as in Fig. 2.6 with ages spanning 0-3 ka, along with the pdf of SBG data (green) with ages spanning 0-100 ka as calculated by distance from the ridge axis,. Note that the pdf of SBG data is simply the pdf of our compilation of SBG data, not a mean pdf of resampled data sets. (b) SBG paleointensity data (converted to VADMs) from (Bowles et al., 2006) and (Gee et al., 2000) in blue and red respectively plotted vs. distance from the ridge axis. (c) 0-100 ka paleointensity data from subaerial lava flows (converted to VADMs) plotted vs. age.

stretched and truncated version of the paleointensity vs. age plot. This comparison further illustrates that ages of samples close to the ridge axis do not correlate well with crustal age.

The age uncertainties limit our ability to make conclusive detailed comparisons between SBG data and data from archeological objects or other igneous sources. It does seem clear that SBG samples give paleointensities comparable to those of other materials. We see no evidence that SBG paleointensities are biased low, as argued by some (Heller et al., 2002; Valet, 2003). If anything, the SBG data are high, though it seems clear that the high values are reasonable given the age uncertainty of the data.

2.5 Discussion and Conclusions

2.5.1 Archeo- and Paleointensity

Paleointensities determined from igneous sources are higher on average and have more scatter than archeointensities of the same age range (0-7 ka). The difference in means is a little over 10%. We considered two possible explanations for this. The first is that a systematic bias might arise from the laboratory methods used to determine paleointensity. From the Geomagia database it is straightforward to determine the general technique used (it is recorded for 88% of igneous and 83% of archeomagnetic results), and following an anonymous reviewer's comment that "it is well known that the microwave method yields lower determinations compared with the Thellier method" we assessed the relative distribution among Shaw, Thellier, and microwave methods in the two data groups. Only 1.5% of the archeomagnetic data were acquired using the microwave technique, compared with 14% of the igneous data. Thus the use of the microwave method can only be the source of bias if microwave paleointensities in this data set are systematically higher rather then lower than those from Thellier, Shaw and undocumented methods. We note that in general it is difficult to make systematic assessments of the influence of particular experimental methods because it is only in rare cases that direct comparisons have been made on identical samples.

A second explanation for the difference could be that lava flows and archeological objects have different natural cooling rates. It has been shown (Halgedahl et al., 1980; Dodson and McClelland-Brown, 1980; Fox and Aitken, 1980; Leonhardt et al., 2006) that when materials cool in nature at much slower rates than they do when cooling in laboratory paleomagnetic experiments, the paleointensities derived from the lab work can be biased high. If archeological objects cool more quickly in nature than lava flows, they would be less biased high than the lava data. While both materials likely have variable cooling rates from site to site, and so an exact correction cannot be applied to a global data set, we can test to

see if the higher mean VADM for lavas (relative to archeointensity data) can be accounted for by a reasonably realistic cooling rate bias. If we assume that all paleointensities from igneous sources are 15% high (this easily falls in the observed range of cooling rate error) and adjust these data, the pdf and mean of the lava data look much more similar to those of the archeointensity data set (Figure 2.6(c) and (d), Table 2.1). Of course, the archeointensity data could also be in need of a cooling rate correction (Fox and Aitken, 1980). However, as archeological objects generally cool more quickly and have higher blocking temperatures than lava specimens, they would incur less of a cooling rate error and need smaller corrections. Donadini et al. (2007) assessed the correlation among intensities derived from lavas and archeological objects, and found that the correlation was good (inferring from this that intensities derived from lavas are reliable), but the relationship between the two data sources was not 1:1, especially if considering only lava specimens which were analyzed using Thellier-Thellier method techniques. We do not test specifically for correlation, but also conclude that there is some discrepancy between the two data sets - enough to warrant more investigation and/or a correction factor but not enough to deem one source unusable.

2.5.2 Significance of Sidelobe in PDF

In the original data set, we see an unusual sidelobe in the pdf of the VADM data set around $5\times10^{22}Am^2$. This feature did not disappear under any circumstances tested in this study.

The sidelobe could be due to typically low paleointensity transitional data (data which have virtual geomagnetic poles lower than a certain cutoff latitude - usually 45^o, labeled 'T' in Pint03). We tested this by looking at a subset of 0-1 Ma data which specifically excluded transitional data. The sidelobe is still present.

Previous studies have noted bimodal distributions of virtual dipole moments (VDMs) for various time ranges and hypothesized that this might indicate two distinct states of geodynamo behavior (Heller et al., 2002, 2003). The struc-

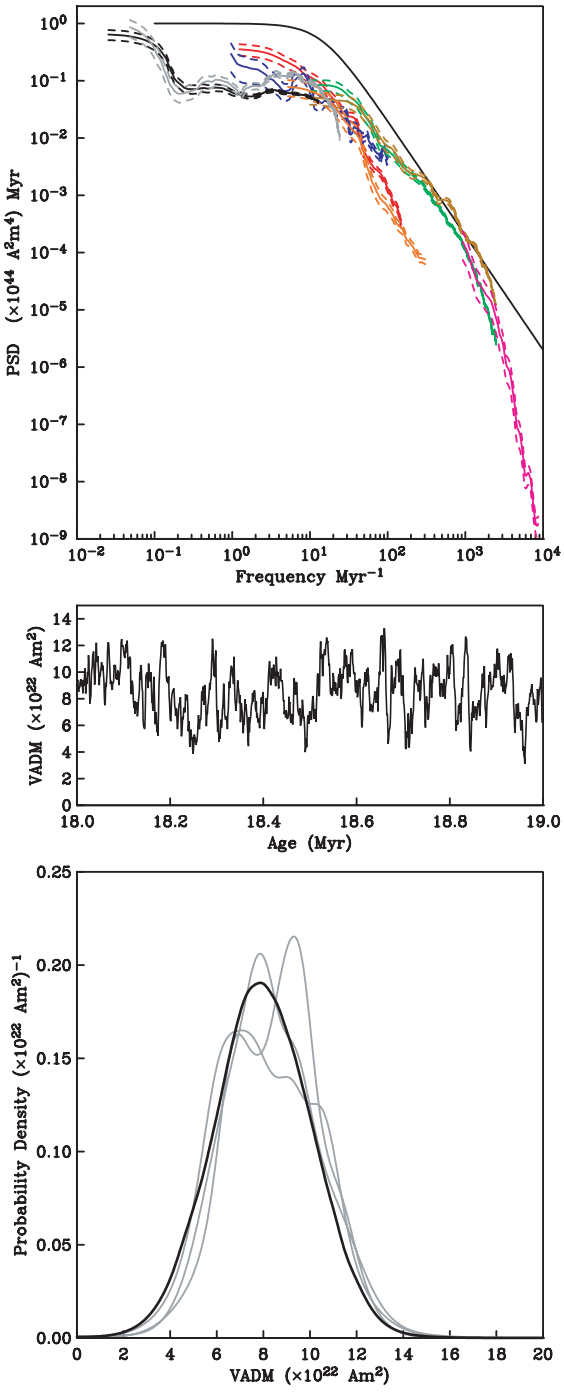

Figure 2.8: (top) Empirical paleomagnetic power spectrum, reproduced from Constable and Johnson (2005) and model (heavy black). (middle) One million years of simulated paleointensity (see text). (bottom) Pdfs of entire 0-100 Myr simulated paleointensities (heavy black) and three pdfs of paleointensities from 1 Myr intervals (gray).

ture in probability density we see in Figure 2.5(a) appears somewhat more subtle than two distinct distributions. Additionally, we see no obvious two-state signal in the pattern of VADM vs. time (see Figure 2.1b).

It is possible that the data set is not yet large enough to resolve a smooth pdf. However, it is also possible that the structure reflects some distinct property of geomagnetic field behavior, that could be resolved if we had a better understanding of how the magnetic field varies over time. To interpret the significance of the structure we see, we first investigate if a 1 Myr time series with the given temporal resolution (around 1000 data points per 1 Myr) is adequate to determine the underlying distribution associated with long term paleofield behavior. For this purpose, we simulate time series which share the same spectral properties as paleomagnetic field intensity variations and then compare their statistical properties with those of our real data set. We model the spectral content using the paleomagnetic power spectrum for the dipole moment estimated by Constable and Johnson (2005) and shown in Figure 2.8. For our tests we choose a simple functional form to approximate the empirical spectrum with a plateau at low frequency and a power law decay at high frequency. That is we suppose the spectrum $S(f)$ has the following functional form:

$$S(f) = \frac{a}{b + cf^p} \tag{2.5}$$

and present specific results from the model function:

$$S(f) = \frac{1}{1 + 0.005f^2} \tag{2.6}$$

The empirical paleomagnetic power spectrum and our model power spectrum are plotted together in Figure 2.8. The simplistic model generally follows the trends of the empirical power spectrum. We make no attempt to derive a best fit model here, as it is not necessary for this exploratory exercise.

We simulate a 100 Myr time series of paleointensity data with the spectrum $S(f)$, and study the distributions of the 100 Myr record as well as 1 Myr

subsets. The simulation has 1000 points per million years, to be comparable in data density to the 0-1 Ma absolute paleointensity data set. Figure 2.8 shows an example of 1 Myr of simulated data and probability density distributions associated with the entire 100 Myr of simulated data as well as a few examples of 1 Myr distributions. Although the 100 Myr distribution is smooth and approximately normally distributed, we see a range of structures in the 1 Myr pdfs and variable levels of similarity to the 100 Myr pdf. One pdf agrees very well with the 100 My pdf, one has a sidelobe similar to the one we see in the real 0-1 Ma paleointensity distribution, and one has even more structure. This result indicates that we should not expect a time series with spectral properties of the paleofield intensity to be adequately represented by a 1 Myr time sample. Although the one million year samples have relatively similar means to each other and to longer time samples, 1 Myr is not long enough to recover the shape of the underlying distribution associated with field intensity. This simple experiment shows that we do not need to call upon two states of the geodyamo or other physical explanations to explain the structure we see in the 0-1 Ma absolute paleointensity data set.

Our interpretation of the sidelobe in the pdf for VADMs as a reflection of actual geomagnetic field behavior in the 0–1 Ma interval can be strengthened by supporting data from sedimentary relative paleointensity records. Figure 2.9 shows the corresponding pdf derived from the most recent half of the SINT2000 dipole strength estimate (Valet et al., 2005), after re-normalization to the equivalent mean value. The sedimentary record (in gray) does indeed have a similar structure to the absolute intensity curve (black), but its variability is subdued in comparison. This is expected from the heavy smoothing that arises in temporal alignment and averaging of data from diverse sedimentary records. Such smoothing is well demonstrated by the power spectrum for SINT800 (Guyodo and Valet, 1999) which appears as the orange curve in Figure 2.8. The power at frequencies higher than about 10–20 Myr^{-1} is attenuated substantially in SINT800 compared with other spectra derived from individual cores (brown, green, and blue curves),

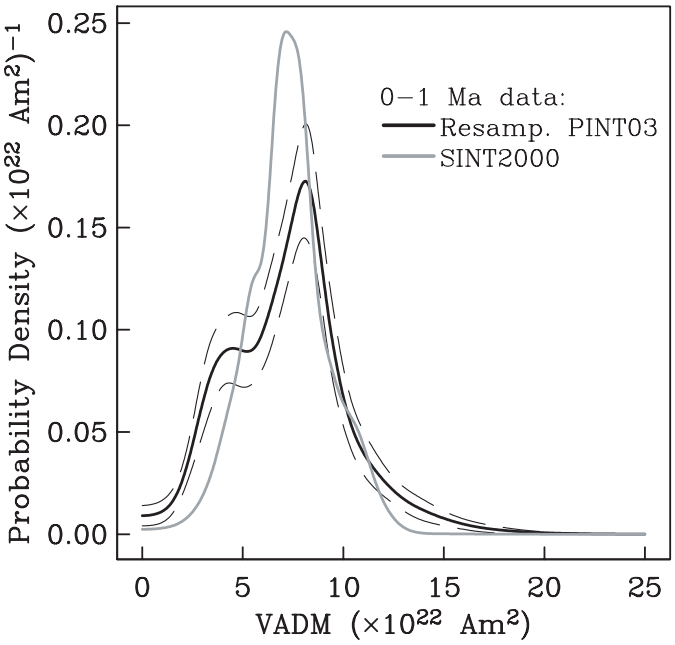

Figure 2.9: Mean pdf of 0-1 Ma Pint03 resampled data sets (black) with 95% confidence bounds (black dash) identical to the red pdf in Fig. 2.5 (a) and pdf of data points from the 0-1 Ma time interval of the SINT2000 relative paleointensity stack (see text).

and corresponds to a reduced variance in the time domain. Individual relative paleointensity records derived from sediments might in principle provide a higher resolution pdf, but in our experience so far many of these are difficult to interpret directly because of the influences of varying sedimentation and other complicating factors.

2.5.3 Suitability and Limitations for Field Modeling

The absolute paleointensity data set compiled in Pint03, including data from all laboratory techniques, reported error, and geographic locations can be used to evaluate average field behavior over the 0-1 Ma time range. The small variability in bootstrapped estimates of mean and variance indicate that the amount and quality of data provide robust estimates of these statistics. Our studies show that the mean VADM for the last million years is $7.26 \pm 0.14 \times 10^{22} Am^2$. This result incorporates temporal resampling to correct for the uneven age distribution of the

data. Further, the result changes only insignificantly when restricting the data used in the estimate to be of a certain reported uncertainty, to be obtained using Thellier-Thellier methods with pTRM checks, or to exclude data from Hawaii. This is reassuring, especially in the context of time varying field modeling, since it means that using lower quality data (and hence using a much larger data set) does not seem to greatly affect the resulting field.

Careful consideration will be needed when combining intensity estimates found from differing material types. Recent data from SBG, as compared to data from subaerial lava flows and archeological objects, seem to give comparable intensities. Detailed comparisons are difficult because of age uncertainties in very young SBG data. For young SBG data, the uncertainties in ages are too great to make the data useful for time varying field modeling, but for older samples the age uncertainties for SBG will be comparable to those in other materials. Nothing in this study indicated that young SBG data are biased to low values of VADM.

Further investigation into causes of observed differences in archeointensities and paleointensities derived from lavas will be necessary to find the most appropriate way to combine these data types in modeling. Differences in cooling histories between the two data sources could explain differences in mean intensities seen in our results, though we have not ruled out other reasons for the discrepancy between these two data types. The cooling rate explanation is significant because it would imply that lava data are biased to high values. A more detailed study of the differences would be be useful in confirming our observations and finding more conclusive explanations.

One of the greatest limitations of the 0-1 Ma paleointensity data set is the poor spatial coverage, which restricts the capacity for any quantitative analysis in search of non-dipole signals and/or assessing their influence on field inferences based on the geocentric axial diople (GAD) assumption. Testing the GAD assumption would require (ideally) that data at each latitude (or in each latitude bin) cover the same time span, and that that time span is long enough and the data

plentiful enough to be able to have a robust time-averaged field estimate at that latitude. In the small latitude range where these conditions are met (Figure 2.2), the latitude bin averages are similar enough that adhering to the GAD assumption and converting data to VADM is not unreasonable. However, more investigation is needed and we can expect greater clarity on this issue as more data become available. An ongoing systematic analysis combining the absolute paleointensity data with relative paleointensity records from sediments should also help in this area.

2.6 Acknowledgments

This work was supported under NSF grant EAR-0337712. We thank Lisa Tauxe, Kristin Lawrence, and Fabio Donadini for useful discussions. The text was improved by taking into account the comments of two anonymous reviewers.

Chapter 2, in full, is a reprint of the material as it appears in L. B. Ziegler, C.G. Constable and C. L. Johnson (2008), Testing the robustness and limitations of 0-1 Ma absolute paleointensity data, Physics of Earth and Planetary Interiors. The dissertation author was the primary investigator and author of this paper. The dissertation author was the primary investigator and author of this paper.

References

Abramson, I. S., 1982: On bandwidth variation in kernel estimates - a square root law. *Annals of Statistics*, **10**(4), 1217–1223.

Barbetti, M., 1977: Measurements of recent geomagnetic secular variation in south-eastern australia and the question of dipole wobble. *Earth Planet. Sci. Lett.*, **36**, 207–218.

Bowles, J., Gee, J. S., Kent, D. V., Bergmanis, E., and Sinton, J., 2005: Cooling rate effects on paleointensity estimates in submarine basaltic glass and implications for dating young flows. *Geochem. Geophys. Geosyst.*, **6**, Q07002, doi:10.1029/2004GC000900.

Bowles, J., Gee, J. S., Kent, D. V., Perfit, M. R., Soule, S. A., and Fornari, D. J., 2006: Paleointensity applications to timing and extent of eruptive activity, 9 degrees-10 degrees n east pacific rise. *Geochem. Geophys. Geosyst.*, **7**, Q06006, doi:10.1029/2005GC001141.

Carlut, J., Cormier, M. H., Kent, D. V., Donnelly, K. E., and Langmuir, C. H., 2004: Timing of volcanism along the northern east pacific rise based on paleointensity experiments on basaltic glasses. *J. Geophys. Res.*, **108**, B04104, 10.1029/2003JB002672.

Carlut, J. C., and Kent, D. V., 2000: Paleointensity record in zero-age submarine basaltic glasses: testing a new dating technique for recent morbs. *Earth Planet. Sci. Lett.*, **183**, 389–401.

Constable, C. G., and Johnson, C. L., 1999: Anisotropic paleosecular variation models: Implications for geomagnetic observables. *Phys. Earth Planet. Int.*, **115**, 35–51.

Constable, C. G., and Johnson, C. L., 2005: A paleomagnetic power spectrum. *Phys. Earth Planet. Int.*, **153**, 61–73.

Dodson, M. H., and McClelland-Brown, E., 1980: Magnetic blocking temperatures of single-domain grains during slow cooling. *J. Geophys. Res.*, **85**(B5), 2625–2637.

Donadini, F., Korhonen, K., P., R., and Pesonen, L. J., 2006: Database for holocene geomagnetic intensity information. *EOS Transactions, American Geophysical Union*, **87**(14), 137, 143.

Donadini, F., P., R., Korhonen, K., Kahma, K., Pesonen, L. J., and Snowball, I., 2007: Holocene geomagnetic paleointensities: A blind test of absolute paleointensity techniques and materials. *Phys. Earth Planet. Int.*, **161**, 19–35.

Efron, B., and Tibshirani, R. J., 1993: *An introduction to the bootstrap*. Chapman&Hall.

Fox, J. M. W., and Aitken, M. J., 1980: Cooling-rate dependence of thermoremanent magnetisation. *Nature*, **283**, 462–463.

Gee, J. S., Cande, S. C., Hildebrand, J. A., Donnelly, K., and Parker, R. L., 2000: Geomagnetic intensity variations over the past 780 kyr obtained from near-seafloor magnetic anomalies. *Nature*, **408**, 827–832.

Guyodo, Y., and Valet, J. P., 1996: Relative variations in geomagnetic intensity from sedimentary records: The past 200,000 years. *Earth Planet. Sci. Lett.*, **143**(1-4), 23–36.

Guyodo, Y., and Valet, J. P., 1999: Global changes in geomagnetic intesnity during the past 800 thousand years. *Nature*, **399**, 249–252.

Halgedahl, S. L., Day, R., and Fuller, M., 1980: The effect of cooling rate on the intensity of weak-field trm in single domain magnetite. *J. Geophys. Res.*, **85**(B7), 3690–3698.

Heller, R., Merrill, R. T., and McFadden, P. L., 2002: The variation of earth's magnetic field with time. *Phys. Earth Planet. Int.*, **131**, 237–249.

Heller, R., Merrill, R. T., and McFadden, P. L., 2003: The two states of paleomagnetic field intensities for the past 320 million years. *Phys. Earth Planet. Int.*, **135**(2-3), 211–223.

Jackson, A., Jonkers, A., and Walker, M., 2000: Four centuries of geomagnetic secular variation from historical records. *Phil. Trans. Roy. Soc. Lond.*, **358**(1768), 957–990.

Korte, M., and Constable, C. G., 2005a: Continuous geomagnetic field models for the past 7 millenia ii: Cals7k. *Geochem. Geophys. Geosyst.*, **6(2)**, Q02H16, doi:10.1029/2004GC000801.

Korte, M., and Constable, C. G., 2005b: The geomagnetic dipole moment over the last 7000 years - new results from a global model. *Earth Planet. Sci. Lett.*, **236**, 348–358.

Leonhardt, R., Matzka, J., Nichols, A. R. L., and Dingwell, D. B., 2006: Cooling rate correction of paleointensity determination for volcanic glasses by relaxation geospeedometry. *Earth Planet. Sci. Lett.*, **243**(1-2), 282.

McElhinny, M. W., and Senanayake, W. E., 1982: Variations in the geomagnetic dipole 1: the past 50,000 years. *J. Geomag. Geoelectr.*, **34**, 39–51.

McFadden, P. L., and McElhinny, M. W., 1982: Variations in the geomagnetic dipole 2: statistical analysis of vdms for the past 5million years. *J. Geomag. Geoelectr.*, **34**, 163–189.

Mejia, V., Opdyke, N. D., and Perfit, M. R., 1996: Paleomagnetic field intensity recorded in submarine basaltic glass from the east pacific rise, the last 69 ka. *Geophysical Research Letters*, **23**(5), 475–478.

Perrin, M., and Schnepp, E., 2004: Iaga paleointensity database: distribution and quality of the data set. *Physics Earth Planet. Int.*, **147**, 255–267.

Pick, T., and Tauxe, L., 1993: Holocene paleointensities: Thellier experiments on submarine basaltic glass from the east pacific rise. *J. Geophys. Res.*, **98**, 17949–17964.

Press, W. H., Teukolsky, S. A., Vetterling, W. T., and Flannery, B. P., 1986: *Numerical Recipes in Fortran 77: the Art of Scientific Computing*. Cambridge University Press.

Selkin, P., and Tauxe, L., 2000: Long term variations in palaeointensity. *Phil. Trans. Roy. Soc. Lond.*, **A358**, 1065–1088.

Silverman, B. W., 1986: *Density estimation for statistics and data analysis*. Monographs on statistics and applied probability. Chapman and Hall.

Tauxe, L., and Kent, D. V., 2004: A simplified statistical model for the geomagnetic field and the detection of shallow bias in paleomagnetic inclinations: Was the ancient magnetic field dipolar? In *Timescales of the Paleomagnetic field*, editors J. Channell, D. Kent, W. Lowrie, and J. G. Meert, volume 145 of *Geophysical Monograph*, 101–116.

Tauxe, L., and Yamazaki, T., 2007: Paleointensities. In *Geomagnetism*, editor M. Kono and G. Schubert, volume 5 of *Treatise on Geophysics*, 509–563. Elsevier, Amsterdam.

Valet, J., 2003: Time variations in geomagnetic intensity. *Reviews of Geophysics*, **41**(1). doi:10.1029/2001RG000104.

Valet, J. P., Meynadier, L., and Guyodo, Y., 2005: Geomagnetic dipole strength and reversal rate over the past two million years. *Nature*, **435**(7043), 802–805. doi:10.1038/nature03674.

Chapter 3

PADM2M: A Penalized Maximum Likelihood Model of the 0-2 Ma Paleomagnetic Axial Dipole Moment

Abstract

We present a new time-varying model for Paleomagnetic Axial Dipole Moment (PADM) for the past 2 million years and compare it with earlier Virtual Axial Dipole Moment (VADM) reconstructions which have been based on stacking and averaging scaled relative paleointensity records. The PADM is derived from both absolute and relative paleointensity data and constructed using a new penalized maximum likelihood (PML) approach to recover a cubic B-spline representation of axial-dipole field variations on million year timescales. The PML method is explicitly intended to reduce bias in estimating the true axial dipole moment that arises in average VADM reconstructions. We apply the PML method to a set of 96,032 published data (1,800 paleointensities from igneous rocks, 3,300 archeointensities, and 86 relative paleointensity time series of variable lengths and resolutions). Two models are discussed: PADM2Mp is a trial model based on a

subset of the 9 longest available sedimentary records; PADM2M uses a comprehensive data set (76 records, 81,446 data; 10 records were eliminated) and is our preferred model. PADM2M has a lower mean than existing VADM reconstructions but shows similarities in long-period variability. Some differences in timing, amplitude, and resolution of certain features can be attributed to variations in age assignments. Others result from our more comprehensive data set and a reduction in bias attributable to PML modeling. PADM2M has an average axial dipole moment over 0-2 Ma of $5.3 \times 10^{22} Am^2$ with a standard deviation of $1.5 \times 10^{22} Am^2$. The Brunhes chron average ($6.2 \times 10^{22} Am^2$) is higher than for earlier epochs of Matuyama ($4.8 \times 10^{22} Am^2$), as seen in some previous studies. The power spectrum for our model agrees with previous estimates of the global paleomagnetic power spectrum for frequencies up to about $10^2 Myr^{-1}$. We see no distinctive evidence in the power spectrum for orbital forcing of geodynamo behavior.

3.1 Introduction

Earth's history can be investigated through the paleomagnetic record. Dynamic processes in the core drive the continuously changing geomagnetic field, which is recorded on Earth's surface by newly forming igneous rocks and sediments. On centennial and millennial time scales, time-varying spherical harmonic models of Earth's magnetic field derived from historical, archeomagnetic, and/or paleomagnetic data (Jackson et al. (2000); Korte and Constable (2005); Korte et al. (2009)) have yielded insights into dynamo processes (e.g. Amit and Olson (2006); Dumberry and Finlay (2007); Wardinski and Korte (2008)).

On million year timescales, time-varying reconstructions of paleomagnetic field behavior are limited by the quantity and quality of available data. As a starting point, the field is often approximated by a dipole, or more specifically a field resulting from a geocentric axial dipole (GAD) source. The GAD approximation is sometimes made under the assumption that it provides an accurate representation

of the time-averaged field structure. Numerous studies have shows that this is not exactly the case (Wilson (1970); Johnson and McFadden (2007); Johnson et al. (2008)), but it remains a useful starting point for understanding field changes on long time scales. The axial-dipole alone represents the largest geographic and temporal variations in the geomagnetic field, and (depending on the available data) may be the only structure recoverable through the data uncertainties. The spatial structure has large geographic variability but is static, so time variations under the GAD model are restricted to changes in the strength of the Paleomagnetic Axial-Dipole Moment (PADM), the terminology we will use for strength of the axial dipole. When paleointensity data are considered under the GAD model they are usually converted into Virtual Axial Dipole Moment (VADM) data – the VADM is the equivalent moment associated with a dipole source aligned with Earth's rotation axis that is needed to produce the paleointensity datum at the latitude of the specific observation. This transformation removes the geographic variations in paleointensity that would be expected for an axial-dipole source. The goal of this work is to use VADM data to find optimal estimates for the PADM.

Under the GAD approximation, a number of time-varying paleomagnetic field strength reconstructions have been made both from globally distributed data (Valet et al., 2005; Channell et al., 2009) and regional data sets (Stoner et al. (2002); Laj et al. (2000)). These efforts involve stacking and averaging relative paleointensity time series derived from sediments and sometimes calibrating the resulting stack to absolute VADM variations through comparison with absolute paleointensity derived from igneous rocks.

These VADM models are somewhat limited in temporal resolution, and are clearly limited by the fixed geographic structure, but nevertheless provide useful information for testing the feasibility of particular dynamo regimes. Investigations to date have included characterizing the timescales associated with field reversals and excursions (Valet et al., 2005), observations of possible asymmetry in the field decay and growth processes associated with reversals (commonly referred to

as 'sawtooth' paleointensity signals), e.g. Valet and Meynadier (1993); McFadden and Merrill (1997); Valet et al. (2005), deriving the power spectrum associated with field intensities including corner frequencies and falloff (Constable and Johnson, 2005; Driscoll and Olson, 2009), among other things. VADM models are also used as magnetostratigraphic tools (e.g. Stoner et al. (1998); Brachfeld et al. (2003)) with global intensity variations providing much higher resolution than the geomagnetic reversal record, but these applications are not the focus of this study.

In this paper we first describe the available VADM data (Section 3.2), then motivate, develop, and apply a new approach for recovering paleomagnetic axial dipole moment variation on million year timescales (Section 3.3). We show that a simple average of VADM data leads to a biased estimate of the PADM (Appendix 3.8), illustrating that the noise distribution associated with VADM data is non-gaussian and asymmetric. We introduce a simple but flexible parametric model for the noise that can take account of variability among the various data records. We develop a penalized maximum likelihood (PML) inversion procedure to recover estimates of PADM that are less biased and apply it to construct a regularized, cubic B-spline model of time-varying PADM over the last two million years (Section 3.3, Appendix 3.9). The resulting PADM2M model is made from a combination of globally distributed absolute paleointensity (API) data and relative paleointensity (RPI) records from sediment cores. As part of the modeling procedure we solve for scaling factors needed to calibrate the relative paleointensity records to virtual axial dipole moments. Our results are presented in Section 3.4, where we describe a preliminary model PADM2Mp constructed from 9 records, each spanning more than 1.5 Myr and including the Brunhes/Matuyama polarity reversal, and our preferred model PADM2M derived from a much larger and more heterogeneous set of currently available RPI time series.

3.2 VADM Data for Global Modeling

For the construction of time-varying paleomagnetic field models, we would ideally use many tightly dated, globally distributed records of intensity variation. In practice, the data available consist of spot recordings (from igneous rocks and archeological artifacts) of absolute field intensity values, and time series (from sediments) of relative field intensity variations. The spot recordings are dated using a range of techniques with correspondingly diverse uncertainties. Although this statement is true of sedimentary data as well, the sequential nature of magnetic measurements taken at regular spacings through a core mean that at least the temporal order is certain. The time series generated from long cores provide information on field strength variations for up to millions of years but cannot constrain the absolute field strength, while the spot recordings adequately constrain field strength but on their own are too sparse to give a picture of field variations on million year time-scales. Our modeling uses both absolute paleointensities (API) and relative paleointensity (RPI) time series to develop a composite picture of field intensity variations over the last two million years.

All data used in this study are drawn from previously published work. We take advantage of freely available, public domain databases in our efforts to build comprehensive data sets suitable for analysis (described below). The exact data compilation used in this study is archived in the EarthRef Digital Archive (http://earthref.org/erda/1138) along with the PADM2M model (http://earthref.org/erda/1139).

3.2.1 Absolute Paleointensity Data

API data are derived from iron-bearing igneous rocks and archeological artifacts which were once hot enough to become magnetized in response to the Earth's magnetic field present at their formation. As these materials cool through the blocking temperature spectrum of the relevant magnetic minerals, the rema-

nent magnetism is frozen in. The theory of thermal remanence acquisition is well understood for simple systems involving single domain magnetite and forms the basis for the pioneering Thellier and Thellier (1959) laboratory technique to recover the ancient magnetic field strength which produced the magnetization of a given sample. There are now many variants on the original method and new methods, that are intended to reduce measurement error, sample alteration, and incorporate internal consistency checks on assumptions inherent to the method. Additionally, various strategies are sometimes employed for making cooling rate or anisotropy corrections (see Tauxe and Yamazaki (2007) for a more comprehensive discussion of modern paleointensity laboratory techniques). Lack of uniformity in laboratory procedures and natural variations in source materials lead to a broad range of contributions to uncertainties in the resulting paleointensity data.

We are interested in using as many data as possible, and do not restrict our dataset to any particular minimum uncertainty level, quality criteria, laboratory procedure, or source material. In a detailed analysis of a diverse paleointensity data set, Ziegler et al. (2008) found that field strength statistics derived from the set of all available records and subsets which excluded less reliable data (based on a few specific criteria) were not significantly different. They concluded that although the use of less reliable data is not the preferred strategy, it does not significantly bias results. This further supports the strategy of using all available paleointensity data in our models. Ziegler et al. (2008) did note a statistical difference between data derived from archeological and igneous sources. Here, we use both material types, but treat them as two distinct data sets.

The most recent Geomagia50.v2 database (Donadini et al., 2009) compiles API data from archeological and igneous sources with ages less than 50 kyr. We use all data in this database except for some submarine basaltic glass data which have poorer age constraints than the rest of the database. In total, we take 4236 data from Geomagia50.v2 as of June 2009 (902 from igneous sources, 3334 from archeological or unspecified materials). For data older than 50 kyr, we look to

the PINT paleointensity database, PINT08 (Biggin et al., 2009). This database contains thousands of data covering all ages older than 50 kyr, but we only use the 868 data with ages greater than 50kyr and less than 2 Myr. We have incorporated improved ages (Singer et al., 2008) for 16 data. Finally, we have added 30 data from Lawrence et al. (2009), giving us a total of 898 data with nominal ages of 50kyr-2Myr.

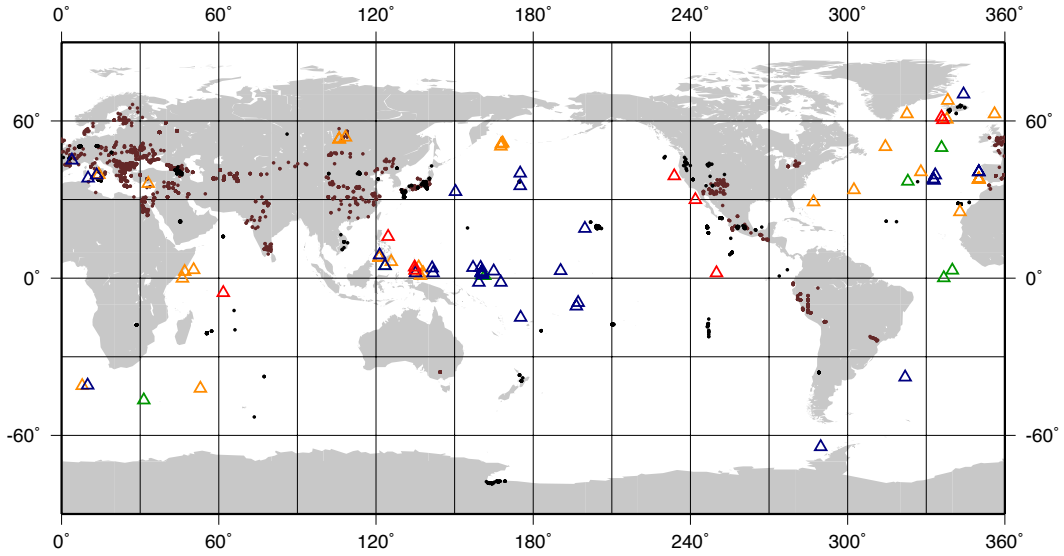

Figure 3.1: Geographic distribution of data used in this study. Small circles are for API data (brown for archeomagnetic data, black for igneous data). Triangles represent sediment cores, where red, blue, yellow, and green correspond to P0, Long, Young, and Reversal records respectively (see text).

The geographic and temporal distributions of the API data are given in figures 3.1 and 3.2 , respectively. Data are mainly concentrated at northern mid-latitudes, although there are some available in the southern hemisphere. Archeomagnetic data are generally less than 10 kyr in age, and are particularly dense in Europe. Hawaii is also noteworthy as a source of volcanic paleointensity records. The age distribution of API data is very non-uniform, with a disproportionate number of archeomagnetic contributions and young volcanics (0-10 ka). Age un-

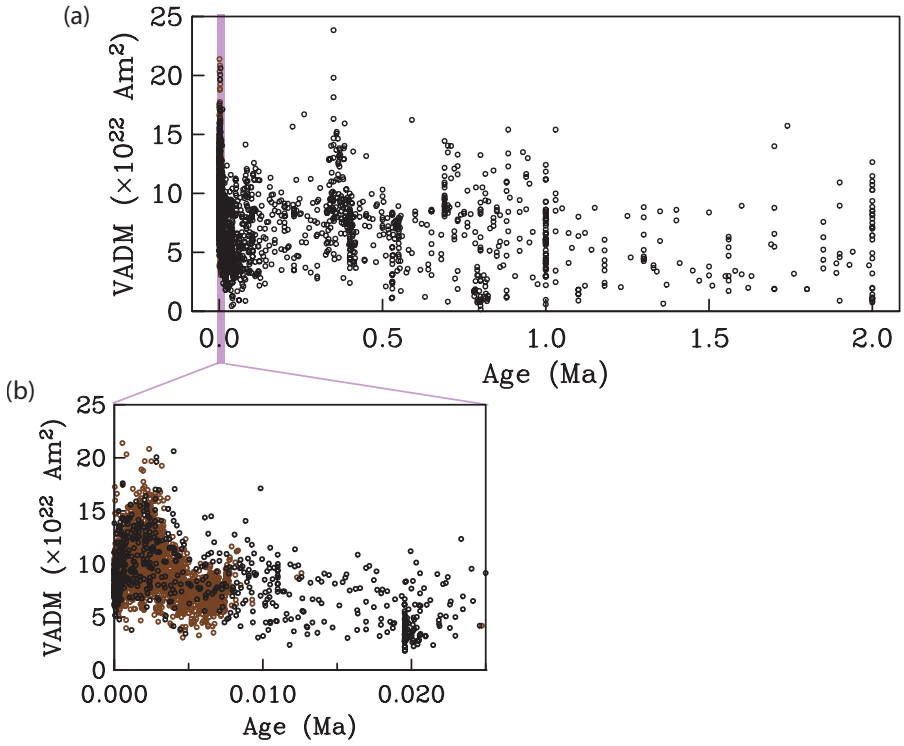

Figure 3.2: API data as a function of age. Black (brown) circles correspond to igneous (archeological) sources. (a) 0-2 Myr (b) 0-25 kyr.

certainties are also highly variable and often poorly documented. However if we take the age information at face value, there are data distributed throughout the past 2 Myr (see Fig. 3.2).

3.2.2 Relative Paleointensity Data

Marine sediments also carry remanent magnetism. However, as opposed to the thermal remanence acquisition process involved in magnetizing API source materials, sediments acquire a detrital remanent magnetization (DRM): As already magnetized detrital grains settle through the water column, they can freely rotate to align with the ambient geomagnetic field. A sample's magnetization depends primarily on the field strength, the amount and type of magnetic material present, and environmental factors such as the sedimentary matrix; after normalizing for

variations in the amount of magnetic material present in the core, the normalized magnetization is supposed to be linearly related to field strength. For already published data it is generally impractical to account for the influence of changing environmental factors (e.g., nature of the sediment matrix, magnetic grain size) on the core's magnetization. Any such factors present will just be incorporated into our noise model. Beyond this, theory needed to recover absolute paleofield intensities from materials which have a DRM is an area of active research. Additionally, some sedimentary environments and/or high field strength can sometimes lead to departures from the linear relationship between normalized magnetism and field strength. A more thorough discussion of sediment RPIs and DRM can be found in Tauxe and Yamazaki (2007) and Valet (2003). Although limited by the absence of theory to recover absolute field intensity, sediments have the advantage of being continuously deposited: sequential measurements down a sediment core give an ordered time series of relative intensity variations. The individual cores reflect a variety of source material compositions, sedimentation rates (and hence, signal resolution and smoothing), normalization proxies, and laboratory procedures.

Recent efforts by the paleomagnetic community have produced a large, geographically diverse set of RPI time series. Numerous lacustrine records have been used in Holocene geomagnetic models (Korte et al., 2009) but we omit almost all these records from our collection because we already have good coverage from archeomagnetic data with generally better age constraints. We primarily use marine cores which provide longer, but typically lower resolution, time series.

We use all the RPI records from the SEDPI06 collection of sediment cores assembled by Tauxe and Yamazaki (2007) whose timescales are independent of correlations based on RPI information and for which we were able to acquire the data. One significant advantage of using the SEDPI06 compilation is that all data have been adjusted to conform to a common Geomagnetic Polarity Time Scale (GPTS) with reversal ages tied to CK95 (Cande and Kent, 1995). This leads to some minor variations from the age models originally published with the data, but

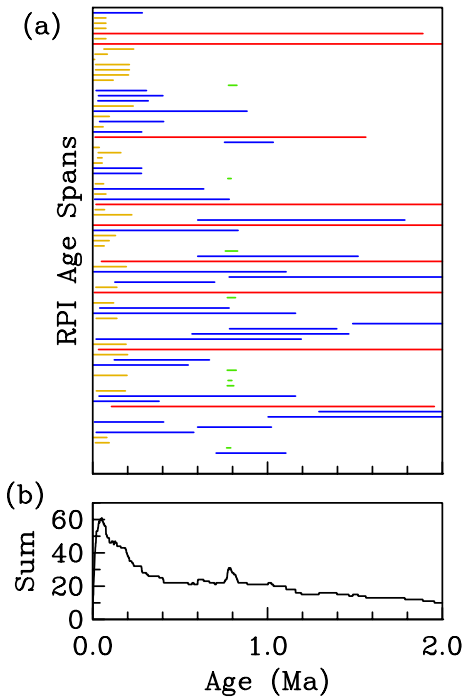

Figure 3.3: Age spans of RPI records, colors as in Fig. 3.1 (red, blue, yellow, and green correspond to P0, Long, Young, and Reversal records respectively). (a) Each bar corresponds to age span of one RPI time series. Names of cores are omitted, but cores are plotted by latitude, with highest latitude records at the top, and decreasing toward the bottom. (b) Total number of RPI time series at each age.

provides us with an internally consistent data set.

Summary information for all 86 cores is given in table 3.1, where for illustrative purposes and to guide our modeling, we have categorized the data into four sets corresponding to the color and letter codes in figures 3.1 and 3.3 . The groups are as follows: 9 (P0) records, 34 Long Records (LR), 35 Young Records (YR) and 8 records focused on the Brunhes/Matuyama Reversal (BM). P0 data all span more than 1.5 of the last 2 Myr and include the Brunhes/Matuyama reversal. LR generally span several 100 kyrs, but may begin at any age. YR are shorter records that do not extend past 250 ka in age. BM records are very short time series developed for studying the Brunhes/Matuyama reversal. In total, the records range from 19 kyr to 2 Myr in length providing variable coverage of the 0-2 Ma interval. Sedimentation rates range from 0.3 to 35 cm/kyr, which provides some idea of the variability in temporal resolution.

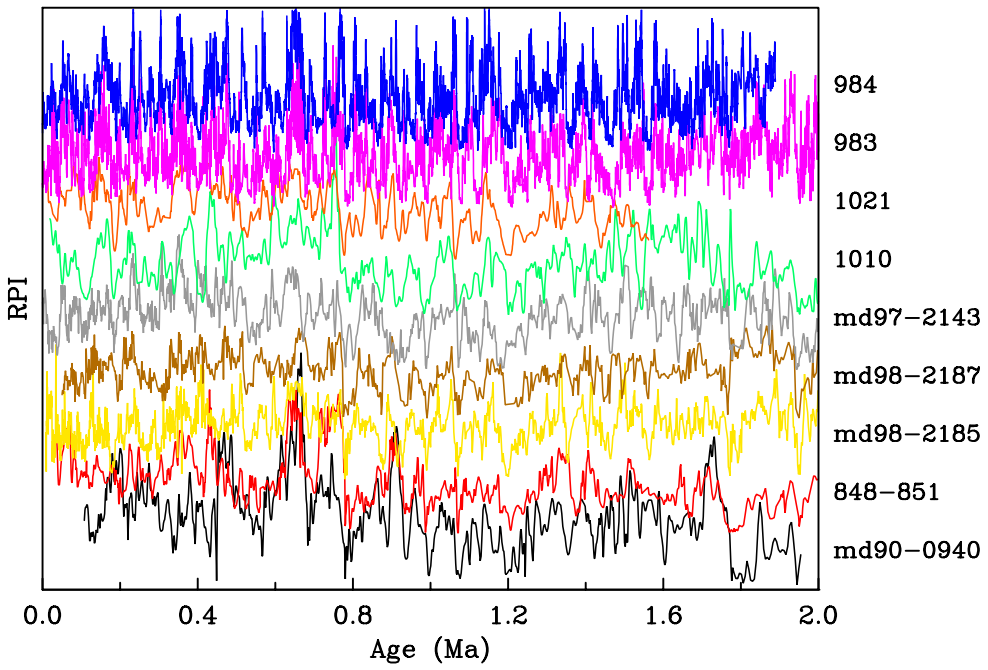

Figure 3.4: P0 RPI records, plotted as RPI vs. Age, where each record has a mean of 1 (offset between records for visual clarity only). Names of cores on right axis.

The geographic distribution of cores is shown by the color-coded triangles

in Fig. 3.1. As with API data, the northern hemisphere data are more numerous, but there is a reasonable number of cores from the southern hemisphere. Fig. 3.3 gives a sense of the actual temporal coverage for the 0-2 Ma interval, plotting the age ranges spanned by each core (with each bar representing one core) along with a plot of the number of cores as a function of age.

The P0 time series form the basis of our preliminary model PADM2Mp and are illustrated in Fig. 3.4, where the differences among the 9 records make it clear that the data reflect more than a simple time-varying axial dipole. The challenge is to extract the PADM, which we first attempt with the P0 data alone and then with the entire set of 86 records. The results are described in Section 3.4, but first we motivate and describe the PML modeling algorithm.

3.3 A Penalized Maximum Likelihood Method

In this section we provide a brief rationale and description of the PML method that is the backbone of our modeling strategy for recovering the PADM. We refer those interested in the details of the algorithm to Appendix 3.9.

From the previous section we abstract the concept of having two distinct kinds of data, and a total of K distinct data series. Each series consists of distinct elements $d_{k,i}$, with subscript k, i refering to the ith point in the kth dataset, where each set is either an RPI time series from a specific location, or a collection of globally distributed API data. Our goal is to recover a time varying description of the PADM, here designated $\nu(t)$ and to outline a specific strategy to accomplish that. There are four aspects to this: (1) choosing a parameterization for $\nu(t)$; (2) using a misfit measure that accommodates the asymmetric noise distribution that is a perennial characteristic of VADM data; (3) recognizing that we want a model whose resulting temporal resolution and complexity is explicitly controlled by the inversion process rather than by the number of model parameters allowed; (4) including an implicit calibration of the RPI data.

The PML strategy that results is basically a merger of a Maximum Likelihood type estimation for parameters in non-Gaussian noise (Constable, 1988) and a quadratic regularized inversion that penalizes roughness to provide a smoothly varying model as a function of time (Constable and Parker, 1988; Parker, 1994) with modifications to suit the specific noise distributions found in the $0-2$ Ma VADM data and to accommodate the joint use of absolute and relative intensity data.

3.3.1 Cubic B-spline Parameterization

Following a strategy widely used for time-varying spherical harmonic models of the geomagnetic field (Bloxham and Jackson, 1992; Jackson et al., 2000; Korte et al., 2009) we write the time-varying PADM, $\nu(t)$, as a linear combination of p cubic B-splines,

$$\nu(t) = \sum_{j=1}^{p} \beta_j c_j(t) \tag{3.1}$$

where $c_j(t)$ are cubic B-spline basis functions evaluated at time t and β_j are the corresponding coefficients. We describe our observations $(d_{k,i})$ at time $t_{k,i}$ as the sum of the model plus a noise term $(\epsilon_{k,i})$, incorporating the scaling of RPI records as follows,

$$\zeta_k d_{k,i} = \nu(t_{k,i}) + \zeta_k \epsilon_{k,i} \tag{3.2}$$

$$= \sum_{j=1}^{p} \beta_j c_j(t_{k,i}) + \zeta_k \epsilon_{k,i} \tag{3.3}$$

where $\zeta_k, \quad k = 1, \ldots, K$ provides the scaling factor needed to calibrate the kth RPI data series into pseudo-absolute VADMs. In the case of API data $\zeta_k = 1$ if the data are expressed as VADMs.

3.3.2 Non-Gaussian noise

When designing or choosing a modeling method, we first need to consider the noise distribution of the data, the statistics of the $\epsilon_{k,i}$. In the case of pale-

ointensity data, the distribution function associated with data noise is unknown - although often implicitly assumed to be gaussian or at least symmetric. The noise associated with VADM data arises from multiple sources including: natural variations inherent to the data materials, uncertainties associated with lab measurements, and contributions associated with local non-axial-dipole field features that are carried along in translating paleointensities into VADMs. None of these noise sources can be assumed gaussian, not least because the scalar paleointensities themselves are bounded below at zero, and the noise may reflect this asymmetry. In Appendix 3.8 we show that the expected distribution is non-gaussian and this introduces bias to estimates of PADM derived by the standard strategies of stacking and averaging multiple RPI records. This bias is in part a consequence of using the scalar intensities only instead of the complete vectors when studying the magnetic field, and is consistent with the conclusion of Love and Constable (2003) who found that an arithmetic mean of intensity data does not correspond to the intensity of the mean field vector.

As an illustration of asymmetry in VADM data that can lead to bias in PADM estimates, consider the 2005 magnetic field as represented by the International Geomagnetic Reference Field (IGRF 2005) (Maus et al. (2005), http://www.ngdc.noaa.gov/IAGA/vmod/igrf.html). We manufactured a dataset of field magnitudes at globally distributed locations, and then convert these into VADMs. If the noise were gaussian, the true axial dipole moment would be best estimated by taking the mean of the data. However, the resulting distribution shown in Fig. 3.5a is non-gaussian and quite asymmetric. In this case, a simple average of the data produces a mean field strength estimate of $8.1 \times 10^{22} Am^2$, while the true axial dipole moment is $7.6 \times 10^{22} Am^2$. A better estimate of the axial dipole moment would be the mode of the distribution ($\sim 7.8 \times 10^{22} Am^2$). While this particular distribution is strongly influenced by the spatial structure of the non-axial-dipole field of IGRF 2005, the skew seen here is a feature also seen in datasets which span long periods of time. For example, a skewed distribution and

corresponding bias in the mean was noted for 0-5 Ma VADMs by McFadden and McElhinny (1982). The distributions associated with the data in Fig. 3.4 are also long-tailed on the positive side (see Fig. 3.5b). Our modeling procedure (described below), estimates the noise distributions of paleointensity data empirically using the residual distributions after model fitting. Residual distributions of the data in Fig. 3.4 for the final PADM2M model are plotted in Fig. 3.5c along with a representative normal distribution. They clearly depart from a normal distribution.

The asymmetry also means that the usual least squares measure of misfit is inappropriate when modeling these data. Alternatively, maximum likelihood (ML) methods will generally give asymptotically unbiased, efficient parameter estimates (Rice, 1995) and can be a better alternative to parameter estimation when noise is known to be non-gaussian (or when one wants to avoid making this assumption). We therefore develop a maximum likelihood approach to our PADM modeling.

3.3.3 Maximum Likelihood Methods

As mentioned above, we parameterize the time-varying PADM with cubic B-splines, and build on ML fitting methods developed by Constable (1988). There, an ML-type method is used to find a best fitting set of model parameters, where these parameters are coefficients $\beta_j, \quad j = 1, \ldots, p$ for a set of basis functions (in our case, cubic B-splines). When the noise distribution is known the solution to the non-linear ML problem is reframed in the form of an iteratively re-weighted least squares problem, which is solved using one of a number of readily available computational tools (see Press et al. (1986)). Constable (1988) proposed that when the probability density function (pdf) for the noise is not known *a priori*, it can be estimated iteratively from the residuals to a best fitting model provided there are sufficient data. In the original formulation, the determination of the pdf was completely empirical and non-parametric (as in Fig. 3.5a, for example), but here we adopt a simple parametric model for the pdf of the noise. We use the best

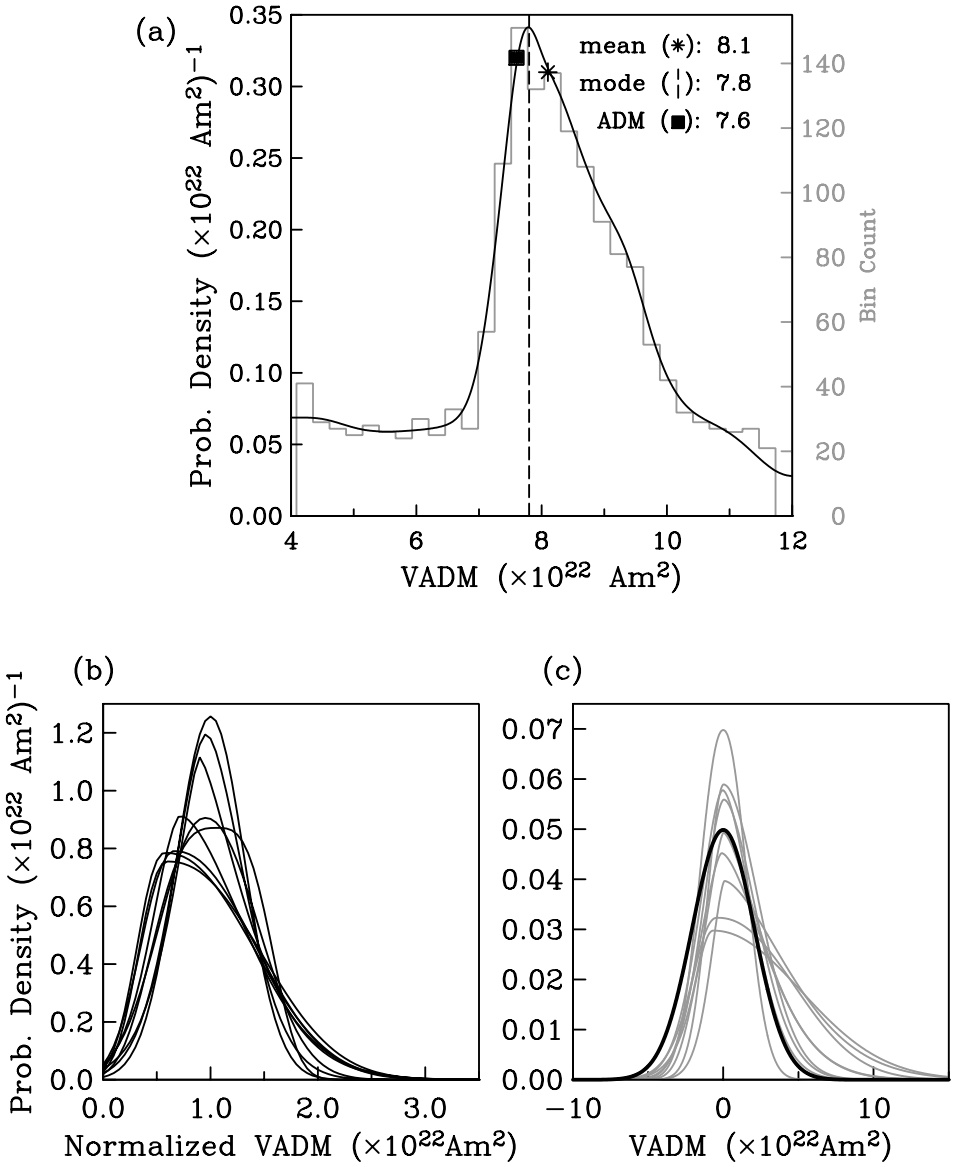

Figure 3.5: (a) Histogram (gray) and pdf (black) of VADMs from the IGRF 2005 field model at a grid of globally distributed locations. Black square corresponds to the true axial dipole moment (from g_1^0), dashed line and asterisk correspond to the mode and mean of the distribution respectively. (b) RPI pdfs for the 9 P0 records, expressed in terms of VADM with a normalized mean of 1. (c) Residual distributions (after PADM2M model fit) for the 9 P0 records (gray) along with a normal distribution (black) with a mean of 0 and a variance intermediate of the residual distributions for reference

fitting Asymmetric Power Distribution pdf (Komunjer, 2007) which has 2 shape parameters, a location and a scaling parameter, to describe the distribution of the residuals. Fig. 3.6 illustrates the broad range of potential APD pdf shapes; a mathematical definition is provided in Appendix 3.9. Both the previous non-parametric estimation and the new APD pdf estimation have the flexibility to take on a variety of shapes in order to fit the unknown noise distribution. However, estimating the pdf of the noise parametrically streamlines the whole fitting routine significantly. The broad range of available APD shapes allows us to accommodate different noise distributions for each of the K time series.

Once the pdf is estimated it is straightforward to recast the ML optimization criteria in the form of an iteratively re-weighted least squares problem and find parameter estimates which maximize the probability of getting the data observed. The method is elaborated in Appendix 3.9, but briefly we note that in order to find a spline model for a single data series of length n_k with noise pdf $f_k(x)$ we would use the following strategy.

The function to be maximized in this case, the likelihood function, $L_k(\hat{\beta})$, is the joint pdf, F_k, of the sample errors, which is in turn the product of the pdfs evaluated at the ML estimate of the parameters β. If the residuals are independent, identically distributed (i.i.d.):

$$L_k(\hat{\beta}) = F_k(\epsilon, \hat{\beta}) = \prod_{i=1}^{n_k} f_k(\epsilon_i, \hat{\beta}) \tag{3.4}$$

As is generally done, in practice we minimize the negative log likelihood ($l_k(\hat{\beta})$), so that the product becomes a sum making the problem more tractable:

$$l_k(\hat{\beta}) = \sum_{i=1}^{n} \rho_k(\epsilon_i), \tag{3.5}$$

where $\rho_k(\epsilon) = -ln[f_k(\epsilon, \hat{\beta})]$ and is termed the loss function.

For the K data sets, minimizing with respect to the model parameters $\hat{\beta}$, and reframing as an iterative weighted least squares problem yields the set of equations:

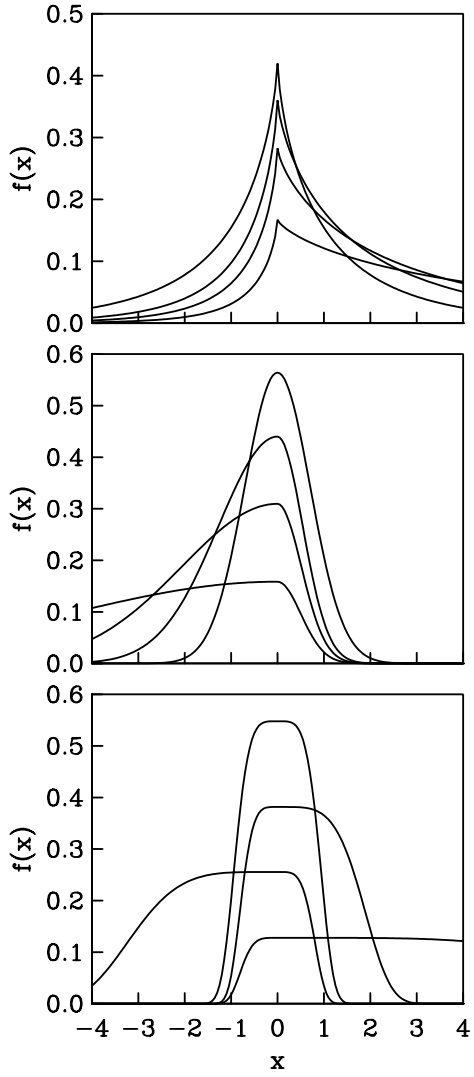

Figure 3.6: Example APD pdfs for an array of shape parameters (see text, Appendix 3.9). $\mu = 0, \sigma = 1$ in all cases. (Top) $\lambda = 0.75, \alpha = 0.1, 0.2, 0.3, 0.5$ (Middle) $\lambda = 2, \alpha = 0.5, 0.7, 0.8, 0.9$ (Bottom) $\lambda = 4.5, \alpha = 0.1, 0.3, 0.5, 0.7$

$$\frac{\partial l}{\partial \beta_j^q} = \sum_{k=1}^{K}\sum_{i=1}^{n_k} w_{k,i}^q c_j(t_{k,i}) \left(\tilde{d_{k,i}} - \sum_{j=1}^{p} \beta_j^q c_j(t_{k,i}) \right) = 0 \tag{3.6}$$

$$w_{k,i}^q = N_k^{q-1} C_k^{q-1} \left| \tilde{d_{k,i}} - \sum_{j=1}^{p} \beta_j^{q-1} c_j(t_{k,i}) \right|^{D_k^{q-1}} \tag{3.7}$$

$$\tilde{d_{k,i}} = \zeta_k d_{k,i} - \mu_k^{q-1} \tag{3.8}$$

The weights used in the qth iteration involve residuals from the previous $(q-1)$th model iteration and factors derived from the noise pdf parameters estimated from those residuals (here labeled C_k^{q-1} and D_k^{q-1}, but explicitly defined in Appendix 3.9, equations 3.38 - 3.40). In the case written above, a distinct noise pdf is calculated for each of the k data series (giving k distinct values of C and D). However, we can also group datasets together under the same noise distribution if that is appropriate. For ease of notation we refrain from writing that out explicitly, but note here that we often group very short RPI data with others from similar geographic regions to provide enough data points for a more robust estimate of the pdfs. The weights also incorporate a normalization factor (N_k^{q-1}) used to account for the size of the kth dataset, so that each data set (regardless of size) contributes equal weight over any specific time interval in the minimization.

3.3.4 Penalizing the Maximum Likelihood Method

We have not yet dealt with the question of how to choose p, the number of B-spline parameters. We follow the strategy outlined as item (3) at the beginning of Section 3.3, recognizing that we want a model whose resulting temporal resolution and complexity is explicitly controlled by the inversion process rather than by the number of model parameters allowed. Framed this way, we choose p to be large, then combine the ML method outlined above with the regularized weighted least squares cubic B-spline model fitting routine developed in Constable and Parker (1988), which penalizes the model roughness, $R(\hat{\beta})$, for the PADM, $\nu(t)$. $R(\hat{\beta})$

is specified in terms of the integrated squared second derivative of the resulting model:

$$R(\hat{\beta}) = \int_{t_i}^{t_n} \left[\partial_t^2 \sum_{j=1}^{p} \beta_j c_j(t) \right]^2 dt \tag{3.9}$$

A tradeoff parameter, Λ, controls the balance between minimizing roughness and minimizing the loss function ρ_k defined in the previous subsection. This adds in the penalty part of the PML algorithm. The resulting objective functional to be minimized over β and Λ is

$$U(\beta) = l_k(\beta) + \Lambda R(\beta) \tag{3.10}$$

The approach advocated by Constable & Parker (1998) for penalized splines and by Constable et al. (1987) for analogous nonlinear problems to solve for Λ generally supposes that the likelihood function corresponds to that expected for normally distributed uncertainties and an associated expected value for the rms misfit which is χ^2 distributed. A side constraint is imposed with

$$[l_k(\beta)] = T$$

with T chosen so that for misfit normalized by uncertainty the expected value of the misfit corresponds to that for the χ^2 distribution when the data uncertainties are independently and identically Gaussian distributed. Here we have a more complex likelihood function associated with the APD pdfs and knowledge of the relative uncertainty of the various data contributions may be derived empirically during the fitting procedure. A more robust approach to determining a suitable value for Λ is on the basis of recovering an appropriate frequency resolution for the model. This is not an arbitrary choice but draws on relevant literature which investigated the reliability of RPI records, especially given their age uncertainties, to choose an appropriate target resolution for our model. A visual inspection of the frequency spectrum of the model is used to settle on a value of Λ and corresponding value of T which gives the target resolution.

3.3.5 The Complete Algorithm

The flowchart in Fig. 3.7 shows the complete iterative PML algorithm. First we fit a low resolution penalized spline model to the sparse absolute paleointensity data using a 2-norm or regular least squares misfit measure (PLS spline in Fig. 3.7). We use this to predict a PADM value at every time point where we have RPI data, then estimate the scale (ζ_k) needed to transform each RPI series into pseudo-absolute VADMs. From there, we solve the PML equations above, where the 0th iteration is a Least Squares fit to find an initial set of residuals from which pdf parameters and new PML weights can be estimated. We then iteratively find residuals, noise pdfs, weights, and updated models until the model stops changing significantly (in practice, we iterate 5 times at which point the model norm changes less than 1%). Note that each updated PML model is regularized, and the tradeoff parameter needed for a target misfit is also estimated through an iterative process as in Constable and Parker (1988). At that point we have the option of recomputing the scale values using the updated PML model, and re-running the PML fitting routine with the updated scale values. Rescaling once or twice is often useful since the initial scales are calculated from a low resolution model, which may not provide an adequate initial estimate for the true VADM. We note that there is no guarantee of convergence in the scaling procedure, but in practice this has not been a problem.

3.4 Results

We apply the PML algorithm to the API data and to two compilations of RPI data and generate two distinct models, PADM2Mp and PADM2M, which are compared before we turn to a more general discussion. In both cases, we treat API data from igneous and archeological sources as data sets with distinct noise distributions because Ziegler et al. (2008) found that these data types were statistically different and have differing temporal distributions and resolutions.

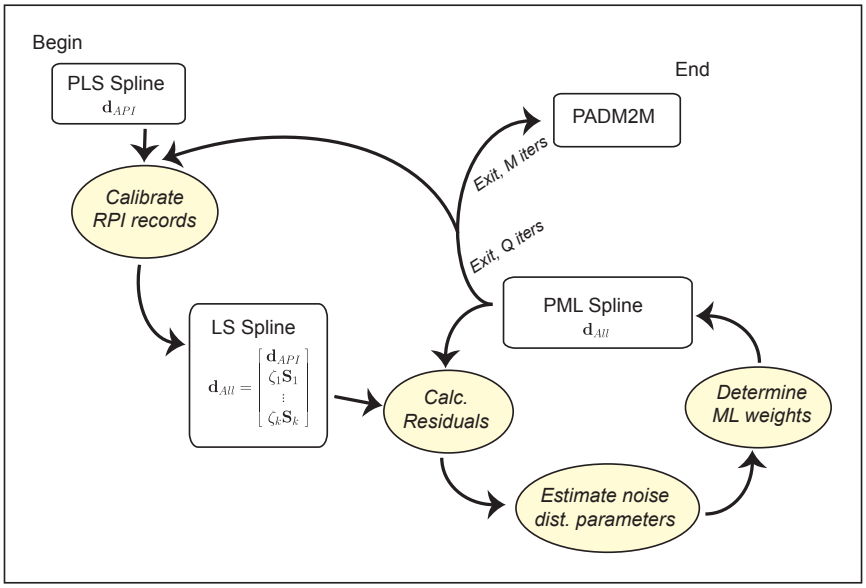

Figure 3.7: Flowchart of computational algorithm used in this study. See text, Section 3.3.5 for details.

For each model we specify up front the density of spline knot points, the target misfit, and the maximum number of iterations for (i) scale value estimation (ii) noise distribution estimation and (iii) tradeoff parameter estimation. The appropriate number of iterations involved in estimating the tradeoff parameter and noise distributions is straightforward (we iterate 5 times in each case). We rescale twice for reasons discussed in Section 3.3.5. Both models are made using 2000 knot points (1 per kyr), providing a sufficient number of parameters to ensure that the temporal resolution is controlled by the regularization. The regularization needed is specified by the target misfit, T, and is less obvious. We turn to the frequency domain to address this issue. McMillan et al. (2002) showed that due to age uncertainties in sediments, intensity variations on timescales less than 10 kyr are difficult to resolve from this data source. We therefore choose the amount of regularization (through Λ) in each case which suppresses energy at timescales of 5-10 kyr (frequencies less than 2-1 $\times 10^2 Myr^{-1}$), and judge from the power spectrum of the resulting model that this is criterion is met. Since the value of Λ in equation

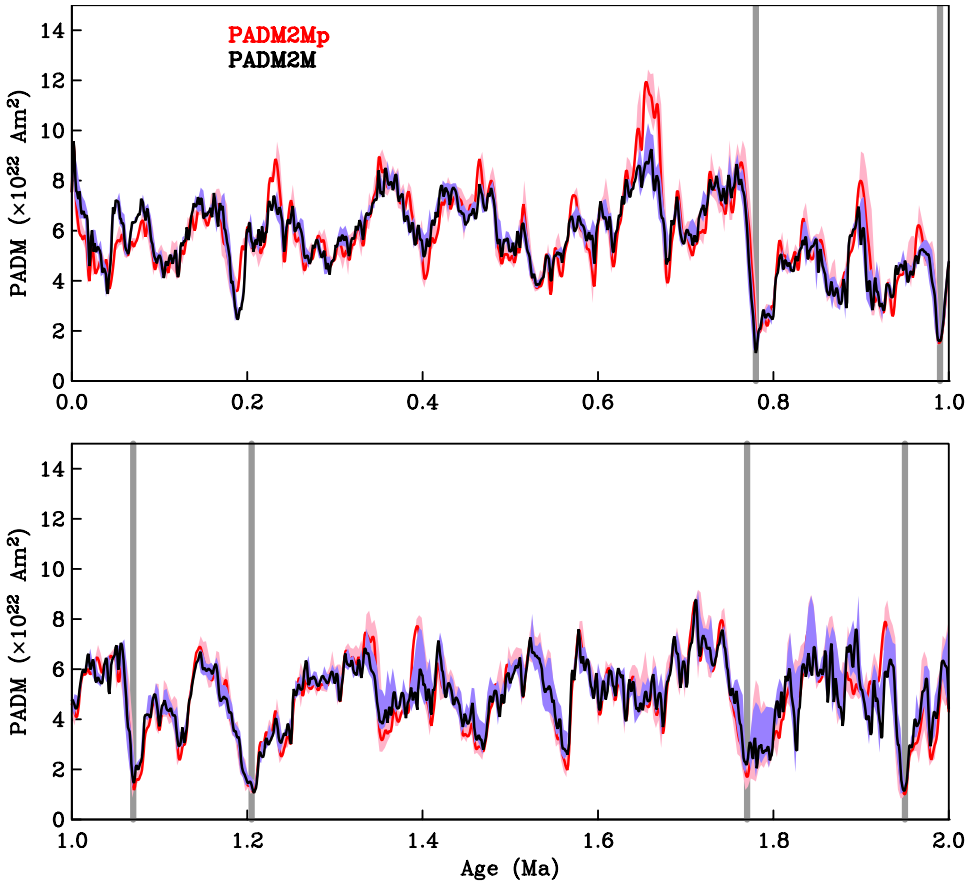

Figure 3.8: PADM2Mp model (red), made from a subset of nine RPI time series and API data. Pink shading represents upper and lower jacknife bounds on PADM2Mp (see text). PADM2M in black, with bounds in blue-gray shading. Gray bars indicate known reversals. (Top) 0-1 Ma. (Bottom) 1-2 Ma.

(10) needed to meet this criterion is not known *a priori*, we look at a range of models incorporating differing levels of smoothing and their power spectra (not shown here) to choose the most appropriate regularization parameter.

The first model discussed, PADM2Mp, is a preliminary model using only 9 of the available RPI time series (Section 3.4.1). The second, PADM2M, is our preferred model from a more complete set of RPI records (Section 3.4.2). Both are plotted in Fig. 3.8, and discussed below.

3.4.1 PADM2Mp

PADM2Mp is a preliminary time-varying, 0-2 Ma PADM model created using the P0 subset of nine globally distributed RPI data sets (see table 3.1), together with the PINT08 and Geomagia50 API data sets. These RPI records, already shown in Fig. 3.4, each span more than 1.5 million years, and have significant amounts of data both before and after the Brunhes/Matuyama reversal. They provide a good starting point for using the PML algorithm on a real data set, characterizing uncertainties in the model, and comparing features of the Brunhes and Matuyama chrons (Section 3.5).

PADM2Mp is shown in red in Fig. 3.8 and shows the expected lows at field reversals and excursions and estimates the current field strength to within 1% ($\nu(0) = 7.55 \pm .09 \times 10^{22} Am^2$, where the true value is $7.6 \times 10^{22} Am^2$). Uncertainties have been estimated using a delete-1 jacknife procedure, where we recreate a model nine times leaving out one of the nine RPI records each time. The PADM2Mp uncertainties plotted in Fig. 3.8 are the minimum and maximum value of the suite of jacknife models at any given time. Uncertainties quoted are $\pm 2\sigma$ of the values instead of the minimum and maximum. The uncertainties illustrate both the consistency of the datasets and that PADM2Mp is not predominantly controlled by any one dataset. The areas of highest variability are in sections of the model older than 1.5 Myr.

We evaluate the effectiveness of our modeling by calculating the variance reduction for each data set individually and find that values for the RPI series range from 21% to 42%, and the PINT08 and Geomagia50 API datasets have variance reductions of 34% and 30% respectively. Variance reduction is limited by poor age controls for some data and by high resolution signal recorded in data but inaccessible in million year field modeling.

PADM2Mp successfully shows the viability of PML modeling. We turn now to a model using all available information.

3.4.2 PADM2M

We created a model using our PML routine, the PINT08 and Geomagia50 API data, and 86 RPI records from the compilation discussed in Section 3.2. After obtaining an initial model using this dataset, we found that 10 RPI series have negative variance reduction (i.e. there is more variance in the residuals after a fit than in the raw data), indicating that these data series are incompatible with the model. These RPI records, discussed further in Section 3.5, are marked with an asterisk in table 3.1 and are eliminated from our preferred model.

The remaining 76 relative paleointensity records and API data are used to produce PADM2M (Paleomagnetic Axial Dipole Moment for 0-2 Ma). The model provides a reasonable fit to the data, with variance reductions of 31% and 24% for PINT08 and Geomagia50 data sets respectively, and variance reductions ranging from -4% to 62% for the RPI datasets, with a median of 22%. Three more RPI records have a slightly negative variance reduction after the fit to 76 records, but we refrained from iterating the process of trimming data and refitting. Variance reduction for all RPI data are listed in table 3.1 for reference. For the 10 records eliminated from the final model, the variance reduction listed in parenthesis is in relation to the 86 record model. The range of agreement between the model and individual RPI data sets reflects RPI quality, but also differences in temporal resolution between the model and each time series. Uncertainties are found in the same manner as described for PADM2Mp.

PADM2M reproduces the current field to within 1% ($\nu(0) = 7.55 \pm .05 \times 10^{22} Am^2$) and shows intensity lows at reversals and excursions (Fig. 3.8). While incorporating a much larger dataset, PADM2M generally agrees with the preliminary model made from only nine long records at most time periods. The most notable difference occurs between approximately 600 and 700 ka, where an intensity peak seen in PADM2Mp is muted in PADM2M. The larger global compilation of 23 records used in PADM2M should give a more reliable result than the subset of nine used in PADM2Mp. In the youngest part of the models ($<$ 100 ka), where

PADM2M adds many tens of RPI series, there are also some moderate differences between the preliminary model and PADM2M.

3.5 Discussion

3.5.1 Comparison to VADM models

In Fig. 3.9 we compare PADM2M with two published VADM models, Sint-2000 (Valet et al., 2005) and PISO-1500 (Channell et al., 2009). PISO-1500 is a scaled stack of 13 RPI records. Sint-2000 is a composite of a 33 RPI series stack (0-800 ka) and a 10 RPI series stack (800-2000 ka). PISO-1500 has a noticeably different variance and resolution from Sint-2000 and PADM2M (Fig. 3.9) because it is constructed from RPI records of higher sedimentation rates. All models show lows at reversals and excursions, and share similar long-period behavior, but with a few differences.

In comparison to Sint-2000, particularly in the Brunhes chron, PADM2M tends to peak at lower amplitudes. This is in part because our PML method addresses and, unlike the VADM stacks, accounts for bias in VADM data. From 600-700 ka, where PADM2M and PADM2Mp disagree most, both Sint-2000 and PISO-1500 show the more pronounced peak in field strength seen in PADM2Mp. For this time period, PADM2M incorporates more than twice as many RPI records as the Sint-2000 and PISO-1500 stacks (23, 10, and 6 RPI records used respectively). For this particular feature, the amplitude difference is due both to our PML method and to PADM2M's incorporation of a larger global dataset.

In the older part of the models (> 1.3 Ma) the timing of some features differ among Sint-2000, PISO-1500 and PADM2M. We note that PADM2M uses published age models for most RPI data, except for some minor age recalibrations to use consistent ages for reversal boundaries (see Section 3.2). Sint-2000 correlates some intensity minima before stacking (Valet et al., 2005), and PISO-1500 uses the Match protocol of Lisiecki and Lisiecki (2002) to correlate intensity and

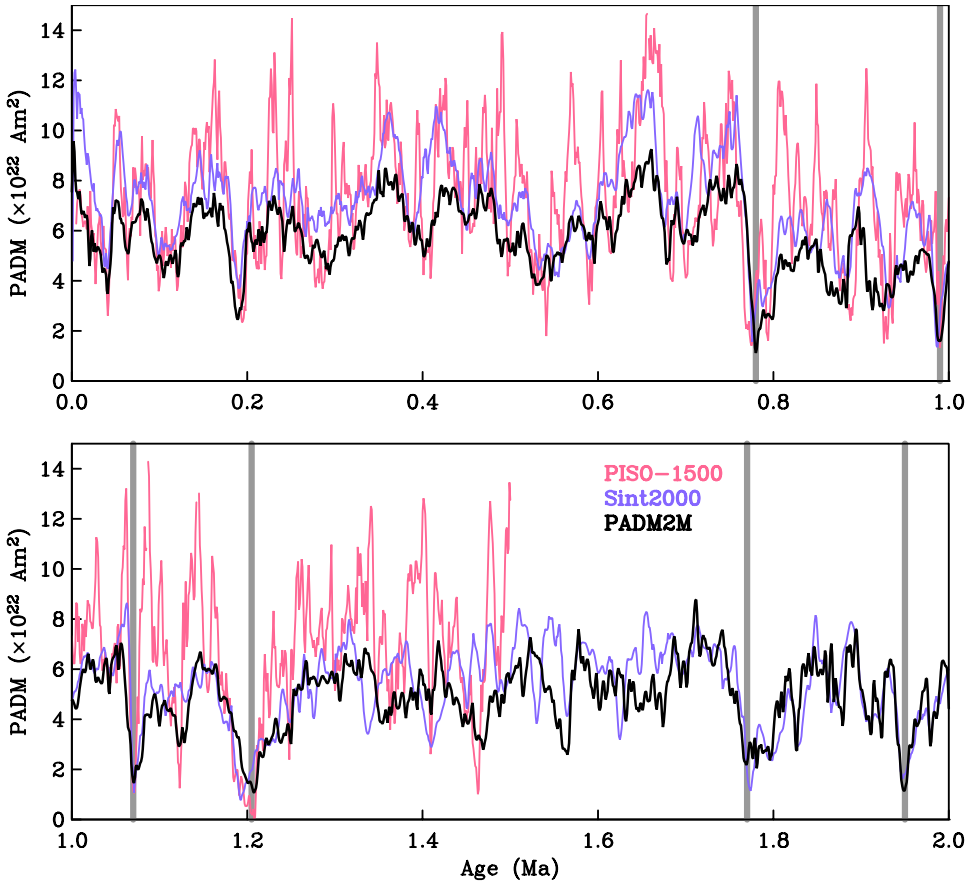

Figure 3.9: PADM2M (black) plotted with Sint-2000 (blue) and PISO-1500 (red) models. Gray bars indicate known reversals. (Top) 0-1 Ma. (Bottom) 1-2 Ma.

oxygen isotope information before stacking. The timing differences reflect these methodology differences. We prefer to avoid geomagnetic tuning, so that our age scale is independent of RPI data.

Finally, because the other models are made from RPI data only (which weakly constrain the most recent field behavior because tops of cores are often missing or damaged in the coring process) and PADM2M incorporates well-dated recent API data, PADM2M is better suited to recover estimates of the current field strength. PISO-1500 does not model 0-5 ka field strength; Sint-2000 does not model 0-1 ka and has a low VADM of $4.8 \times 10^{22} Am^2$ for $t = 1$ ka, but has more reasonable field values starting at 2 ka.

3.5.2 Statistical Analysis of PADM2M

Table 3.2 gives some statistics of PADM2M, including the mean and standard deviation of the full 0-2 Ma model, the Brunhes chron, and the Matuyama chron younger than 2 Ma. PADM2M has a mean field strength of $5.3 \times 10^{22} Am^2$ for the last 2 Ma and a standard deviation of $1.5 \times 10^{22} Am^2$. There is a difference in mean between the Brunhes and older portion of both the PADM2M and PADM2Mp of $1.4 \times 10^{22} Am^2$ (see Table 3.2). For PADM2M (evaluated every 1 ka), the average Brunhes model, and average upper and lower model bounds are 6.2, 5.9 and $6.5 \times 10^{22} Am^2$; for the 0.78 - 2 Ma Matuyama segment, these numbers are 4.8, 4.5 and $5.4 \times 10^{22} Am^2$. The non-overlapping bounds show that the means of the Brunhes and Matuyama chrons are distinctly different. PADM2Mp shows similar non-overlapping bounds. This result is consistent with the conclusions of Valet et al. (2005) for Sint-2000, but with a smaller difference in mean PADM for the two chrons (1.4 vs. $2.3 \times 10^{22} Am^2$). For PISO-1500 the difference in chron means is $0.7 \times 10^{22} Am^2$, and is considered statistically insignificant. For perspective, Table 3.2 also lists means over these time ranges for the preliminary PLS low resolution model fit, the first step of our PML algorithm. This preliminary estimate is made only from API data and does not include the ML estimation, hence the overall higher mean values. Yet the PLS spline also shows a substantial difference in Brunhes/Matuyama means (of $1.9 \times 10^{22} Am^2$). The difference in means seen in PADM2M and Sint-2000 is not confined to the RPI datasets. This is important because it rules out possible VRM contamination of RPI records as a source of differences in the Brunhes/Matuyama chron means.

The lowest value of PADM2M is $1.08 \times 10^{22} Am^2$ and occurs at 1.208 Ma (the Cobb Mountain Excursion), with other reversals having similar lows. The highest PADM2M of $9.7 \times 10^{22} Am^2$ occurs at 2 ka; the highest value outside the last few thousand years is slightly lower at $9.3 \times 10^{22} Am^2$ and occurs at 0.657 Ma. Many of the highest values of 0-2 Ma API derived VADMs in the PINT08 database are from 2-3 ka as well, indicating that the intensity peak of 2-3 ka may be the

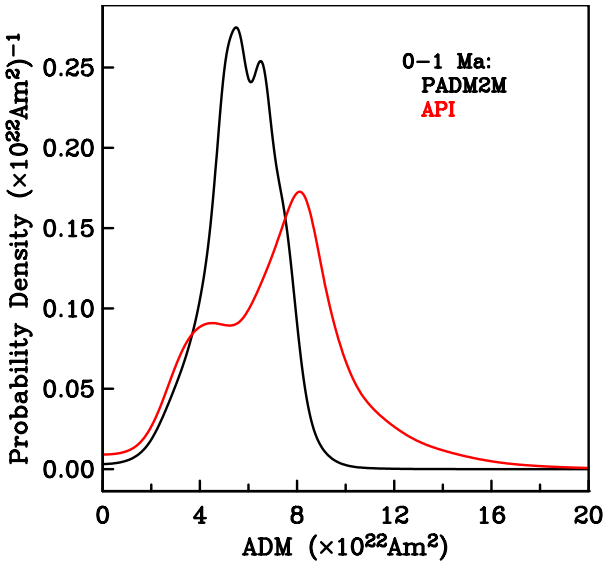

Figure 3.10: 0-1 Ma axial dipole moment distribution for PADM2M (black), along with 0-1 Ma axial dipole moment distribution from API data found in Ziegler et al. (2008) (red).

high point of the last 2 million years. Some individual archeointensities also show a very high field at this age (see e.g. Ben-Yosef et al. (2009)). However, the first few thousand years of our model are constrained primarily by API data, which can capture the true high frequency variation of the field in this time interval better than the inherently smoothed RPI records that constrain most of the model. This limitation of low sedimentation rate RPI data makes it unlikely that they can fully recover the true magnitude of older peaks.

Fig. 3.10 compares the distribution of the PADM2M model with the API distribution from Ziegler et al. (2008) for 0-1 Ma. As expected, the model distribution shows a smaller variance, because high frequency field variations are averaged out by the sedimentary processes and lost in model fitting. In the case of PADM2M, resolution is on the order of 10 kyr. The model pdf shows a variation of the slightly bimodal distribution seen in the API distribution, supporting the conclusions in Ziegler et al. (2008) that this feature is likely an accurate representation of the true distribution and temporal variations of 0-1 Ma intensities rather than an artifact generated by subsets of poor quality data.

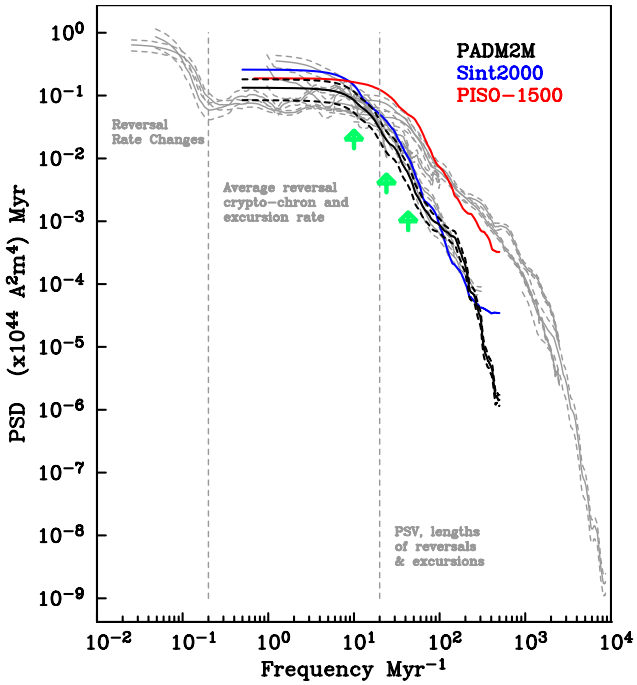

Figure 3.11: Power spectral density function of PADM2M (black), Sint-2000 (blue) and PISO-1500 (red) plotted on top of the composite paleomagnetic power spectrum of Constable and Johnson (2005) (gray). Dashed lines represent $\pm 2\sigma$ bounds. Green arrows indicate frequencies of 23, 41 and 100 kyr, corresponding to orbital periods.

3.5.3 Power spectrum

We calculate the power spectrum of PADM2M, both to look for any signals associated with orbital frequencies and to compare it with the paleomagnetic power spectrum Constable and Johnson (2005) constructed from several separate field models and sediment records. The PADM2M spectrum is calculated using the same multi-taper spectral estimation techniques described in Constable and Johnson (2005).

Plotting the PADM2M spectrum along with the paleomagnetic power spectrum (Fig. 3.11), we see that the PADM2M spectrum lies on top of portions corresponding to moderate resolution sediment records. At frequencies higher than $10^2 Myr^{-1}$, the slope of the spectrum is proportional to f^{-8} which reflects the power spectrum associated with the effective filter of the smoothing spline regularization (Constable and Parker, 1991) and is not characteristic of the data. As

mentioned in section 3.4, we have intentionally chosen an amount of regularization which filters out these high frequencies, considering them unreliably estimated by the currently available data. We calculate and plot the power spectra of Sint-2000 and PISO-1500 for comparison. Sint-2000 has a power spectrum similar to PADM2M, whereas PISO-1500 has additional energy at higher frequencies because it is constructed from higher resolution, geomagnetically-tuned sediment records and agrees with the portion of the paleomagnetic power spectrum constructed from high resolution sediment records.

Some authors have seen a correlation between orbital cycles (i.e. eccentricity, obliquity, and precession) and relative paleointensity records (e.g. Channell et al. (1998); Channell and Kleiven (2000); Yamazaki and Kanamatsu (2007)). The PADM2M spectrum has no peaks in power at orbital cycle frequencies (e.g. periods of 23, 41 or 100 kyr), or at any others. Therefore, our model, in agreement with other VADM models like PISO-1500 (Channell et al., 2009), shows no obvious connection between orbital cycles and geomagnetic field behavior.

3.5.4 Anomalous Data

In section 3.4, we found that some records strongly disagreed with the PADM2M model. From visual assessment, most of these anomalous records seemed similar to the model, except that the ages of peaks and lows would often be offset from those of the model. This indicates that misfit has more to do with timing errors than errors in paleointensity measurements. Some rock magnetic information from sediments in regions producing the anomalous RPI data suggest the data are possibly affected by reduction diagenesis, and record a lag between the age of the sediments and the age of remanent magnetization acquisition (e.g. (Rowan et al., 2009; Stoner et al., 2003)). Because our ML method attributes the noise to intensity uncertainties, and explicitly uses the pdf associated with the noise/residuals in the estimation procedure, it was inappropriate to use these data with this method. However, efforts to incorporate timing uncertainties into future methods might

allow for the use of these records.

Six of the rejected RPI series are categorized as LR and four are YR (see table 3.1). Of the six LR, four are from the southern hemisphere - whereas 8 of the total 34 LR are southern hemisphere. This disproportionate misfit of southern hemisphere records may indicate that there are real regional differences in paleointensity signals, in addition to or instead of only timing errors. An investigation of this is beyond the scope of this paper, but suggests that it might be useful to make separate regional models using our PML method and compare the results.

3.6 Conclusions

We have developed a method for efficiently generating paleomagnetic axial dipole moment models from a joint set of absolute paleointensity data and many relative paleointensity time series. The use of penalized maximum likelihood fitting criteria minimizes the influence of outliers and avoids bias in the fit due to the asymmetric noise associated with paleomagnetic data. We generate PADM2M, a time-varying, 2 million year model with 5-10 kyr resolution, and confirm that it often agrees both with the data and with other recent axial dipole moment models, with some notable differences discussed in Section 3.5.

We find that the Brunhes chron shows a mean about 20% higher than that for the Matuyama, but note that our model does not cover the entire Matuyama chron. This result was seen in our PADM2M model, in the 9 record version (PADM2Mp) made from very long RPI records, which have significant amounts of data both before and after the reversal, and in an interim model based only on API data so we are confident the observation is not a result of our scaling or modeling procedures. Field strength models alone cannot resolve whether this reflects any difference in geodynamo processes during the two chrons or whether it is simply an observation of non-stationarity of the field over 2 Myr intervals.

The power spectrum of PADM2M shows no extra power at orbital fre-

quencies, indicating that the field strength has no strong correlation with orbital forcing. A comparison with the paleomagnetic power spectrum of Constable and Johnson (2005) shows that as expected, some high frequency energy is lost through the process of finding a best fitting model to a highly variable set of data.

Our modeling efforts were able to incorporate both API data and RPI datasets with a range of lengths, sedimentation rates (and therefore, resolutions) and global locations. We examined quantitatively how well each dataset fit with a resulting model, and found a subset of records which fit poorly. Although we eliminated these records from our final model, we do not conclude that they are simply 'bad' data or unusable. Rather, this result points to the need to address timing uncertainties and more complicated geographic structure in future paleomagnetic field models.

3.7 Acknowledgments

We are grateful to Ivana Komunjer for code and helpful discussions regarding APD functions. Peter Spellucci provided the optimization subroutine donlp2 which was incorporated in the PML routine to calculate APD parameters. We thank Toshi Yamazaki and an anonymous reviewer for their constructive comments on the manuscript, which improved this article. This work was supported under NSF grant EAR-0809709. CLJ acknowledges support from NSERC.

Chapter 3, in full, is a reprint of the material as it appears in L. B. Ziegler, C.G. Constable, C. L. Johnson, and L. Tauxe (2011), PADM2M: A Penalized Maximum Likelihood Model of the 0-2 Ma Paleomagnetic Axial Dipole Moment, Geophysical Journal International. The dissertation author was the primary investigator and author of this paper.

3.8 Appendix: Bias due to Noise in estimating Axial Dipole Moment from VADM data

Intensity data are converted by a linear transformation to Virtual Axial Dipole Moment (VADM) data through the geocentric-axial-dipole (GAD) field assumption, with non-axial-dipole (NAD) intensity contributions, measurement, and recording error manifesting as noise in the VADM data. This noise is often implicitly assumed to be gaussian - or at least symmetric - with a mean of zero. In paleomagnetic studies VADM noise is generally treated as being zero-mean gaussian so that on average, VADM is thought to represent the true axial dipole moment. We show below that the true paleomagnetic axial dipole moment (PADM) is non-linearly related to field intensity. Because of this non-linearity, VADMs produce a biased estimate of axial dipole moment.

We derive here the relationship between field intensity ($|B(t)|$) and axial dipole strength (g_1^0), including a consideration of NAD and other implicit noise. At any given location we express the measured squared field strength as:

$$\begin{aligned} B^2(r,\theta,\phi,t) = B^2(t) &= (B_r(t)^2 + B_\theta(t)^2 + B_\phi(t)^2) && (3.11) \\ &= (k_r g_1^0(t) + R)^2 + (k_\theta g_1^0(t) + T)^2 + (H)^2 && (3.12) \end{aligned}$$

where $k_r = 2\cos\theta$ and $k_\theta = \sin\theta$, and R, T, H are independent random variables which express non-axial-dipole contributions to the field strength. They might be Gaussian, but relaxing that restriction allows for a more flexible approach to noise contributions. For now, we can suppose that $E[R] = E[T] = E[H] = 0$ and has no time variation (implying NAD vector field contributions average to zero).

Taking (3.12) and expanding the RHS we get a quadratic equation that can be solved for $g_1^0(t)$, namely:

$$(k_r^2 + k_\theta^2)[g_1^0(t)]^2 + 2(k_r R + k_\theta T)g_1^0(t) + R^2 + T^2 + H^2 - B^2(t) = 0 \qquad (3.13)$$

Solving for $g_1^0(t)$ we find

$$g_1^0(t) = \pm\frac{B(t)}{(k_r^2+k_\theta^2)^{1/2}}\left[1-\frac{(R^2+T^2+H^2)}{[B(t)]^2}+\frac{k_rR+k_\theta T}{[B(t)]^2(k_r^2+k_\theta^2)}\right]^{1/2}-\frac{k_rR+k_\theta T}{(k_r^2+k_\theta^2)} \tag{3.14}$$

and invoking the binomial expansion

$$g_1^0(t) \approx \pm\frac{B(t)}{(k_r^2+k_\theta^2)^{1/2}}\left[1-\frac{(R^2+T^2+H^2)}{2[B(t)]^2}+\frac{k_rR+k_\theta T}{2[B(t)]^2(k_r^2+k_\theta^2)}+\cdots\right]-\frac{k_rR+k_\theta T}{(k_r^2+k_\theta^2)} \tag{3.15}$$

Transforming the axial dipole intensity, $g_1^0(t)$, into axial dipole moment is just a matter of multiplicative constants:

$$PADM(t) = \nu(t) = \frac{4\pi r^3}{\mu_0}g_1^0(t) \tag{3.16}$$

with Earth average radius $r = 6371km$ and $\mu_0 = 4\pi\times10^{-7}H/m$. Applying this to equation 3.15 and noting that $(k_r^2+k_\theta^2)^{1/2} = (1+3\cos^2\theta)^{1/2}$ gives the relationship between PADM and field intensity:

$$\begin{aligned}\nu(t) \approx \pm\ &\frac{4\pi r^3}{\mu_0(1+3\cos^2\theta)^{1/2}}\left[B(t)-\frac{(R^2+T^2+H^2)}{2[B(t)]}+\frac{k_rR+k_\theta T}{2[B(t)](1+3\cos^2\theta)}+\cdots\right]\\ &-\frac{4\pi r^3}{\mu_0}\frac{k_rR+k_\theta T}{(1+3\cos^2\theta)}\end{aligned} \tag{3.17}$$

The usual paleomagnetic VADM ($V(t)$) is

$$V(t) = \frac{4\pi r^3}{\mu_0(1+3\cos^2\theta)^{1/2}}B(t)$$

which is in fact the first (and largest) term on the RHS of the equation for PADM (3.17). However, it takes no account of the additional RHS terms. If R, T, and H are gaussian random variables with zero means, the last term would be zero on average but the other terms would not. In practice, R, T, and H are not known, but one can restate the relationship between PADM and VADM as:

$$V(t) = \nu(t) + b$$

where b is a bias term, which is a random variable of 'noise' which has a non-zero mean and an unknown (but certainly non-gaussian) distribution function.

3.9 Appendix: Penalized Maximum Likelihood Inversion

The penalized maximum likelihood algorithm follows the outline given in Section 3.3.5 and presented in the flowchart of figure 3.7. In Section 3.9.1 we outline how the PML method would be applied to a single time series of absolute paleointensity data with a common noise distribution, then in Section 3.9.2 discuss additional complexity associated with incorporating and calibrating heterogenous sediment records of variable resolution.

3.9.1 PML for a Single (Absolute) VADM Data Series

In Step 1 we follow the algorithm of Constable and Parker (1988) to find $\nu_0(t)$, a penalized cubic B-spline model of PADM for a single (absolute) paleointensity data series. The observations $(d_i,\ i = 1, \ldots, n)$ are represented as a linear combination of cubic B-spline basis functions $c_j(t_i)$ and a noise term (ϵ_i):

$$d_i = \nu(t_i) + \epsilon_i = \sum_{j=1}^{p} \beta_j c_j(t_i) + \epsilon_i \tag{3.18}$$

where β_j are the corresponding spline coefficients, and are the initial model parameters we seek. In this first step we do not yet have an estimate for the noise distribution so the objective functional minimized over $\hat{\beta}$ is

$$U(\beta) = l_0(\hat{\beta}) + \Lambda R(\hat{\beta}) \tag{3.19}$$

with $l_0(\hat{\beta})$ corresponding to the standard 2-norm misfit measure anticipated for a least squares fit. That is

$$l_0(\hat{\beta}) = \sum_{i=1}^{n} (d_i - \nu_0(t_i))^2 = \sum_{i=1}^{n} \epsilon_i^2 \tag{3.20}$$

The model roughness, $R(\hat{\beta})$, is given by the integrated squared second derivative of the resulting spline:

$$R(\hat{\beta}) = \int_{t_i}^{t_n} \left[\partial_t^2 \sum_{j=1}^{p} \beta_j c_j(t) \right]^2 dt \tag{3.21}$$

The tradeoff parameter Λ in equation 3.19 controls the balance between fitting the data and penalizing roughness in $\nu(t)$.

The usual ML method finds the parameter estimates which maximize the probability of getting the data that were actually observed using an appropriate pdf for the noise. The function to be maximized in this case, the likelihood function, $L(\hat{\beta})$, is the joint pdf, F, of the sample errors, which is in turn the product of the individual pdfs if the errors are independent, identically distributed:

$$L(\hat{\beta}) = F(\epsilon, \hat{\beta}) = \prod_{i=1}^{n} f(\epsilon_i, \hat{\beta}) \tag{3.22}$$

Step 2 is to make a first estimate of the noise distribution $f(\epsilon)$, using the residuals of the data from $\nu_0(t)$. For a given dataset, we describe the statistical distribution of the residuals (ϵ_i) using an Asymmetric Power Distribution (APD), whose pdf function is by definition:

$$f(\epsilon_i) = \frac{\delta_{\alpha,\lambda}^{1/\lambda}}{\sigma\Gamma(1+1/\lambda)} exp\left[-\frac{\delta_{\alpha,\lambda}}{\gamma(\epsilon_i)} \left| \frac{(\epsilon_i - \mu)}{\sigma} \right|^{\lambda} \right] \tag{3.23}$$

where

$$\delta_{\alpha,\lambda} = \frac{2\alpha^{\lambda}(1-\alpha)^{\lambda}}{\alpha^{\lambda} + (1-\alpha)^{\lambda}} \tag{3.24}$$

$$\begin{aligned} \gamma(\epsilon_i) &= \alpha^{\lambda} && \epsilon_i \leq \mu \\ &= (1-\alpha)^{\lambda} && \epsilon_i > \mu \end{aligned} \tag{3.25}$$

and μ, σ, α and λ are the location, scale, and two shape parameters respectively. The shape parameter α has the range $0 < \alpha < 1$ and corresponds to asymmetry, where 0.5 means there is an equal amount of data on either side of the mode.

The second shape parameter, λ, corresponds to tail shape, and has the range $\lambda > 0$, though it is generally between 1 and 3 (see table 3.1). High values of λ mean flatter-topped distributions, with $\lambda = 2$ (and $\alpha = 0.5$) corresponding to a symmetric gaussian distribution (see Fig. 3.6). μ is unbounded, and $\sigma > 0$.

We estimate the pdf parameters (μ, σ, α and λ) of the noise empirically from the residuals resulting from iterative PML fits:

$$\epsilon_i^q = d_i - \sum_{j=1}^{p} \beta_j^{q-1} c_j(t_i) \tag{3.26}$$

where q represents the qth iteration.

The maximum of likelihood and minimum of the negative log likelihood ($l(\hat{\beta})$) coincide, so we can rewrite the problem as:

$$\max_{\hat{\beta}} L(\hat{\beta}) = \min_{\hat{\beta}} l(\hat{\beta}) = \min_{\hat{\beta}} \sum_{i=1}^{n} \rho(\epsilon_i), \tag{3.27}$$

where $\rho(\epsilon) = -ln[f(\epsilon, \hat{\beta})]$ and is termed the loss function.

Now, combining this with the APD description for f, we can define our condition to minimize as:

$$\begin{aligned} &\min_{\hat{\beta}} \; l(\hat{\beta}), \\ &\qquad l(\hat{\beta}) = \sum_{i=1}^{n} -ln[f(\epsilon_i, \hat{\beta})] \\ &\qquad l(\hat{\beta}) = \sum_{i=1}^{n} -ln\left(\frac{\delta^{1/\lambda}}{\sigma\Gamma(1+\frac{1}{\lambda})}\right) + \frac{\delta}{\sigma^\lambda \gamma^\lambda} \left|\epsilon_i - \mu\right|^\lambda \end{aligned} \tag{3.28}$$

The minimum is found where the derivatives with respect to the parameters, β_j, are zero - i.e. $\nabla l(\beta) = 0$. Using Equation 3.26, we get:

$$\frac{\partial l}{\partial \beta_j} = \sum_{i=1}^{n} \frac{\lambda\delta c_j(t_i)}{\sigma^\lambda \gamma^\lambda} \left| d_i - \sum_{j=1}^{p} \beta_j c_j(t_i) - \mu \right|^{\lambda-2} \left(d_i - \sum_{j=1}^{p} \beta_j c_j(t_i) - \mu \right) = 0 \tag{3.29}$$

Although this is non-linear it can be solved iteratively in the form of a weighted least squares problem (Constable, 1988) by rewriting the above equation as:

$$\frac{\partial l}{\partial \beta_j^q} = \sum_{i=1}^{n} w_i^q c_j(t_i) \left(\tilde{d}_i - \sum_{j=1}^{p} \beta_j^q c_j(t_i) \right) = 0 \tag{3.30}$$

$$w_i^q = \frac{\lambda \delta}{\sigma^\lambda \gamma^\lambda} \left| \tilde{d}_i - \sum_{j=1}^{p} \beta_j^{q-1} c_j(t_i) \right|^{\lambda-2} \tag{3.31}$$

$$\tilde{d}_i = d_i - \mu \tag{3.32}$$

Note, the parameters $(\mu, \sigma, \alpha, \lambda)$ and δ are all derived from the $(q-1)$th iteration as well, though the superscripts have been left off in the above notation to avoid clutter. In matrix notation we will express this as:

$$\mathbf{C}^T \mathbf{W}_q \mathbf{C} \hat{\beta} = \mathbf{C}^T \mathbf{W}_q \mathbf{d} \tag{3.33}$$

In 3.33, $\mathbf{C}$ is the design matrix of B-spline functions, $\mathbf{d}$ the vector of observations, $\tilde{d}_i$, $\hat{\beta}$ the model vector of coefficients β_j, and $\mathbf{W}_q$ is the $n \times n$ diagonal matrix of 'weights' calculated from residuals produced from the previous $(q-1)$th iteration. Successive iterations of $\hat{\beta}$ and weights are calculated until specified convergence criteria are reached. Recasting the solution of the nonlinear ML problem as an iteratively re-weighted least squares problem conveniently allows us to use the same algorithm as in Step 1 to recover a penalized maximum likelihood solution by adding the roughness penalty in Equation 3.21. Equation 3.19 is thus directly updated to include the correct likelihood function $l_q(\beta)$ for the asymmetric noise distribution expected for the absolute VADM data.

$$U(\beta) = l_q(\hat{\beta}) + \Lambda R(\hat{\beta}) \tag{3.34}$$

We call the algorithm that solves Equation 3.34 a Penalized Maximum Likelihood (PML) inversion, because of the explicit tradeoff between finding the ML solution and the penalty on roughness in the resulting model.

3.9.2 Using Relative Paleointensity Time Series in PML Models

Section 3.9.1 has described fitting a PML model to a single data series of n absolute observations of VADM with a common noise distribution. In practice, we have both spot recordings of VADM from igneous samples, and several independent time series of relative variations in VADM from sediment records. Multiple absolute data sets can be treated in the same way but with distinct noise pdfs where necessary. However, the incorporation of RPI data into our model requires appropriate choices for calibrating these data to absolute values and appropriate weightings of the contribution of series some of which are very densely sampled in time.

Calibration of RPI data

The calibration of RPI observations is a simple scaling by a multiplicative factor to transform them to absolute values of VADM. Explicitly stated, for RPI we have $d_i = \zeta_k S_{k,i}$, where $S_{k,i}$ denotes the ith data point in the kth time series and ζ_k is the scale value for the kth dataset such that equation 3.18 becomes:

$$\zeta_k S_{k,i} = \sum_{j=1}^{p} \beta_j c_j(t_{k,i}) + \zeta_k \epsilon_{k,i} \tag{3.35}$$

We estimate scale values by finding a low resolution preliminary PADM model from the sparse absolute paleointensity data. Using this model, we calculate the ratio of the model to the RPI time series at each time, and use the median of this ratio as the scale estimate. There is a small bias-correction factor (Δ_k^{m-1}) needed for non-symmetric noise, where $\bar{\epsilon} \neq 0$. These scale estimates are then recalculated m times (usually 2-3 times) after an updated ML model is made from the absolute and scaled RPI data.

$$\zeta_k^m = median\left(\frac{\sum_{j=1}^{p} \beta_j^{m-1} c_j(t_i)}{S_{k,i} - \Delta_k^{m-1}}\right) \tag{3.36}$$

Note that Δ_k^{m-1} is the difference between the mean and the mode of a given set of ϵ_i normalized by the scale value, ζ_k^{m-1}, (since ϵ_i are in essence scaled as the data are scaled).

Temporal Normalization

For RPI records, sediment type and accumulation rate directly control the resolution possible, since a finite thickness of sediment is required for paleointensity analysis. Thus, each data point in the time series provides a temporal average paleointensity over 100s or 1000s of years. Additionally, some studies of post-depositional remanent magnetization (pDRM) in sediments suggest that the process of remanent magnetization acquisition in sediments itself acts as a low-pass filter and may contribute to signal smoothing (e.g Roberts and Winklhofer (2004)). For our goal of finding a global average of dipole moment, we want each time series to contribute equally to the resulting model at any given time. We weight each sediment record so that it contributes equally over a given time range. There are two things to consider for this goal. First, high resolution records simply contain more data points over a given time range (sometimes an order of magnitude more), so we divide by the number of data (n_k) per age range (Δt) to reduce this influence. In addition to the data density being controlled by sedimentation rate, it also affects the variability of the paleointensity (and subsequently the residuals after a fit). Given that each data point is itself an average of a time interval, the longer the time interval over which it averages, the less variable the data. This influences the values of our ML weights - which are derived from a pdf. Pdfs by definition, integrate to 1, such that if there is more variance in the data, the peak ends up being lower relatively speaking, which translates into the ML weights having a different average for each time series. Therefore, we also normalize the weights by dividing by the average weight for each distribution. These normalization factors (N_k) are absorbed into the PML weights:

$$N_k = \left(\frac{\Delta t}{n_k}\right)\left(\frac{1}{\frac{1}{n_k}\sum_{j=1}^{n_k} w_{k,j}}\right) \tag{3.37}$$

3.9.3 The Combined Problem: Absolute and Relative Paleointensity Series

For the joint inversion of API and several RPI datasets, we start with the assumption that each dataset has a unique noise distribution ($f(\epsilon_i, \hat{\beta})$) and unique scale factor. For K datasets, this updates equations 3.30-3.32 into:

$$\frac{\partial l}{\partial \beta_j^q} = \sum_{k=1}^{K}\sum_{i=1}^{n_k} w_{k,i}^q c_j(t_{k,i})\left(\tilde{d_{k,i}} - \sum_{j=1}^{p}\beta_j^q c_j(t_{k,i})\right) = 0 \tag{3.38}$$

$$w_{k,i}^q = N_k^{q-1}\left(\frac{\lambda\delta}{\sigma^\lambda\gamma^\lambda}\right)_k^{q-1}\left|\tilde{d_{k,i}} - \sum_{j=1}^{p}\beta_j^{q-1}c_j(t_{k,i})\right|^{\lambda_k^{q-1}-2} \tag{3.39}$$

$$\tilde{d_{k,i}} = \zeta_k d_{k,i} - \mu_k^{q-1} \tag{3.40}$$

In matrix notation, in a scenario with $(K-1)$ RPI records and one API data set:

$$\begin{bmatrix} \mathbf{C}_1^T & & & \\ \vdots & & & \\ \mathbf{C}_{K-1}^T & & & \\ \mathbf{C}_a^T & & & \end{bmatrix}\begin{bmatrix} \mathbf{W}_1 & & & 0 \\ & \ddots & & \\ & & \mathbf{W}_{K-1} & \\ 0 & & & \mathbf{W}_a \end{bmatrix}\begin{bmatrix} \mathbf{C}_1 \\ \vdots \\ \mathbf{C}_{K-1} \\ \mathbf{C}_a \end{bmatrix}\hat{\beta} = \begin{bmatrix} \mathbf{C}_1^T & & & \\ \vdots & & & \\ \mathbf{C}_{K-1}^T & & & \\ \mathbf{C}_a^T & & & \end{bmatrix}\begin{bmatrix} \mathbf{W}_1 & & & 0 \\ & \ddots & & \\ & & \mathbf{W}_{K-1} & \\ 0 & & & \mathbf{W}_a \end{bmatrix}\begin{bmatrix} \zeta_1\mathbf{S}_1 \\ \vdots \\ \zeta_{K-1}\mathbf{S}_{K-1} \\ \mathbf{A} \end{bmatrix} \tag{3.41}$$

where $\mathbf{C}$ are cubic B-spline matrices, $\mathbf{W}$ are weight matrices and $\mathbf{A}$ and $\mathbf{S}$ are data vectors of absolute and relative paleointensities respectively. $\hat{\beta}$ is the vector of model parameters: the coefficients for the B-splines.

Table 3.1 Relative Paleointensity records used in PADM2M

Core Name	**Lat.** (^{o})	**Lon.** (^{o})	**Min. Age** (kyr)	**Max. Age** (kyr)	**Sed Rt.** (cm/kyr)	n	α, λ	**variance reduc. (%)**	**Ref**
P0 Records									
ODP 983	61.4	-24.1	0	1888.9	16	16859	0.18, 2.06	22	1,2,3,4,5
ODP 984	60.4	-23.6	0	2151.9	12	16843	0.25, 2.21	32	2,4,5
ODP 1021	39.08	-126.22	13.4	1562.1	3	1869	0.50, 2.12	53	6,7
ODP 1010	29.97	-118.1	19.0	2036.0	1	1859	0.35, 1.62	30	6,8
MD97-2143	15.87	124.65	0	2140.0	2	1224	0.40, 1.77	37	9
MD98-2187	4.27	134.99	50.5	3052.7	1	831	0.32, 1.88	20	10
MD98-2185	3.08	134.99	8.9	2256.2	2	1605	0.44, 1.73	17	10
ODP 848-851	2	-110	33.5	4035.3	2.5	1312	0.19, 1.63	34	11
MD90-0940	-5.56	61.67	107.8	1954.4	< 2	977	0.34, 1.50	21	12
Long Records									
ps1852-2	70.26	-15.83	3.5	283.3	2	258	0.15, 1.30	12	13
ldb	45	4	19.45	307.57	15	428	0.22, 1.79	12	14,15

(continued)

Table 3.1 (continued)

Core Name	**Lat.** (^{o})	**Lon.** (^{o})	**Min. Age** (kyr)	**Max. Age** (kyr)	**Sed Rt.** (cm/kyr)	n	α, λ	**variance reduc. (%)**	**Ref**
md95-2039	40.58	-11.00	29.6	317.4	7-25	1347	0.33, 1.62	23	16
md95-2040	40.58	-10.00	32.8	401.8	7-25	1409	0.22, 1.93	16	16
ngc69	40.00	175.00	6.87	883.02	1	229	0.48, 1.30	47	17
ded8708	39.37	13.34	39.5	405.6	10	192	0.22, 1.79	-1	18
su92-17	39.37	-26.60	4.4	280.0	2.4	690	0.57, 1.51	11	19
*lc07	38.15	10.07	754.0	1033.0	2.3	584	-	(-31)	20
su92-18	37.78	-27.22	4.4	280.0	3.5	690	0.26, 1.54	23	19
su92-19	37.3	-27.08	4.4	278.8	3	687	0.16, 2.26	21	19
ngc65	35.24	175.00	6.5	634.9	1	130	0.42, 2.49	35	17
rc10-167	33.03	150.38	10.7	781.1	2.1	722	0.34, 1.36	2	21
kk78-030	18.9	-160.3	601.3	1785.4	2	1636	0.22, 1.01	7	22
769	8.78	121.30	5.0	1106.0	8	719	0.46, 2.18	7	23,24
767	4.78	123.5	601.0	1518.2	10	530	0.22, 1.08	9	25,26

(continued)

Table 3.1 (continued)

Core Name	**Lat.** (^{o})	**Lon.** (^{o})	**Min. Age** (kyr)	**Max. Age** (kyr)	**Sed Rt.** (cm/kyr)	n	α, λ	**variance reduc. (%)**	**Ref**
kh90-3-5	4.00	160.02	5.0	1106.0	1	1102	0.44, 1.69	37	27
807a	4.0	157.0	781.14	2036.4	-	475	0.14, 2.57	29	28
np35	3.80	141.49	126.7	697.9	1	221	0.39, 2.14	5	29
p226	2.88	-169.58	40.6	780.0	0.6	195	0.51, 1.76	20	29
kh73-4-7	2.69	164.84	2.0	1160.0	1	1159	0.33, 1.43	2	30
*803a	2.26	160.30	783.0	1396.0	1	1396	-	(-24)	28
803b	2.26	160.3	1487.9	2786.3	1	173	0.27, 1.38	-2	28
md97-2140	2.05	141.76	568.3	1465.1	1	680	0.14, 2.57	39	31
md98-2183	2.01	135.02	19.9	1193.0	2	3361	0.47, 1.55	30	10
rndb75p	1.9	160.2	123.7	1193.0	1	795	0.40, 1.58	7	32
ngc36	1.22	160.57	0.8	546.0	1	106	0.36, 1.31	12	29
kh73-4-8	-1.55	167.64	36.0	1160.0	1	1125	0.35, 1.39	27	30
*e113p	-1.64	159.22	4.4	379.6	1.3	557	-	(-63)	33

(continued)

Table 3.1 (continued)

Core Name	**Lat.** (^{o})	**Lon.** (^{o})	**Min. Age** (kyr)	**Max. Age** (kyr)	**Sed Rt.** (cm/kyr)	n	α, λ	**variance reduc. (%)**	**Ref**
kr9912-pc5	-9.35	-162.83	1294.5	2117.7	0.3-1.5	260	0.37, 1.40	-4	10
*kr9912-pc2	-10.75	-163.49	1003.9	2999.2	0.3-1.5	980	-	(-15)	10
ngc38	-14.99	175.16	9.5	405.5	1	71	0.36, 1.31	46	29
*ks87-752	-37.75	-38.05	600.4	1022.6	-	283	-	(-29)	34
*1089	-40.94	9.89	20.1	578.3	15-20	8073	-	(-56)	35
1101	-64.37	-70.27	706.3	1105.0	7	800	0.30, 1.47	17	36
Young Records									
ps2644-5	67.87	-21.77	11.5	76.0	37	636	0.33, 1.48	30	37,38
md95-2009	62.74	-3.99	10.3	76.0	33	648	0.42, 2.53	34	37,38
su90-24	62.67	- 37.38	11.0	76.0	32	641	0.23, 3.07	17	37,38
su90-33	60.57	-22.09	11.5	76.0	11	636	0.23, 1.19	2	37,38
ver98-1-6	53.69	108.35	64.5	234.5	4.3	356	0.35, 2.71	4	39
305-a5	53.0	106.0	0.4	10.8	12	27	0.35, 2.71	22	40

(continued)

Table 3.1 (continued)

Core Name	**Lat.** (^{o})	**Lon.** (^{o})	**Min. Age** (kyr)	**Max. Age** (kyr)	**Sed Rt.** (cm/kyr)	n	α, λ	**variance reduc. (%)**	**Ref**
BaikalStack	53.0	106.0	12.8	83.8	12	199	0.35, 2.71	28	40
884	51.45	168.34	16.2	210.0	5	864	0.32, 2.57	37	41
883	51.20	167.77	16.2	210.0	5	863	0.32, 2.57	37	41
882b	50.36	167.60	0.9	204.9	4	63	0.32, 2.57	31	42
*md95-2024	50.20	-45.69	1.5	117.0	22	2407	-	(-9)	43
su9003	40.51	-32.05	7.3	231.6	5	617	0.33, 1.18	24	44
ket8251	39.48	14.17	7.9	95.2	5	71	0.22, 1.79	12	18
ded8707	39.41	13.35	9.8	59.7	10	192	0.22, 1.79	30	18
md01-2440	37.8	-10.0	2.2	54.5	15-35	304	0.20, 1.91	8	16
*md01-2441	37.8	-10.0	28.5	53.7	15-35	301	-	(-17)	16
md95-2042	37.8	-10.0	31.7	160.9	15-35	399	0.29, 1.70	13	16
*md99-2334	37.8	-10.0	0.2	37.6	15-35	236	-	(-38)	16
md84-629	36.04	33.08	15.5	58.6	12	201	0.28, 2.01	26	18

(continued)

Table 3.1 (continued)

Core Name	**Lat.** (^{o})	**Lon.** (^{o})	**Min. Age** **(kyr)**	**Max. Age** **(kyr)**	**Sed Rt.** **(cm/kyr)**	n	α, λ	**variance** **reduc. (%)**	**Ref**
md95-2034	33.69	-57.58	11.5	76.0	40	636	0.22, 1.19	2	37,38
ch88-10p	29.0	-73.0	14.2	67.8	22	315	0.40, 2.14	5	45
Sed-17aK	25.28	-17.11	8.4	223.8	4-13	344	0.20, 1.91	10	46
768a	8.0	121.22	5.1	94.2	10	73	0.42, 1.97	34	24
768b	8.0	121.22	9.3	130.3	10	105	0.42, 1.97	20	24
*md98-2181	6.30	125.83	11.8	65.7	45	514	-	(-6)	47
ngc29	4.13	136.27	2.3	192.1	1-10	74	0.28, 1.83	49	48
md85-674	3.19	50.44	18.2	138.3	10	284	0.26, 1.25	35	49
ngc26	3.00	135.02	1.2	119.7	1-10	74	0.28, 1.83	44	48
md85-669	2.49	46.92	20.1	138.0	5	239	0.20, 1.20	22	49
ngc16	2.00	135.00	1.6	191.2	1-10	125	0.28, 1.83	30	48
np7	2.00	138.01	5.7	199.4	1-10	70	0.28, 1.83	41	48
np5	1.01	136.96	8.5	196.4	1-10	132	0.28, 1.83	23	48

(continued)

Table 3.1 (continued)

Core Name	**Lat.** (^{o})	**Lon.** (^{o})	**Min. Age** (kyr)	**Max. Age** (kyr)	**Sed Rt.** (cm/kyr)	n	α, λ	**variance reduc. (%)**	**Ref**
md85-668	-0.02	46.04	20.9	187.3	5	191	0.29, 1.36	14	49
21-pc02	-41.14	7.81	0.5	80.7	13.5	1450	0.44, 2.19	39	35,50,51
md84-528	-42.11	53.04	15.6	94.0	12	927	0.36, 1.43	10	18
BM Rev. Recs									
609b	49.86	-24.23	777.1	824.9	7	176	0.28, 1.30	62	52
606a	37.00	-37.00	773.0	792.0	-	70	0.28, 1.30	7	53
767b	4.78	123.5	758.8	828.8	8	58	0.28, 1.30	19	25,26
665a	3.0	-20.0	770.3	817.3	4	38	0.28, 1.30	47	52

(continued)

Table 3.1 (continued)

Core Name	**Lat.** (^{o})	**Lon.** (^{o})	**Min. Age** (kyr)	**Max. Age** (kyr)	**Sed Rt.** (cm/kyr)	n	α, λ	**variance reduc. (%)**	**Ref**
805b	1.14	160.32	769.8	820.8	2	40	0.28, 1.30	45	52
804c	1.0	161.4	774.0	796.0	1	22	0.28, 1.30	41	52
664d	0.1	-23.27	769.8	806.7	4	73	0.28, 1.30	43	54
v16-58	-46.5	31.3	766.5	789.6	<2	56	0.28, 1.30	10	55,56

Table 3.1: Relative paleointensity records used in PADM2M. (*) denotes Core is excluded from final model; n is number of data used from RPI record; α, λ are the two best fitting APD pdf shape parameters for the residuals distribution. References: 1, Channell et al. (1997); 2, Channell (1999); 3, Channell and Kleiven (2000); 4, Channell et al. (2002); 5, Channell et al. (2004); 6, Leonhardt et al. (1999); 7, Guyodo et al. (1999); 8, Hayashida et al. (1999); 9,Horng et al. (2003); 10, Yamazaki and Oda (2005); 11, Valet and Meynadier (1993); 12, Meynadier et al. (1994); 13, Nowaczyk and Frederichs (1999); 14, Williams et al. (1998); 15, Thouveny et al. (1994); 16, Thouveny et al. (2004); 17, Yamazaki (1999); 18, Tric et al. (1992); 19, Lehman et al. (1996); 20, Dinares-Turell et al. (2002); 21, Kent and Opdyke (1977); 22, Laj et al. (1996); 23, Schneider (1993); 24, Schneider and Mello (1996); 25, Guyodo and Valet (2006); 26, Schneider et al. (1992); 27, Sato et al. (1998); 28, Kok and Tauxe (1999); 29, Yamazaki et al. (1995); 30, Sato and Kobayashi (1989); 31, Carcaillet et al. (2003); 32, Tauxe and Shackleton (1994); 33, Tauxe and Wu (1990); 34, Valet et al. (1994); 35, Stoner et al. (2003); 36, Guyodo et al. (2001); 37, Kissel et al. (1999); 38, Laj et al. (2000); 39, Oda et al. (2002); 40, Peck et al. (1996); 41, Roberts et al. (1997); 42, Okada (1995); 43, Stoner et al. (2000); 44, Weeks et al. (1995); 45, Schwartz et al. (1996); 46, Haag (2000); 47, Stott et al. (2002); 48, Yamazaki and Ioka (1994); 49, Meynadier et al. (1992); 50, Stoner et al. (2002); 51, Channell et al. (2000); 52, Hartl and Tauxe (1996); 53, Clement and Kent (1986); 54, Valet et al. (1989); 55, Clement and Kent (1991); 56, Kent and Schneider (1995)

Table 3.2 Comparison of Model Statistics

Model	μ_{2M}	σ_{2M}	μ_b	σ_b	μ_m	σ_m
PLS Spline	6.0	1.4	7.2	1.2	5.3	1.0
PADM2Mp	5.3	1.7	6.2	1.5	4.8	1.5
PADM2M	5.3	1.5	6.2	1.2	4.8	1.4
Sint-2000	6.2	2.0	7.6	1.7	5.3	1.6
PISO-1500	-	-	7.5	2.6	-	-

Table 3.2: Mean (μ) and one standard deviation (σ) of the four axial dipole models discussed in text and the Penalized Least Squares fit (PLS Spline) to absolute paleointensities used in the construction of PADM2M over three age ranges. Subscripts 2M, b, and m represent age ranges of: 0-2 Ma, 0-780 ka (the Brunhes chron) and 780 ka - 2 Ma respectively.

References

Amit, H., and Olson, P., 2006: Time-average and time-dependent parts of core flow. *Phys. Earth Planet. Int.*, **155**(1-2), 120–139. doi:10.1016/j.pepi.2005.10.006.

Ben-Yosef, E., Tauxe, L., Levy, T. E., Shaar, R., Ron, H., and Najjar, M., 2009: Geomagnetic intensity spike recorded in high resolution slag deposit in Southern Jordan. *Earth Planet. Sci. Lett.*, **287**(3-4), 529–539.

Biggin, A., Strik, G., and Langereis, C., 2009: The intensity of the geomagnetic field in the late-Archaean: new measurements and an analysis of the updated IAGA palaeointensity database. *Earth Planets and Space*, **61**(1), 9–22.

Bloxham, J., and Jackson, A., 1992: Time-Dependent Mapping of the Magnetic-field at the Core-Mantle Boundary. *J. Geophys. Res.- Solid Earth*, **97**(B13), 19537–19563.

Brachfeld, S., Domack, E., Kissel, C., Laj, C., Leventer, A., Ishman, S., Gilbert, R., Camerlenghi, A., and Eglinton, L., 2003: Holocene history of the Larsen-A Ice Shelf constrained by geomagnetic paleointensity dating. *Geology*, **31**(9), 749–752.

Cande, S., and Kent, D., 1995: Revised calibration of the geomagnetic polarity timescale for the late Cretaceous and Cenozoic. *J. Geophys. Res.*, **100**(B4), 6093–6095.

Carcaillet, J. T., Thouveny, N., and Bourles, D. L., 2003: Geomagnetic moment instability between 0.6 and 1.3 ma from cosmonuclide evidence. *Geophys. Res. Lett.*, **30**(15), 1792.

Channell, J., Stoner, J., Hodell, D., and Charles, C., 2000: Geomagnetic paleointensity for the last 100 kyr from the sub-antarctic South Atlantic: a tool for inter-hemispheric correlation. *Earth Planet. Sci. Lett.*, **175**, 145–160.

Channell, J. E. T., 1999: Geomagnetic paleointensity and directional secular variation at Ocean Drilling Program (ODP) Site 984 (Bjorn Drift) since 500 ka: Comparisons with ODP Site 983 (Gardar Drift). *J. Geophys. Res.*, **104**(B10), 22937–22951.

Channell, J. E. T., Curtis, J. H., and Flower, B. P., 2004: The Matuyama-Brunhes boundary interval (500-900 ka) in North Atlantic drift sediments. *Geophys. J. Int.*, **158**(2), 489–505.

Channell, J. E. T., Hodell, D. A., and Lehman, B., 1997: Relative geomagnetic paleointensity and ^{18}O at ODP Site 983 (Gardar Drift, North Atlantic) since 350 ka. *Earth Planet. Sci. Lett.*, **153**, 103–118.

Channell, J. E. T., Hodell, D. A., McManus, J., and Lehman, B., 1998: Orbital modulation of the Earth's magnetic field intensity. *Nature*, **394**(6692), 464–468.

Channell, J. E. T., and Kleiven, H. F., 2000: Geomagnetic palaeointensities and astrochronological ages for the Matuyama-Brunhes boundary and the boundaries of the Jaramillo Subchron: palaeomagnetic and oxygen isotope records from ODP Site 983. *Phil Trans Roy Soc London, Series A*, **358**(1768), 1027–1047.

Channell, J. E. T., Mazaud, A., Sullivan, P., Turner, S., and Raymo, M. E., 2002: Geomagnetic excursions and paleointensities in the Matuyama Chron at Ocean Drilling Program Sites 983 and 984 (Iceland Basin). *J. Geophys. Res.*, **107**(B6).

Channell, J. E. T., Xuan, C., and Hodell, D. A., 2009: Stacking paleointensity and oxygen isotope data for the last 1.5 Myr (PISO-1500). *Earth Planet. Sci. Lett.*, **283**(1-4), 14–23. doi:10.1016/j.epsl.2009.03.012.

Clement, B., and Kent, D., 1991: A Southern-Hemisphere Record of the Matuyama-Brunhes Polarity Reversal. *Geophy. Research Letters*, **18**(1), 81–84.

Clement, B. M., and Kent, D. V., 1986: Short polarity intervals within the Matuyama: transitional field records from hydraulic piston cored sediments from the North Atlantic. *Earth Planet. Sci. Lett.*, **81**, 253–264.

Constable, C., 1988: Parameter-estimation in non-gaussian noise. *Geophys. J.*, **94**(1), 131–142.

Constable, C., and Johnson, C., 2005: A paleomagnetic power spectrum. *Phys. Earth Planet. Int.*, **153**(1-3, Sp. Iss. SI), 61–73. doi:10.1016/j.pepi.2005.03.015.

Constable, C., and Parker, R., 1988: Smoothing, splines, and smoothing splines - their application in geomagnetism. *J. Computational Physics*, **78**(2), 493–508.

Constable, C., and Parker, R., 1991: Deconvolution of long-core paleomagnetic measurements - spline therapy for the linear problem. *Geophys. J. Int.*, **104**(3), 453–468.

Dinares-Turell, J., Sagnotti, L., and Roberts, A. P., 2002: Relative geomagnetic paleointensity from the Jaramillo Subchron to the Matuyama/Brunhes boundary as recorded in a Mediterranean piston core. *Earth Planet. Sci. Lett.*, **194**(3-4), 327–341.

Donadini, F., Korte, M., and Constable, C. G., 2009: Geomagnetic field for 0-3 ka: 1. New data sets for global modeling. *Geochem. Geophys. Geosyst.*, **10**, Q06007, 10.1029/2008GC002295. doi:10.1029/2008GC002295.

Driscoll, P., and Olson, P., 2009: Polarity reversals in geodynamo models with core evolution. *Earth Planet. Sci. Lett.*, **282**(1-4), 24–33. doi: 10.1016/j.epsl.2009.02.017.

Dumberry, M., and Finlay, C., 2007: Eastward and westward drift of the Earth's magnetic field for the last three millennia. *Earth Planet. Sci. Lett.*, **254**(1-2), 146–157. doi:10.1016/j.epsl.2006.11.026.

Guyodo, Y., Acton, G. D., Brachfeld, S., and Channell, J. E. T., 2001: A sedimentary paleomagnetic record of the Matuyama chron from the Western Antarctic margin (ODP Site 1101). *Earth Planet. Sci. Lett.*, **191**(1-2), 61–74.

Guyodo, Y., Richter, C., and Valet, J. P., 1999: Paleointensity record from Pleistocene sediments off the California Margin. *J. Geophys.*, **104**, 22953–22965.

Guyodo, Y., and Valet, J. P., 2006: A comparison of relative paleointensity records of the Matuyama Chron for the period 0.75-1.25 Ma. *Phys. Earth Planet. Int.*, **156**, 205–212.

Haag, M., 2000: Reliability of relative palaeointensities of a sediment core with climatically-triggered strong magnetisation changes. *Earth Planet. Sci. Lett.*, **180**(1-2), 49–59.

Hartl, P., and Tauxe, L., 1996: A precursor to the Matuyama/Brunhes transition-field instability as recorded in pelagic sediments. *Earth Planet. Sci. Lett.*, **138**, 121–135.

Hayashida, A., Verosub, K. L., Heider, F., and Leonhardt, R., 1999: Magnetostratigraphy and relative palaeointensity of late Neogene sediments at ODP Leg 167 Site 1010 off Baja California. *Geophys. J. Int.*, **139**(3), 829–840.

Horng, C. S., Roberts, A. P., and Liang, W. T., 2003: A 2.14-Myr astronomically tuned record of relative geomagnetic paleointensity from the western Philippine Sea. *J. Geophys. Res.*, **108**(B1).

Jackson, A., Jonkers, A., and Walker, M., 2000: Four centuries of geomagnetic secular variation from historical records. *Phil. Trans. Roy. Soc. Lond.*, **358**(1768), 957–990.

Johnson, C., and McFadden, P., 2007: Time-averaged field and paleosecular variation. In *Geomagnetism*, editor M. Kono and G. Schubert, volume 5 of *Treatise on Geophysics*, 417–453. Elsevier, Amsterdam.

Johnson, C. L., Constable, C. G., Tauxe, L., Barendregt, R., Brown, L. L., Coe, R. S., Layer, P., Mejia, V., Opdyke, N. D., Singer, B. S., Staudigel, H., and Stone, D. B., 2008: Recent investigations of the 0-5 Ma geomagnetic field recorded by lava flows. *Geochem. Geophys. Geosyst.*, **9**, Q04032, 10.1029/2007GC001696. doi:10.1029/2007GC001696.

Kent, D. V., and Opdyke, N. D., 1977: Paleomagnetic field intensity variation recorded in a Brunhes epoch deep-sea sediment core. *Nature*, **266**, 156–159.

Kent, D. V., and Schneider, D. A., 1995: Correlation of paleointensity variation records in the Brunhes/Matuyama polarity transition interval. *Earth Planet. Sci. Lett.*, **129**, 135–144.

Kissel, C., Laj, C., Labeyrie, L., Dokken, T., Voelker, A., and Blamart, D., 1999: Rapid climatic variations during marine isotopic stage 3: magnetic analysis of sediments from Nordic Seas and North Atlantic. *Earth Planet. Sci. Lett.*, **171**(3), 489–502.

Kok, Y. S., and Tauxe, L., 1999: A relative geomagnetic paleointensity stack from Ontong-Java Plateau sediments for the Matuyama. *J. Geophys. Res.-Solid Earth*, **104**(B11), 25401–25413.

Komunjer, I., 2007: Asymmetric power distribution: Theory and applications to risk measurement. *J. Applied Econometrics*, **22**(5), 891–921. doi: 10.1002/jae.961.

Korte, M., and Constable, C. G., 2005: Continuous geomagnetic field models for the past 7 millenia ii: Cals7k. *Geochem. Geophys. Geosyst.*, **6(2)**, Q02H16, doi:10.1029/2004GC000801.

Korte, M., Donadini, F., and Constable, C. G., 2009: Geomagnetic field for 0-3 ka: 2. A new series of time-varying global models. *Geochem. Geophys. Geosyst.*, **10**, Q06008, 10.1029/2008GC002297. doi:10.1029/2008GC002297.

Laj, C., Kissel, C., and Lefevre, I., 1996: Relative geomagnetic field intensity and reversals from Upper Miocene sections in Crete. *Earth Planet. Sci. Lett.*, **141**(1-4), 67–78.

Laj, C., Kissel, C., Mazaud, A., Channell, J. E. T., and Beer, J., 2000: North Atlantic palaeointensity stack since 75 ka (NAPIS-75) and the duration of the Laschamp event. *Phil. Trans. Roy. Soc. Lond.*, **358**(1768), 1009–1025.

Lawrence, K. P., Tauxe, L., Staudigel, H., Constable, C. G., Koppers, A., McIntosh, W., and Johnson, C. L., 2009: Paleomagnetic field properties at high southern latitude. *Geochem. Geophys. Geosyst.*, **10**, Q01005, 10.1029/2008GC002072. doi:10.1029/2008GC002072.

Lehman, B., Laj, C., Kissel, C., Mazaud, A., Paterne, M., and Labeyrie, L., 1996: Relative changes of the geomagnetic field intensity during the last 280 kyr from piston cores in the Acores area. *Phys. Earth Planet. Inter.*, **93**, 269–284.

Leonhardt, R., Heider, F., and Hayashida, A., 1999: Relative geomagnetic field intensity across the Jaramillo subchron in sediments from the California margin: ODP Leg 167. *J. Geophys. Res*, **104**, 29133–29146.

Lisiecki, L., and Lisiecki, P., 2002: Application of dynamic programming to the correlation of paleoclimate records. *Paleoceanography*, **17**(4), 1049, doi:10.1029/2001PA000733. doi:10.1029/2001PA000733.

Love, J., and Constable, C., 2003: Gaussian statistics for palaeomagnetic vectors. *Geophys. J. Int.*, **152**(3), 515–565.

Maus, S., Macmillan, S., Chernova, T., Choi, S., Dater, D., Golovkov, V., Lesur, F., Lowes, H., Lühr, H., Mai, W., McLean, S., Olsen, N., Rother, M., Sabaka, T., Thomson, A., Zvereva, T., and IAGA Division V, W. G. V., 2005: The 10th generation international geomagnetic reference field. *Phys. Earth Planet. Int.*, **151**, 320–322.

McFadden, P., and McElhinny, M., 1982: Variations in the geomagnetic dipole-2: Statistical analysis of VDMs for the past 5 million years. *Journal of Geomag. and Geoelectricity*, **34**(3), 163–189.

McFadden, P., and Merrill, R., 1997: Sawtooth paleointensity and reversals of the geomagnetic field. *Phys. Earth Planet. Int.*, **103**(3-4), 247–252.

McMillan, D., Constable, C., and Parker, R., 2002: Limitations on stratigraphic analyses due to incomplete age control and their relevance to sedimentary paleomagnetism. *Earth Planet. Sci. Lett.*, **201**(3-4), 509–523.

Meynadier, L., Valet, J. P., Bassinot, F., Shackleton, N. J., and Guyodo, Y., 1994: Asymmetrical saw-tooth pattern of the geomagnetic field intensity from equatorial sediments in the Pacific and Indian Oceans. *Earth Planet. Sci. Lett.*, **126**, 109–127.

Meynadier, L., Valet, J. P., Weeks, R., Shackleton, N. J., and Hagee, V. L., 1992: Relative geomagnetic intensity of the field during the last 140 ka. *Earth Planet. Sci. Lett.*, **114**, 39–57.

Nowaczyk, N. R., and Frederichs, T. W., 1999: Geomagnetic events and relative palaeointensity variations during the past 300 ka as recorded in Kolbeinsey Ridge sediments, Iceland Sea: indication for a strongly variable geomagnetic field. *Int. J. Earth Sci.*, **88**(1), 116–131.

Oda, H., Nakamura, K., Ikehara, K., Nakano, T., Nishimura, M., and Khlystov, O., 2002: Paleomagnetic record from Academician Ridge, Lake Baikal: a reversal excursion at the base of marine oxygen isotope stage 6. *Earth Planet. Sci. Lett.*, **202**(1), 117–132.

Okada, M., 1995: Detailed variation of geomagnetic field intensity during the late Pleistocene at Site 882. *Proc. ODP, Sci. Res.*, **145**, 469–474.

Parker, R. L., 1994: *Geophysical Inverse Theory.* Princeton University Press.

Peck, J., King, J., Colman, S., and Kravchinsky, V., 1996: An 84-kyr paleomagnetic record from the sediments of Lake Baikal, Siberia. *J. Geophys. Res.*, **101**, 1,365–11,385.

Press, W. H., Teukolsky, S. A., Vetterling, W. T., and Flannery, B. P., 1986: *Numerical Recipes in Fortran 77: the Art of Scientific Computing.* Cambridge University Press.

Rice, J. A., 1995: *Mathematical Statistics and Data Analysis, second edition.* Duxbury Press.

Roberts, A., Lehman, B., Weeks, R., Verosub, K., and Laj, C., 1997: Relative paleointensity of the geomagnetic field over the last 200,000 years from ODP Sites 883 and 884, North Pacific Ocean. *Earth Planet. Sci. Lett.*, **152**, 11–23.

Roberts, A. P., and Winklhofer, M., 2004: Why are geomagnetic excursions not always recorded in sediments? Constraints from post-depositional remanent magnetization lock-in modelling. *Earth Planet. Sci. Lett.*, **227**(3-4), 345–359.

Rowan, C. J., Roberts, A. P., and Broadbent, T., 2009: Reductive diagenesis, magnetite dissolution, greigite growth and paleomagnetic smoothing in marine sediments: A new view. *Earth Planet. Sci. Lett.*, **277**(1-2), 223–235.

Sato, T., Kikuchi, H., Nakashizuka, M., and Okada, M., 1998: Quaternary geomagnetic field intensity: Constant periodicity or variable period? *Geophys. Res. Lett*, **25**, 2221–2224.

Sato, T., and Kobayashi, K., 1989: Long-period secular variations of the Earth's magnetic field revealed by Pacific deep-sea sediment cores. *J. Geomag. Geoelectr.*, **41**, 147–159.

Schneider, D., and Mello, G., 1996: A high-resolution marine sedimentary record of geomagnetic iintensity during the Brunhes chron. *Earth Planet. Sci. Lett.*, **144**, 297–314.

Schneider, D. A., 1993: An estimate of Late Pleistocene geomagnetic intensity variation From Sulu Sea sediments. *Earth Planet. Sci. Lett.*, **120**(3-4), 301–310.

Schneider, D. A., Kent, D. V., and Mello, G. A., 1992: A detailed chronology of the Australasian impact event, the Brunhes-Matuyama geomagnetic polarity reversal and global climate change. *Earth Planet. Sci. Lett.*, **111**, 395–405.

Schwartz, M., Lund, S. P., and Johnson, T. C., 1996: Environmental factors as complicating influences in the recovery of quantitative geomagnetic-field paleointensity estimates from sediments. *Geophys. Res. Lett.*, **23**, 2693–2696.

Singer, B. S., Hoffman, K. A., Schnepp, E., and Guillou, H., 2008: Multiple Brunhes Chron excursions recorded in the West Eifel (Germany) volcanics: Support for long-held mantle control over the non-axial dipole field. *Phys. Earth Planet. Int.*, **169**(1-4, Sp. Iss. SI), 28–40. doi:10.1016/j.pepi.2008.05.001.

Stoner, J., Channell, J., and Hillaire-Marcel, C., 1998: A 200 ka geomagnetic chronostratigraphy for the Labrador Sea: Indirect correlation of the sediment record to SPECMAP. *Earth Planet. Sci. Lett.*, **159**(3-4), 165–181.

Stoner, J., Channell, J., Hillaire-Marcel, C., and Kissel, C., 2000: Geomagnetic paleointensity and environmental record from labrador sea core md95-2024: global marine sediment and ice core chronostratigraphy for the last 110 kyr. *Earth Planet. Sci. Lett.*, **5626**, 1–17.

Stoner, J. S., Channell, J. E. T., Hodell, D. A., and Charles, C. D., 2003: A ∼580 kyr paleomagnetic record from the sub-Antarctic South Atlantic (Ocean Drilling Program Site 1089). *Jour. Geophys. Res.*, **108**(B5).

Stoner, J. S., Laj, C., Channell, J. E. T., and Kissel, C., 2002: South Atlantic and North Atlantic geomagnetic paleointensity stacks (0-80 ka): implications for inter-hemispheric correlation. *Quaternary Science Reviews*, **21**(10), 1141–1151.

Stott, L., Poulsen, C., Lund, S., and Thunell, R., 2002: Super ENSO and global climate oscillations at millennial time scales. *Science*, **297**, 222–226.

Tauxe, L., and Shackleton, N. J., 1994: Relative paleointensity records from the Ontong-java Plateau. *Geophys. J. Int.*, **117**, 769–782.

Tauxe, L., and Wu, G., 1990: Normalized remanence in sediments of the Western Equatorial Pacific: relative paleointensity of the geomagnetic field? *J. Geophys. Res.*, **95**(B8), 12,337–12,350.

Tauxe, L., and Yamazaki, T., 2007: Paleointensities. In *Geomagnetism*, editor M. Kono and G. Schubert, volume 5 of *Treatise on Geophysics*, 509–563. Elsevier, Amsterdam.

Thellier, E., and Thellier, O., 1959: Sur l'intensité du champ magnétique terrestre dans le passé historique et géologique. *Annales de Geophysique*, **15**, 258–378.

Thouveny, N., Carcaillet, J., Moreno, E., Leduc, G., and Nerini, D., 2004: Geomagnetic moment variation and paleomagnetic excursions since 400 kyr BP: a stacked record from sedimentary sequences of the Portuguese margin, Pt 1. *Earth Planet. Sci. Lett.*, **219**(3-4), 377–396.

Thouveny, N., Debeaulieu, J. L., Bonifay, E., Creer, K. M., Guiot, J., Icole, M., Johnsen, S., Jouzel, J., Reille, M., Williams, T., and Williamson, D., 1994: Climate Variations in Europe over the Past 140-Kyr Deduced from Rock Magnetism. *Nature*, **371**(6497), 503–506.

Tric, E., Valet, J. P., Tucholka, P., Paterne, M., LaBeyrie, L., Guichard, F., Tauxe, L., and Fontugne, M., 1992: Paleointensity of the geomagnetic field during the last 80,000 years. *J. Geophys. Res.*, **97**, 9337–9351.

Valet, J., 2003: Time variations in geomagnetic intensity. *Reviews of Geophysics*, **41**(1). doi:10.1029/2001RG000104.

Valet, J. P., and Meynadier, L., 1993: Geomagnetic-field intensity and reversals during the past 4 million years. *Nature*, **366**(6452), 234–238.

Valet, J. P., Meynadier, L., Bassinot, F. C., and Garnier, F., 1994: Relative paleointensity across the last geomagnetic reversal from sediments of the Atlantic, Indian and Pacific Oceans. *Geophys. Res. Lett*, **21**, 485–488.

Valet, J. P., Meynadier, L., and Guyodo, Y., 2005: Geomagnetic dipole strength and reversal rate over the past two million years. *Nature*, **435**(7043), 802–805. doi:10.1038/nature03674.

Valet, J. P., Tauxe, L., and Clement, B. M., 1989: Equatorial and mid-latitude records of the last geomagnetic reversal from the Atlantic Ocean. *Earth Planet. Sci. Lett.*, **94**, 371–384.

Wardinski, I., and Korte, M., 2008: The evolution of the core-surface flow over the last seven thousands years. *J. Geophys. Res.- Solid Earth*, **113**(B5). doi: 10.1029/2007JB005024.

Weeks, R. J., Laj, C., Endignoux, L., Mazaud, A., Labeyrie, L., Roberts, A. P., Kissel, C., and Blanchard, E., 1995: Normalised natural remanent magnetisation intensity during the last 240000 years in piston cores from the central North Atlantic Ocean: geomagnetic field intensity or environmental signal? *Phys. Earth Planet. Inter.*, **87**, 213–229.

Williams, T., Thouveny, N., and Creer, K. M., 1998: A normalised intensity record from Lac du Bouchet: geomagnetic palaeointensity for the last 300 kyr? *Earth Planet. Sci. Lett.*, **156**(1-2), 33–46.

Wilson, R., 1970: Permanent aspects of the Earth's non-dipole magnetic field over upper Tertiary times. *Geophys. Journal of the Royal Astronomical Society*, **19**(4), 417–439.

Yamazaki, T., 1999: Relative paleointensity of the geomagnetic field during Brunhes Chron recorded in North Pacific deep-sea sediment cores: orbital influence? *Earth Planet. Sci. Lett.*, **169**(1-2), 23–35.

Yamazaki, T., and Ioka, N., 1994: Long-term secular variation of the geomagnetic field during the last 200 kyr recorded in sediment cores from the western equatorial Pacific. *Earth Planet. Sci. Lett.*, **128**, 527–544.

Yamazaki, T., Ioka, N., and Eguchi, N., 1995: Relative paleointensity of the geomagnetic field during the Brunhes Chron. *Earth Planet. Sci. Lett.*, **136**, 525–540.

Yamazaki, T., and Kanamatsu, T., 2007: A relative paleointensity record of the geomagnetic field since 1.6 Ma from the North Pacific. *Earth Planets and Space*, **59**(7), 785–794.

Yamazaki, T., and Oda, H., 2005: A geomagnetic paleointensity stack between 0.8 and 3.0 Ma from equatorial Pacific sediment cores. *Geochem. Geophys. Geosyst.*, **6**, Q11H20, doi: 10.2029/2005GC001001.

Ziegler, L. B., Constable, C. G., and Johnson, C. L., 2008: Testing the robustness and limitations of 0-1 Ma absolute paleointensity data. *Phys. Earth Planet. Int.*, **170**(1-2), 34–45. doi:10.1016/j.pepi.2008.07.027.

Chapter 4

Asymmetry in growth and decay of the geomagnetic dipole

Abstract

The geodynamo in Earth's core is responsible for magnetic field changes on diverse timescales, including numerous enigmatic reversals of the dipole field polarity. Understanding the physical processes driving them is an active area of investigation via both paleomagnetic work and numerical simulations of the geodynamo. Some previous studies on geomagnetic field intensity detected a *sawtooth pattern* of intensity around reversals: a gradual decay in field strength preceding a reversal followed by rapid growth afterwards. Here we characterize distinct statistical properties for increasing and decreasing dipole strength over the past two million years. Examining the geomagnetic field and its time derivative on a range of time scales reveals that for periods longer than about 25 ky there is a clear asymmetry in the statistical distributions for growth versus decay rates of the dipole strength. At 36 ky period, average growth rate is about 20% larger than the decay rate, and the field spends 54% of its time decaying, but only 46% growing. These differences are not limited to times when the field is reversing, suggesting that the asymmetry is controlled by fundamental physical processes underlying all paleosecular variation. The longer decay cycle might suggest the possibility of

episodic periods of subcritical dynamo activity where the field is dominated by diffusive processes, followed by transient episodes of strong convection. However, our work finds no clear separation of timescales for diffusive and convective processes influence on dipole moment: both seem to play an important but asymmetric role on the 25-150 ky timescale.

4.1 Introduction

Relative paleointensity variation records from marine sediments have contributed enormously to current views of how the geomagnetic field changes on time scales of thousands to millions of years. A 4 My long sediment record of relative paleointensity Valet and Meynadier (1993), first provided the idea of a sawtooth pattern, namely that field intensity is highest immediately after a polarity reversal, slowly decays until the next reversal occurs, and rebounds to a high after the reversal thus beginning a new cycle. The slow decay might be interpreted as a steady diffusive process (with faster advective influences overlaid) but the characteristic time scale of several hundred thousand years is long compared with the dipole free decay time of 15 ky (Backus et al., 1996). The sawtooth interpretation was immediately debated (Kok and Tauxe, 1996) and, despite being subsequently observed in some relative paleointensity records, has not been universally seen or accepted (see Tauxe and Yamazaki (2007); Valet (2003) for reviews). A pared down version of this observation has subsequently been uncovered in the Sint-2000 stack of about 30 sediment records Valet et al. (2005), in which field intensity takes tens of thousands of years to decay preceding 5 of the 7 reversals between 780 and 2000 ka, and only a few thousand years to grow back to values more typical of stable polarity intervals. It was suggested that diffusive processes dominate the pre-reversal episode.

We take a new approach to testing this observation, and examine the statistical distributions of time derivatives of the comprehensive PADM2M model

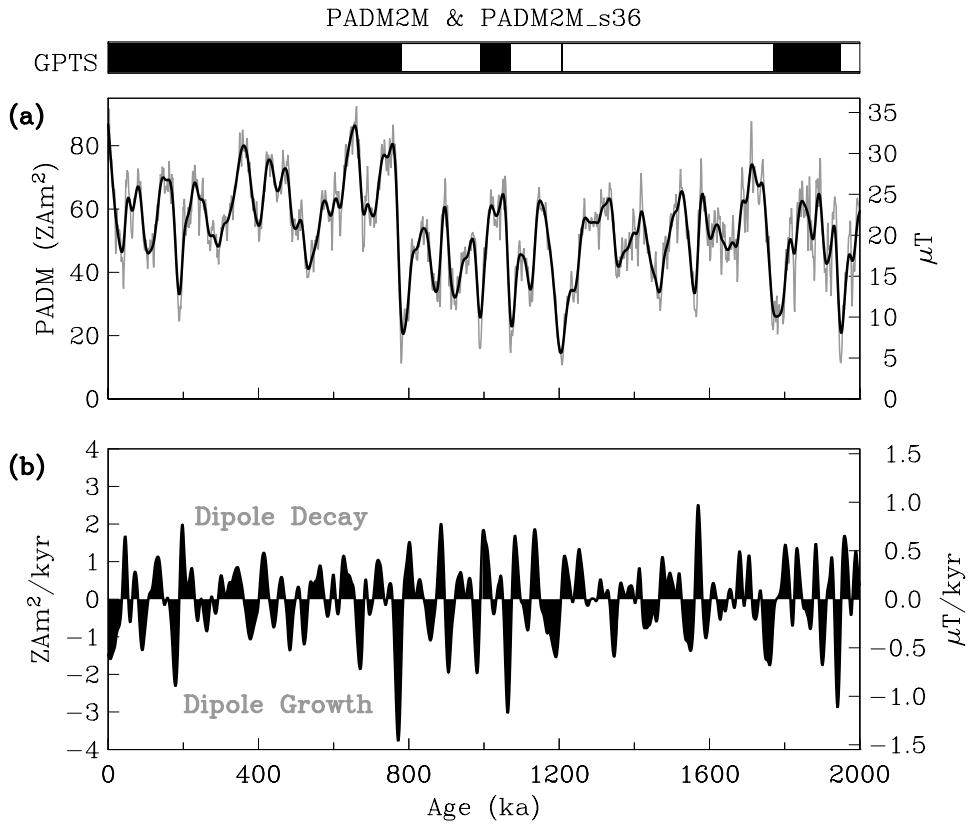

Figure 4.1: Axial dipole moment variations and rate of change for the time period 0-2000 ka: (a) PADM2M (gray)(Ziegler et al., 2011) and PADM2M_s36 (black), smoothed to damp variations with periods shorter than 36 ky. Left axis gives axial dipole moment, p_A in units of $10^{21} Am^2$. Right axis give equivalent value in μT for g_1^0 the axial dipole coefficient in spherical harmonic representation of the field, $p_A(t) = \frac{4\pi r^3}{\mu_0} g_1^0(t) = 2.58621 g_1^0(t)\ ZAm^2$ (b) Rate of change for PADM2M_s36, showing stronger average dipole growth than decay.

of dipole strength at various frequency resolutions.

4.2 Methods

PADM2M (Ziegler et al., 2011) was constructed using a penalized maximum likelihood inversion technique that efficiently uses 5000 globally-distributed individual absolute paleointensity data and 76 sedimentary relative paleointensity records with variable lengths and sedimentation rates to produce a calibrated, continuous, time-varying model of Paleomagnetic Axial Dipole Moment (PADM).

Time variations in PADM2M are parametrized by cubic B-splines allowing a direct calculation of the rate of change with time. The model is expected to robustly resolve features at timescales longer than 10 ky.

We fit a family of smoothing splines (Constable and Parker, 1988) to the PADM2M model, with each one effectively creating a low-pass filtered version of the original, and calculate uniformly sampled time derivatives. Models have effective cutoff periods ranging from 10 –180 ky, where the cutoff is the period at which the smoothed model power spectrum has been damped to half the power of the original PADM2M. Each is named according to its cutoff period (xx) as PADM2M_sxx.

4.3 Results

4.3.1 Asymmetry in Rate of Change

Figure 4.1a shows PADM2M together with a representative smoothed model, PADM2M_s36, in which variations with periods shorter than 36 ky have been suppressed. A plot of the time-derivative for PADM2M_s36 (Fig. 4.1b) shows that extreme values of the growth rates tend to exceed those of decay rates. To investigate further, we construct a histogram of evenly sampled derivative values, and find a distinct, but subtle, asymmetry that depends on the filter period. For PADM2M_s36 the average growth rate is about 20% larger than the decay rate and peak growth values are approximately 50% larger, suggesting the field has episodes of strong growth with no equivalent in the decay process. Additionally, the field is decreasing a larger fraction of the time (54%), suggesting intervals of decay which are longer than comparable spans of growth. This result is not specific to limited windows surrounding polarity reversals, but applies to the full two million year time span. In Figure 4.2, the Brunhes (0-780 ka) and Matuyama (780-2000 ka) chrons are considered separately, excising 50 ky on each side of the reversal at 780 ka. In both cases, the histograms are asymmetric, with slightly more values

exhibiting dipole decay than growth, and the magnitude of extreme growth rate is larger than for extreme decay. A calculation of separate empirical cumulative distribution functions (ECDFs) for the magnitudes confirms that rates of decrease are concentrated at lower values than for increase.

Notably, the Brunhes chron shows the asymmetry in derivative distribution, but contains no reversals, although there are multiple geomagnetic excursions. Therefore, these differences in growth and decay statistics are not limited to times when the field is reversing, suggesting that the asymmetry reflects fundamental physical processes underlying the paleosecular variation. The robustness of our result is tested by repeating the analysis using other dipole moment reconstructions for the 0-2 Ma time interval. The Sint-2000 stack shows the same asymmetry in both chrons. Another reconstruction, the PISO-1500 stack (Channell et al., 2009) does not, but there are major methodological differences in its reconstruction.

Intensity changes occur on a range of timescales, and their structure depends on the temporal resolution of the curve being studied. Fig. 4.3 shows a sampling of histogram derivatives from several of the PADM2M_sxx models (the full suite is provided in Supplemental Figure 1 (Figure 4.5 at end of chapter). The original, unfiltered PADM2M model resolves changes down to 5-10 ky, and the peak dipole strength attained over the past 2 My appears to be capped around its recent values (Fig. 4.1a). Growth and decay on the timescale of the model resolution (5-10 ky) appear to be well balanced, which could be interpreted as similar processes governing growth and decay on this relatively short timescale. However, as we filter higher frequency field strength variations and look at progressively longer timescales, the pattern of longer duration of decay increasingly stands out. When periods shorter than 10 ky are heavily damped there is an unambiguous asymmetry in the distribution of rates of change, and when variations shorter than 25 ky are damped the fraction of time spent growing is noticeably smaller than that spent decreasing. As expected the magnitudes of rate of change decrease with increasing cutoff period. The structure of the asymmetry also evolves with

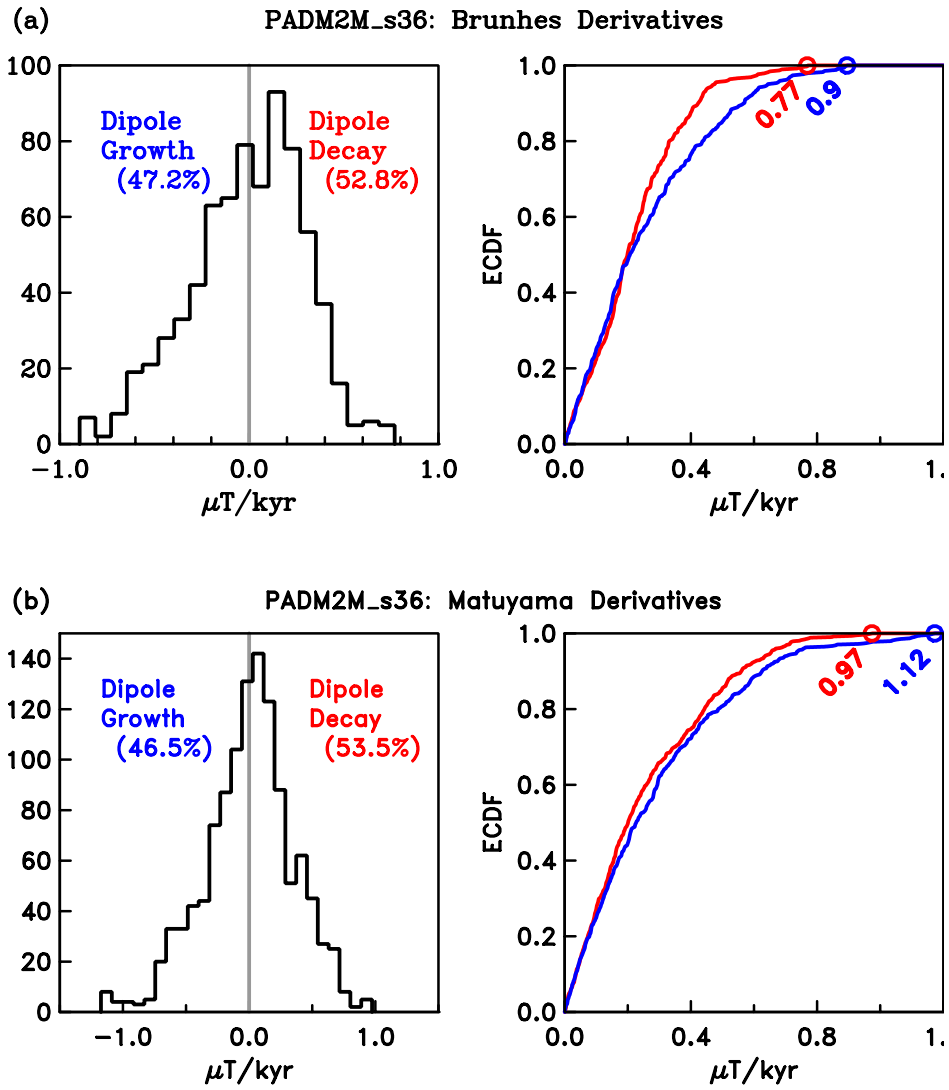

Figure 4.2: Asymmetric distributions of rate of change of axial dipole strength for PADM2M_s36: (a) the evenly sampled Brunhes and (b) Matuyama segments of PADM2M_ s36 show rapid rates of axial dipole growth and slower decay. Note 50 ky segment of time series was removed from each side of Brunhes/Matuyama boundary. Also negative derivative corresponds to growth because age decreases with flow of time. Right panels shows ECDFs for magnitudes of growth (blue) and decay (red), with the values of distribution extrema labeled.

increasing cutoff. Figure 4.4a summarizes this dependence, showing the percentage of time spent growing as a function of cutoff frequency in the PADM2M_sxx family of models. From cutoffs of 40 My^{-1} to 19 My^{-1} (periods of 25 ky to about

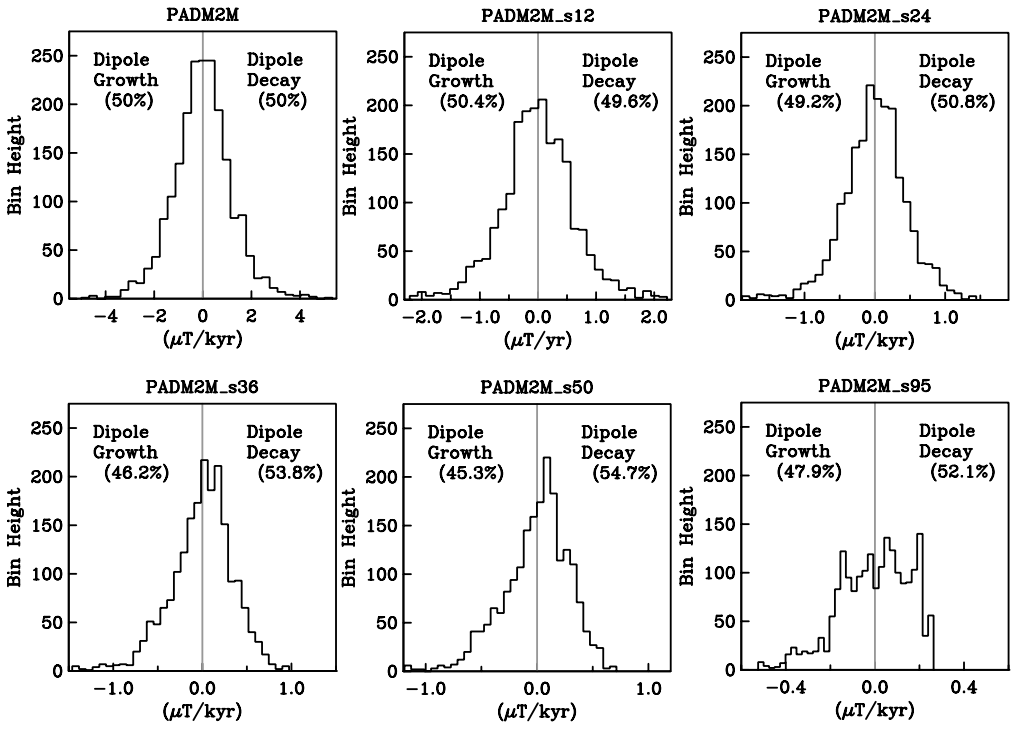

Figure 4.3: Progressively asymmetrical derivates: Six panels show histograms of rates of dipole intensity change for progressively smoother PADM2M_s family models (see Methods). PADM2M is in the top left, and family models are ordered and labeled according to their cutoff period (xx) as PADM2M_sxx. Asymmetry is most pronounced where cutoff period is around 50 kyr.

50 ky respectively) the percentage growth/decay asymmetry becomes increasingly distinct. From 19 My^{-1} to 7 My^{-1}, the asymmetry remains, but becomes less pronounced. This probably reflects the fact that the field today is stronger than in the past, so the overall trend for the past two-million years is one of growth. Extreme damping of the PADM2M_sxx family eventually recovers the signal of long term growth rather than decay in the field, so that when damping variations with periods over 150 ky (frequency of 7 My^{-1}) we see a majority of the time is spent in growing. However, the actual distribution of growth and decay remains asymmetric even at very long periods (Fig. 4.3a).

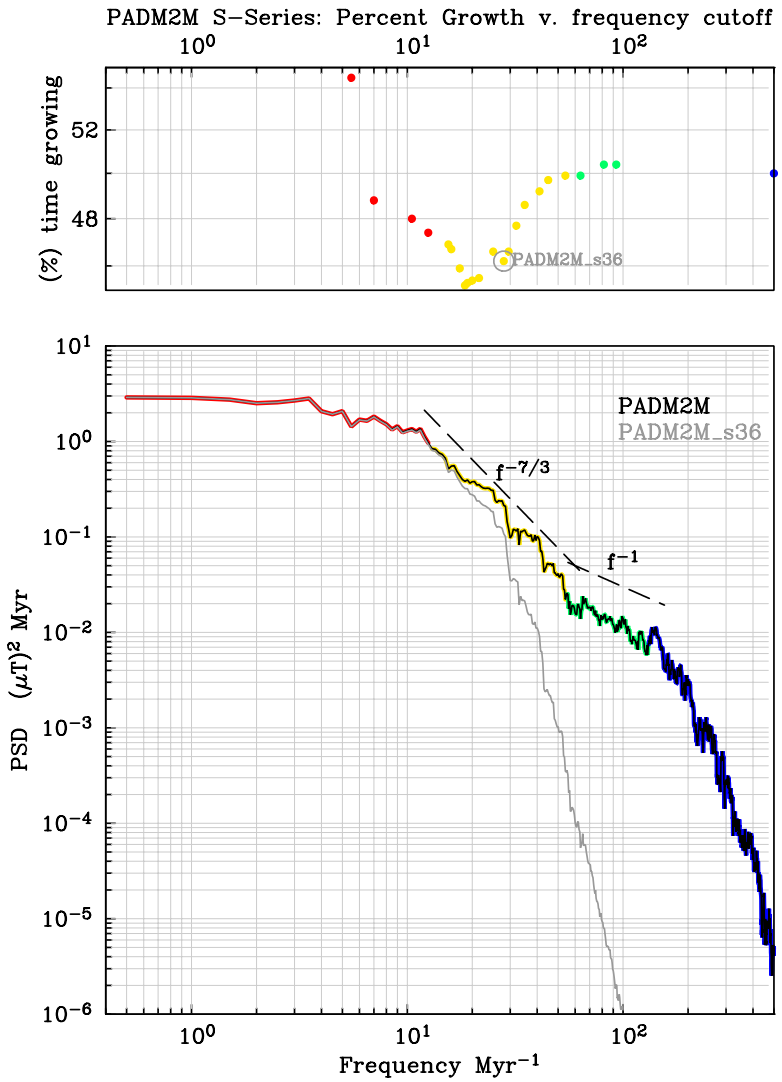

Figure 4.4: Power spectrum for PADM2M and impact of smoothing on asymmetry in growth and decay: (a) Percentage of time spent in periods of intensity growth vs. frequency cutoff of smoothing. Gray circle indicates the value corresponding to the smoothed PADM2M_s36 model analyzed in this study. (b) PADM2M power spectrum (black) highlighted with colors to show distinct behavioral regimes. Spectrum of smoothed PADM2M_s36 is shown in gray. All power spectra are calculated with prolate multi-taper techniques (Thomson, 1982), with time bandwidth product of 12 and frequency resolution of 5.4 My^{-1}.

4.3.2 Ties to Features in the Power Spectrum

Fig. 4.4b shows that this behavior can be tied to several distinct regimes in the power spectrum of PADM2M. From about 1 to 12 My^{-1} the spectrum

is roughly flat, as expected for randomly occurring reversals and excursions in a Poisson-like process with specific average rate (Constable and Johnson, 2005). From about 12 to 60 My^{-1} the power spectrum falloff is about $f^{-7/3}$; then from 60 to 100 My^{-1} the slope is a bit shallower, with a falloff more like f^{-1} My^{-1}. The time scales of roughly 10-100 ky covered by these two regions can be expected to reflect paleosecular variation of the magnetic field, although the transition to f^{-1} might also be impacted by increasing age uncertainties in correlating multiple sediment paleointensity records. Above 100 My^{-1} the falloff is mainly controlled by regularization of the PADM2M model inherent in the inversion, accounting for uncertainty in the various contributing data.

The onset of the pattern of asymmetric growth and decay trend at high frequencies correlates with the change in spectral slope from f^{-1} to $f^{-7/3}My^{-1}$. This supports the idea that distinct processes are dominating the paleosecular variation within the various frequency ranges. The asymmetric growth and decay would be associated with the processes characterized by a $f^{-7/3}$ trend in the power spectrum a power law dependence that has been identified in some numerical simulations (Olson et al., 2009; Driscoll and Olson, 2009). We note that while the Sint-2000 record shows the same asymmetry of growth and decay, it does not seem possible to clearly identify regimes in the power spectrum characterized by different falloff slopes.

4.4 Discussion & Conclusions

The transitions among the various parts of the power spectrum in Fig. 4.4b are gradual and hard to identify with precision, as are any exact power law dependencies, but the asymmetries of Fig. 4.4a and Fig 4.3 are clear. Figures 4.2 and 4.4a are compatible with the idea that between 25 and 150 ky periods decreasing dipole moment is dominated by diffusive processes with slow decay most concentrated at rates less than 0.5 $\mu T(ky)^{-1}$. However, on the same timescales

there is evidence for systematic growth that occurs more rapidly than the decay. Neither growth nor decay occurs in a sustained uninterrupted fashion. Given the apparent inhibition on axial dipole growth to values much larger than those seen in the past few millennia, our analysis provides some support for an intrinsically unstable dynamo (Zhang and Gubbins, 2000), with changes in convection strength driven by changes in magnetic field strength, which may then lead to periods of diffusive decay in the dipole. In some numerical dynamos (Liu and Olson, 2009) mixing flows lead to partial dipole field collapse that is accelerated by radial diffusion and meridional advection, but actual field reversal seems to require a sustained mixing event with magnetic flux opposing the dominant polarity (perhaps initiated by a diffusive process) being advected polewards and contributing to a long term decrease in the dipole (Olson et al., 2009). After reversals field strength may be restored through rapid transient growth, as demonstrated by some equatorially antisymmetric zonal field configurations in kinematic model studies (Livermore and Jackson, 2006, 2004).

Our observations indicate that in the 10– 150 ky period range there is no clean separation of the diffusion and advection timescales, but that changes in the dipole are more likely influenced by the combined influence of both slow diffusive and more rapid regeneration processes. A scenario that might lead to geomagnetic reversal is one where the regeneration process fails to engage for some dynamical situation, leading to dominance of diffusive processes and a low in dipole strength somewhat like what was envisaged in an early demonstration (Backus, 1958) of a successful kinematic dynamo. Yet, lows in dipole strength occur often as part of paleosecular variation, sometimes with excursional paleomagnetic directions, but do not necessarily produce a reversal. Our finding that slow decay also occurs in intervals dominated by excursions now links them more closely than ever to reversals in terms of generation mechanism. It may not be necessary to distinguish the processes that produce ordinary paleosecular variation in the dipole moment from those producing a reversal: the physics and time scales may be the same.

The only distinguishing feature of a reversal would be the dynamics producing persistent or recurring decay of field strength in the absence of an appropriate dynamical configuration to reinvigorate the dipole field.

Understanding the complex dynamo process requires analysis of secular variation on timescales of years to millions of years. Characteristic changes in the dominant global dipole field for the past 2 million years provide important constraints for dynamo simulations, since several reversals and excursions occur over this range of time. We can anticipate new time-varying field models that will incorporate characterization of the spatial scale of regional changes contributing to dipole moment, sharpening the views obtained for the past few centuries and millennia (Jackson et al., 2000; Korte et al., 2009) about the persistence of flux lobes, the influence of the tangent cylinder, and any hemispherical biases on these longer time scales. A move to regional views of field behavior may also illuminate tradeoff between rapid convective growth, and how mixtures of advection and diffusion contribute to the dipole decay process.

4.5 Acknowledgments

This study was supported by National Science Foundation Grant EAR 0809709. CC thanks Christopher Davies and David Gubbins for useful conversations.

Chapter 4, in full, has been submitted for publication to Earth and Planetary Science letters as: L. B. Ziegler and C. G. Constable, Asymmetry in growth and decay of the geomagnetic dipole. The dissertation author was the primary investigator and author of this paper.

4.6 Supplementary Material

This sequence of figures shows histograms of rates of change of paleomagnetic axial dipole moment for PADM2M_s family of models. At the top left of the first page we show derivatives for PADM2M. From left/top to right/bottom the S family models are progressively smoother as power in higher frequency variations is damped. Titles PADM2M_sxx on each subfigure indicate the cutoff period (xx), defined by a reduction by a factor of two at the cutoff and increased damping at higher periods. Negative derivatives indicate growth and positive derivatives represent decay because the time axis is expressed in positive numbers of years before present. PADM2M is fairly symmetric, but the distributions of rates of change become increasingly asymmetric as the cutoff period progresses from 10 ky upwards to about 150 ky. Beyond 150 ky the distribution is increasingly dominated by the long term trend towards higher average field strength in the Brunhes chron. Even the whole time span of 2 My cannot provide a representative average for the axial dipole moment.

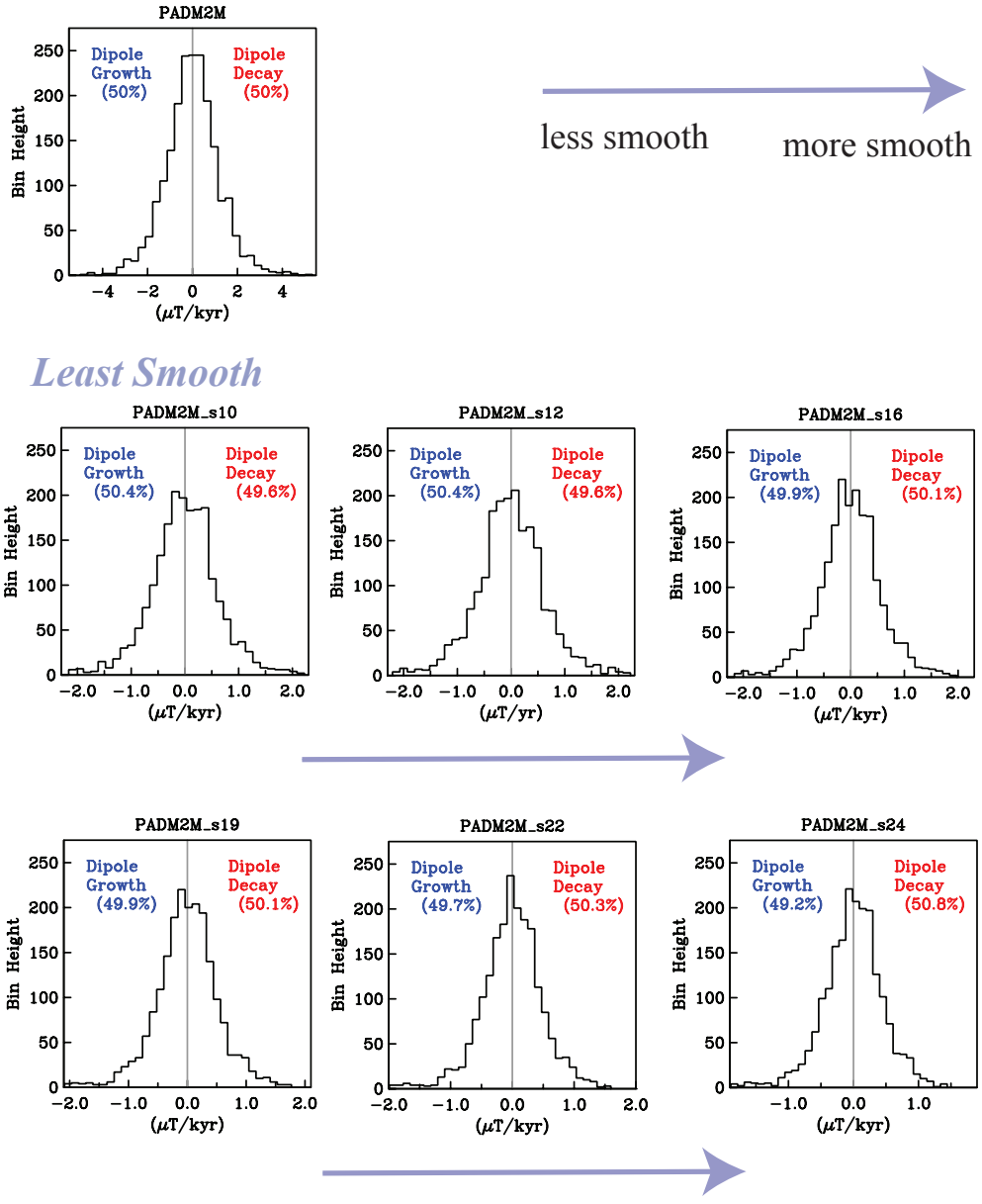

Figure 4.5: Progressively asymmetrical derivates: Full Suite of PADM2M_s models (3 pages)

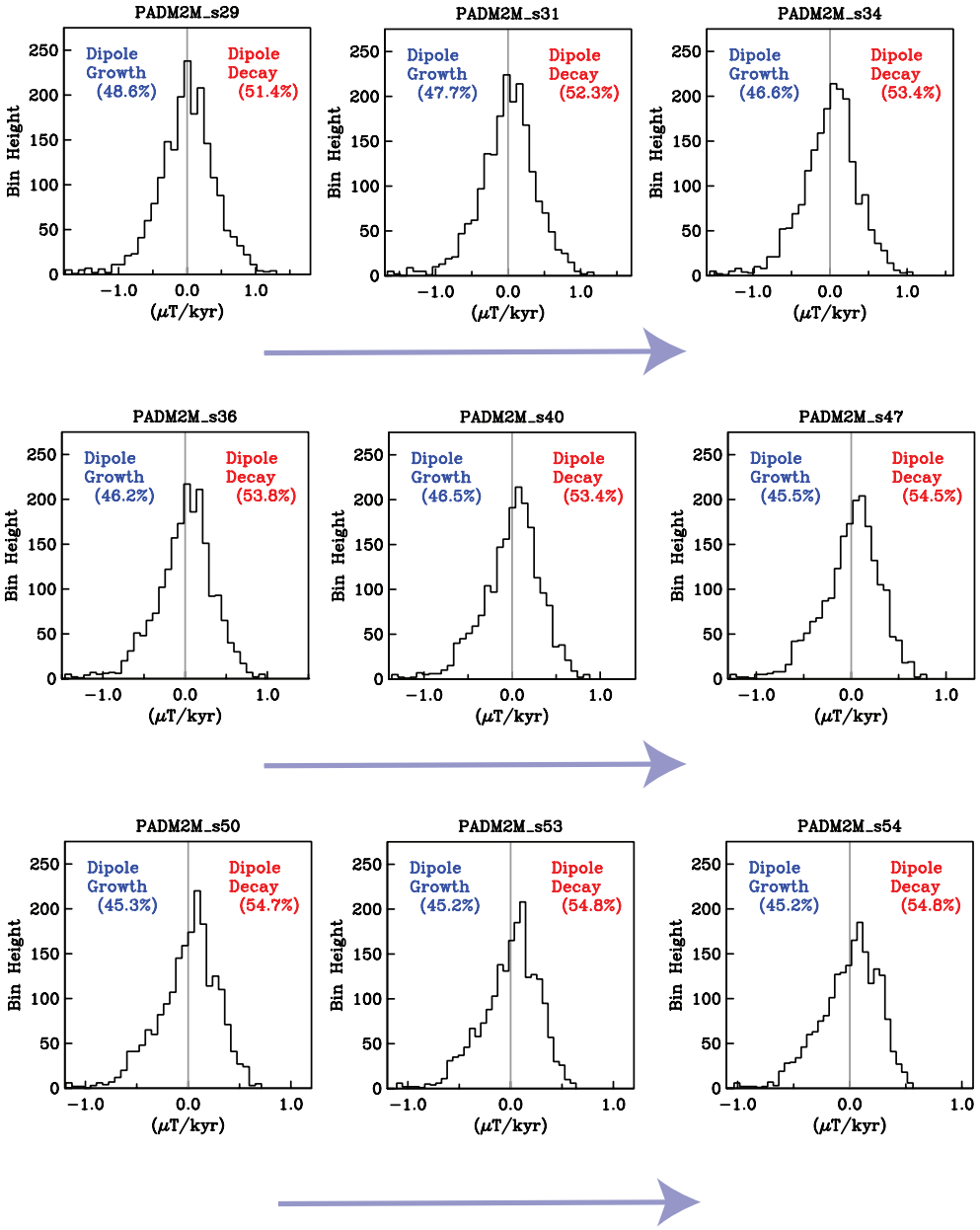

Figure 4.5 continued

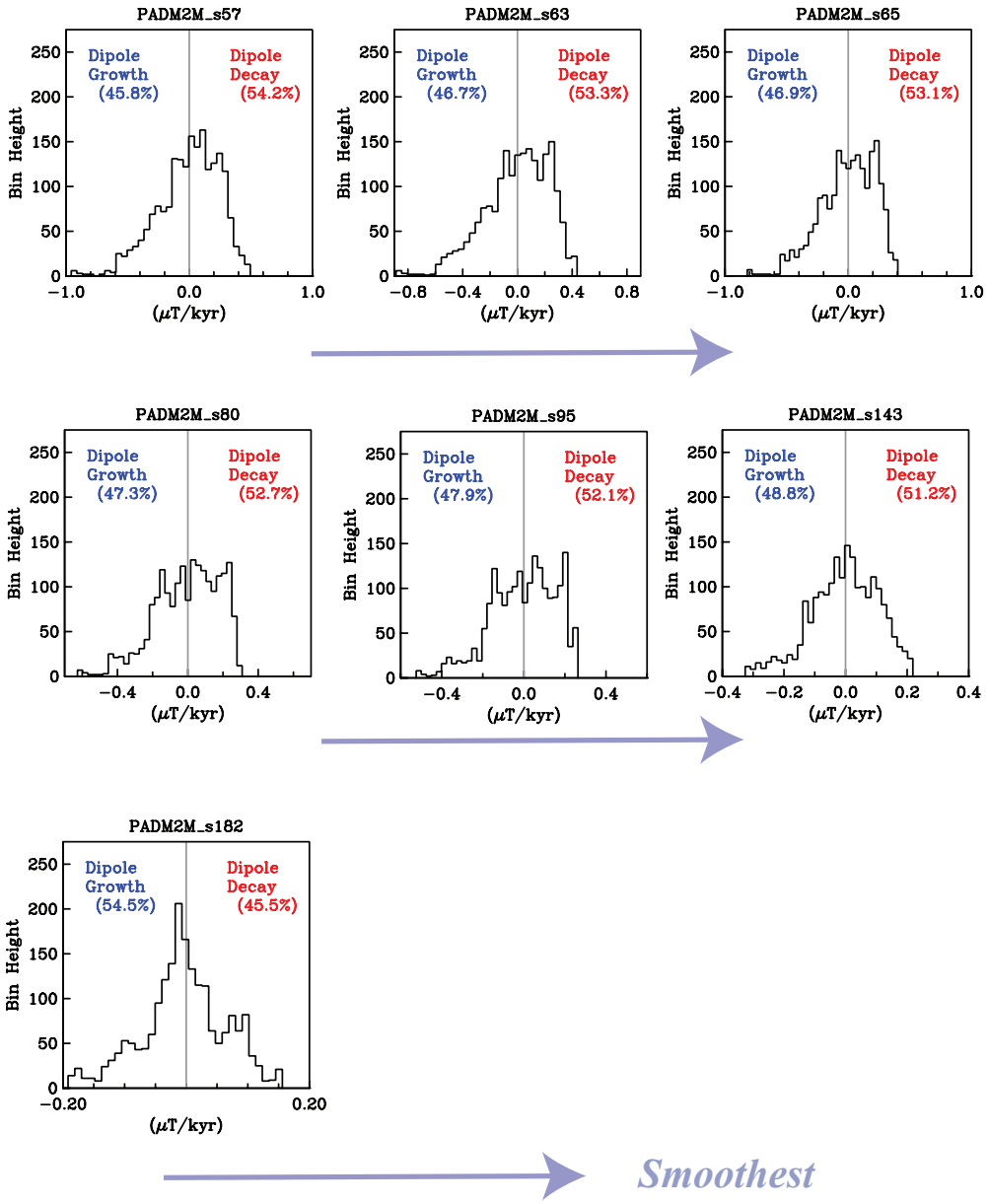

Figure 4.5 continued

References

Backus, G., 1958: A Class of Self-sustaining dissipative spherical dynamos. *Annals of Physics*, **4**(4), 372–447.

Backus, G., Parker, R., and Constable, C., 1996: *Foundations of Geomagnetism.* Cambridge University Press.

Channell, J. E. T., Xuan, C., and Hodell, D. A., 2009: Stacking paleointensity and oxygen isotope data for the last 1.5 Myr (PISO-1500). *Earth Planet. Sci. Lett.*, **283**(1-4), 14–23. doi:10.1016/j.epsl.2009.03.012.

Constable, C., and Johnson, C., 2005: A paleomagnetic power spectrum. *Phys. Earth Planet. Int.*, **153**(1-3, Sp. Iss. SI), 61–73. doi:10.1016/j.pepi.2005.03.015.

Constable, C., and Parker, R., 1988: Smoothing, splines, and smoothing splines - their application in geomagnetism. *J. Computational Physics*, **78**(2), 493–508.

Driscoll, P., and Olson, P., 2009: Polarity reversals in geodynamo models with core evolution. *Earth Planet. Sci. Lett.*, **282**(1-4), 24–33. doi: 10.1016/j.epsl.2009.02.017.

Jackson, A., Jonkers, A., and Walker, M., 2000: Four centuries of geomagnetic secular variation from historical records. *Phil. Trans. Roy. Soc. Lond.*, **358**(1768), 957–990.

Kok, Y., and Tauxe, L., 1996: Saw-toothed pattern of relative paleointensity records and cumulative viscous remanence. *Earth Planet. Sci. Lett.*, **137**(1-4), 95–99.

Korte, M., Donadini, F., and Constable, C. G., 2009: Geomagnetic field for 0-3 ka: 2. A new series of time-varying global models. *Geochem. Geophys. Geosyst.*, **10**, Q06008, 10.1029/2008GC002297. doi:10.1029/2008GC002297.

Liu, L., and Olson, P., 2009: Geomagnetic dipole moment collapse by convective mixing in the core. *Geophy. Research Letters*, **36**. doi:10.1029/2009GL038130.

Livermore, P., and Jackson, A., 2004: Preferential axisymmetric field growth in kinematic geodynamo models. *Geophy. Research Letters*, **31**(22). doi: 10.1029/2004GL021397.

Livermore, P., and Jackson, A., 2006: Transient magnetic energy growth in spherical stationary flows. *Proc. Royal Soc. A*, **462**(2072), 2457–2479. doi: 10.1098/rspa.2005.1644.

Olson, P., Driscoll, P., and Amit, H., 2009: Dipole collapse and reversal precursors in a numerical dynamo. *Phys. Earth Planet. Int.*, **173**(1-2), 121–140. doi:10.1016/j.pepi.2008.11.010.

Tauxe, L., and Yamazaki, T., 2007: Paleointensities. In *Geomagnetism*, editor M. Kono and G. Schubert, volume 5 of *Treatise on Geophysics*, 509–563. Elsevier, Amsterdam.

Thomson, D., 1982: Spectrum Estimation and harmonic analysis. *Proc. of the IEEE*, **70**(9), 1055–1096.

Valet, J., 2003: Time variations in geomagnetic intensity. *Reviews of Geophysics*, **41**(1). doi:10.1029/2001RG000104.

Valet, J. P., and Meynadier, L., 1993: Geomagnetic-field intensity and reversals during the past 4 million years. *Nature*, **366**(6452), 234–238.

Valet, J. P., Meynadier, L., and Guyodo, Y., 2005: Geomagnetic dipole strength and reversal rate over the past two million years. *Nature*, **435**(7043), 802–805. doi:10.1038/nature03674.

Zhang, K., and Gubbins, D., 2000: Is the geodynamo process intrinsically unstable? *Geophys. J. Int.*, **140**(1), F1–F4.

Ziegler, L. B., Constable, C. G., Johnson, C. L., and Tauxe, L., 2011: PADM2M: a penalized maximum likelihood model of the 02 Ma palaeomagnetic axial dipole moment. *Geophys. J. Int.*, **184**(3), 1069–1089. doi:doi: 10.1111/j.1365-246X.2010.04905.x.

Chapter 5

Regional paleointensity features in the 0-300 ka paleomagnetic field

5.1 Introduction

Earth's magnetic field is primarily that produced by an axial dipole: it is anti-symmetric about the equator, with field magnitude and direction varying with latitude. Field lines trace a path outward from one hemispherical pole and inward at the other, and intensity at the poles is double that at the equator. This fundamental pattern (see figure 5.1), along with observations of secular variation and occasional global reversals of polarity, informs our basic understanding of the field generation processes happening in the Earth's iron core.

In the modern field, the axial dipole component of the field (g_1^0) is almost six times larger than the next largest component of the field (Finlay et al., 2010). Yet, much of the modern field departs from the simple, global picture of an axial dipole field. These components can be described mathematically using the usual g_l^m and h_l^m coefficients of degree l and order m from a spherical harmonic expansion Ψ for the magnetic scalar potential with $\mathbf{B} = -\nabla\mathbf{\Psi}$. A specific length scale is

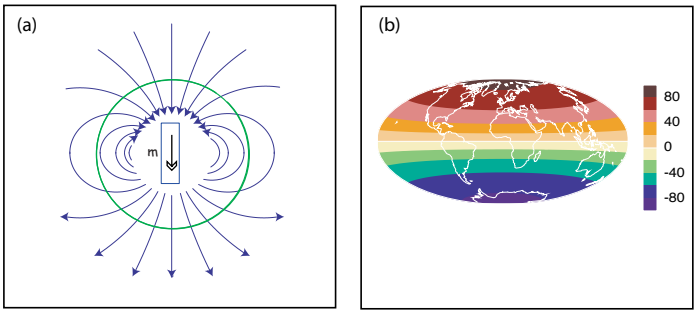

Figure 5.1: (a) Illustration of magnetic lines of force for a dipole field surrounding a bar magnet source. (b) Illustration of the vertical field component at the surface of the earth for an internal dipole source, with color contours showing field magnitude. Positive and negative values of denote lines of force pointing 'into' or 'out of' the surface respectively (see (a)). Adapted from (Tauxe, 2005), reproduced from Chapter 1

associated with each spherical harmonic degree: Jean's formula gives $\lambda = \frac{2\pi a}{(l+1/2)}$, where a is Earth's radius, and for $l \leq 15$ the field is dominantly from Earth's core. More broadly speaking, these components are called simply 'Non-Axial-Dipole' field or NAD field, and can be thought of as regional departures from an axial dipole field. Higher degree terms are dominated by crustal field contributions which are neglected here.

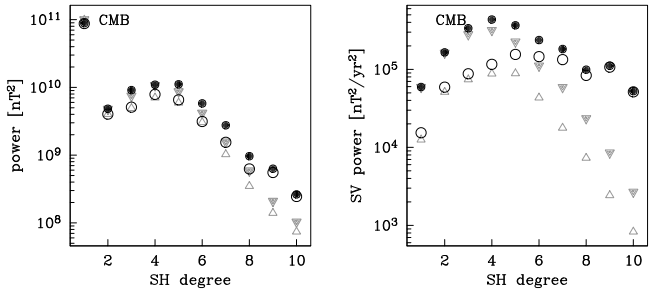

Figure 5.2: Geomagnetic main field (left) and secular variation (right) power spectra for the models CALS3k.3 (gray filled triangles), CALS3k.3b gray open triangles, CALS3k.4 (black dots) and CALS3k.4b (black circles). Reproduced from (Korte and Constable, Submitted)

NAD field features vary on a different timescale from the GAD (geocentric axial dipole) field as can be seen in figure 5.2. In time-varying models of the modern and historical field they are readily observed and mathematically described even at short length scales (e.g. the CHAOS-2 models based on satellite and observatory data include secular variation terms up to $l = 20$, and static terms to $l = 60$ (Olsen et al., 2009)). Data quality and availability from the ancient field limit our ability to describe fine scale regional departures from GAD beyond a few hundred years. However, millennial scale models which now extend to 10 ka (Korte et al., In Prep.) recover NAD field out to about degree 4 or 5 (length scales of $\lambda = \frac{2\pi a}{(l+1/2)}$, about 8,000 km).

These departures from GAD extend to million year time scales, with time-averaged field models mainly based on paleomagnetic directional data indicating that a GAD field does not fit the data as well as one with some NAD structure (Johnson and Constable, 1997; Gubbins and Kelly, 1995). Aubert et al. (2010) note in particular longitudinal structure in their model of Brunhes (0-780 ka) time averaged field. Archeomagnetic paleointensity data spanning the 0-3 ka interval show clear regional differences in time variations of virtual axial dipole moment (Genevey et al., 2008).

Much NAD structure on short timescales is highly variable, reflecting the dynamic non-linear processes generating the field. However, persistence of, or trends in, NAD features seen over long time scales in the time averaged field may reflect fundamental, long-term features of fluid flow in the core, such as effects of the solid inner core on flow (e.g. tangent cylinder effects), or core-mantle boundary conditions (Gubbins et al., 2007; Aubert et al., 2010).

Persistent NAD structure of the sort seen in time averaged field models should be visible in time-varying field models over tens of thousands to millions of years. However, because of limited data availability, typically on these time scales the GAD approximation has been invoked to produce time-varying reconstructions of axial dipole field strength based only on paleointensity data (Valet et al., 2005;

Channell et al., 2009; Ziegler et al., 2011). These studies have yielded significant insights into long term variations in the axial dipole field. However, some interesting features seen in the centennial and millennial models, such as recurring high latitude flux patches (Korte et al., In Prep.), cannot be investigated on paleo time scales from a simple GAD field reconstruction. Additionally, stratigraphic, tectonic, and environmental studies which rely on paleointensity assisted chronology as a dating tool could have more robust age constraints from a more geographically precise paleomagnetic reference field.

In an effort to better understand regional field features, the North Atlantic Paleointensity Stack (NAPIS) and the South Atlantic Paleointensity Stack (SAPIS) were created and illustrate composite axial dipole moment models made from a handful of relative paleointensity (RPI) time series geographically clustered in the north Atlantic ocean (NAPIS) and the south Atlantic ocean (SAPIS) (Laj et al., 2000; Stoner et al., 2002). A comparison of the 75 kyr long stacks by Stoner et al. (2002) found time spans of close agreement and others with distinct differences between the two stacks.

Investigations comparing the spectral coherence of individual relative paleointensity time series and stacks can be difficult due to the effects of age uncertainties in the data . Moderate age errors typical in RPI time series can supress the expected signal of systematic increase in coherence with decreasing geographical separation of core locations (McMillan et al., 2004). However, stacks or models made from several regionally clustered data can serve to reinforce strong moderate to long period signals.

Here we use regionally clustered relative paleointensity data sets and the modeling techniques developed in Ziegler et al. (2011) to construct geographically variable models of axial dipole moment. We look at subsets of the data divided by both latitude and longitude in an effort to isolate large-scale NAD features from global PADM variations.

5.2 Data & Methods

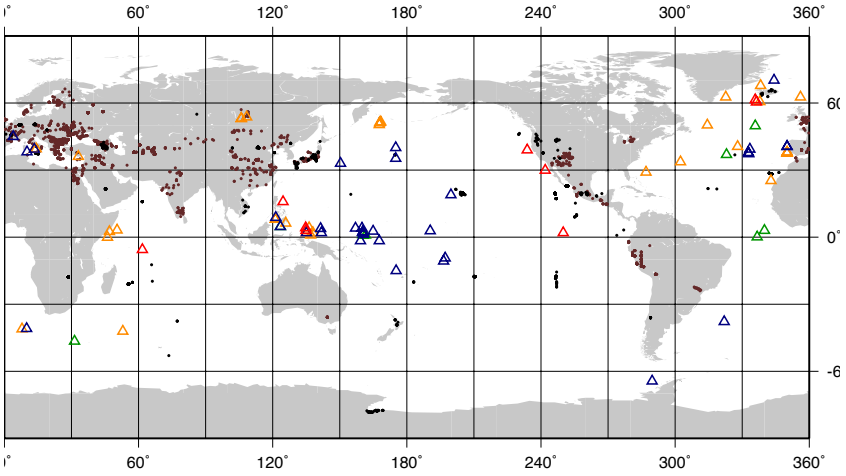

Figure 5.3: Geographic distribution of data used in PADM2M and this study. Small circles are for API data (brown for archeomagnetic data, black for igneous data). Triangles represent sediment cores color coded by age span: 0-2 Ma records (red), records which span several hundred kyr (blue), records which span between 0 and 200 kyr ago (yellow), and short Brunhes/Matuyama reversal records (green). Reproduced from Ziegler et al. (2011)

The data and methods used in this work are described in Ziegler et al. (2011), and are summarized briefly here. We work with a compilation of 86 RPI records from (Tauxe and Yamazaki, 2007), and absolute paleointensity data from PINT08 (Biggin et al., 2009) and the Geomagia50.v2 database (Donadini et al., 2009) that span the age range 0–2 Ma. The modeling technique is a penalized maximum likelihood method and has previously been used to construct a time varying paleomagnetic axial dipole field moment parameterized by cubic B-splines, using the joint set of absolute paleointensity data and RPI time series. Whereas in the creation of PADM2M the model was fit to the entire RPI set (except for a few incompatible time series), here we fit PADM models to RPI data from restricted geographic regions. The RPI time series are anywhere from tens of thousands to millions of years long and are spread across the globe (see figure 5.3, reproduced from Ziegler et al. (2011) for global distribution of data). Each regional model uses only a subset of the global RPI compilation, and the sparse data distribution

presents some difficulties. We fit regional models to the time span in which a minimum of five RPI records are present at all times. With this criterion, all (except one) of the regions considered below have sufficient RPI data for modeling back to approximately 300 kyr ago. We therefore limit our study to this age range.

In all regional models, we include the entire global absolute paleointensity data which provide the basic calibration for magnitude of the regional axial dipole moment (RADM). Data availability made it impractical to use regionally clustered absolute paleointensity data for each selection of regionally clustered RPI data. However, the RPI time series contribute significantly more data than the absolute paleointensity data set, so the model is primarily constrained by those data.

5.2.1 Latitudinal Bands

We initially divided the global RPI set into 3 latitudinal bands for separate RADM reconstructions. The first extends nominally from 25 to 90 degrees latitude. 40 records fall into this category and in practice, span latitudes of 25 to 70 degrees, generating our Mid-High Latitude RADM. The next band is designated Equatorial and nominally extends from +25 to -25 degrees latitude. It contains 40 RPI records, which are actually confined to a band from -15 to +20 degrees latitudes. A third band stretches from -25 to -90 degrees latitude. However, in this southern hemisphere mid- to high latitude band there is no point where 5 RPI time series overlap, and we therefore refrain from modeling the region.

5.2.2 Longitudinal Bands

The global data set is separately divided into 3 regions based on RPI core longitudinal location. These regions are nominally 0-90, 90-270, and 270-360 degrees longitude, and roughly correspond to the Indian, Pacific, and Atlantic oceans respectively. The 0-90 degree longitude region has the sparsest coverage, with a maximum of 12 records in the 0-187 ka span and fewer than 5 beyond that interval. The Pacific has 45 records and enough data to supply more than 5

records at any given time well beyond 300 ka, but we plot only to this age to be comparable to the other longitudinal bands. The Atlantic region has more than 5 records for all times between 0-283 ka, and comprises 21 total records.

5.3 Results

The resulting RADM models are shown in figures 5.4 and 5.5. Figure 5.4 shows the two models made from latitudinal bands of RPI data along with the number of RPI cores contributing to the model for each age. Model uncertainties are calculated using a delete-1 jacknife routine, and are shown as the shaded area surrounding each RADM model. The models look quite similar, especially for 0-180 ka - the RMS value of the difference between models is $10.0 ZAm^2$ for 0-180 ka and $14.1 ZAm^2$ for 180-300 ka. We plot the difference between the models at each age explicitly in figure 5.6. Some lows (for instance, at 180 ka) tend to be lower in the mid- to high latitude band than the equatorial region. On average, the equatorial region has slightly higher intensity, with a mean difference of $6.3 ZAm^2$. The equatorial region is missing a small paleointensity low at about 120 ka, and shows a different shape for the broad paleointensity low at around 180 ka. In the long period signals, there is general agreement between models.

The three longitudinal RADM models are shown in figure 5.5. The model covering 0-90 degrees longitude (here loosely categorized as the 'Indian Ocean' region) is constructed from the lowest number of RPI cores, and has a low resolution due to the data quantity. The Pacific and Atlantic RADMs have resolutions more similar to each other; uncertainties for these, shown as the shaded area around each model, are again calculated for these from delete-1 jacknife routines. They agree with the broad trends of the Indian ocean regional model, but show many areas of disagreement with each other. The longitudinal regions have more pronounced differences than the latitudinally grouped models, as discussed in further detail in the next section. In figure 5.6 we see the difference between the Pacific

and Atlantic regions (regions 5 and 6 respectively) has larger variance. The RMS of the difference between these two regions is $12.2ZAm^2$ over the 283 ka they overlap, compared to an RMS of $11.6ZAm^2$ for the difference between the latitudinal models in this time range, despite the fact that the mean difference between the longitudinal regional models ($4.8ZAm^2$) is less than the mean difference between the latitudinal regions.

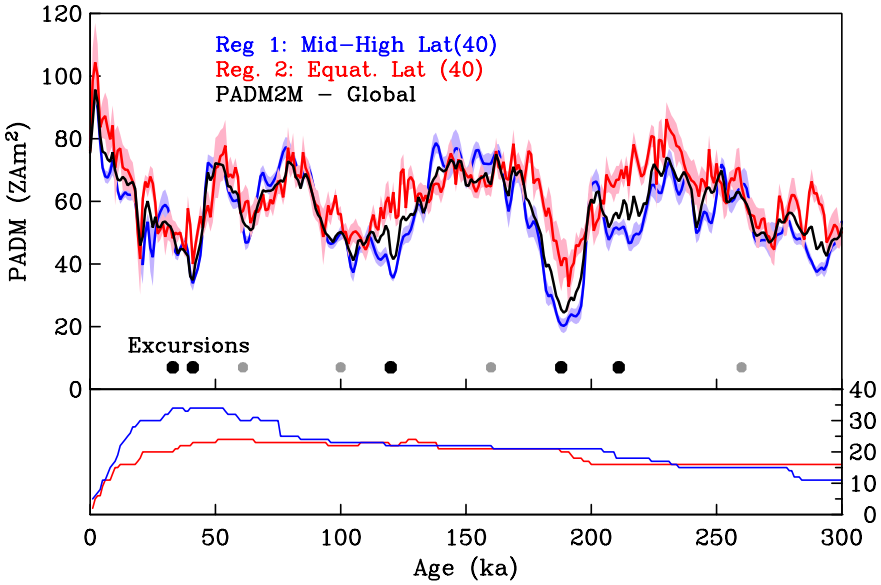

Figure 5.4: Regional Axial Dipole Moment models: Latitude bands. (Top) RADM models from mid- to high- latitude RPI data (blue) and equatorial latitude data (red), along with the PADM2M model. Shaded region surrounding each RADM model represents $\pm 2\sigma$ estimated from a delete-1 jacknife routine. Globally observed excursions (black circles) and additional excursions (gray circles) are marked at their estimated ages. (Bottom) Number of RPI records available for each latitudinal model (colors correspond to top plot).

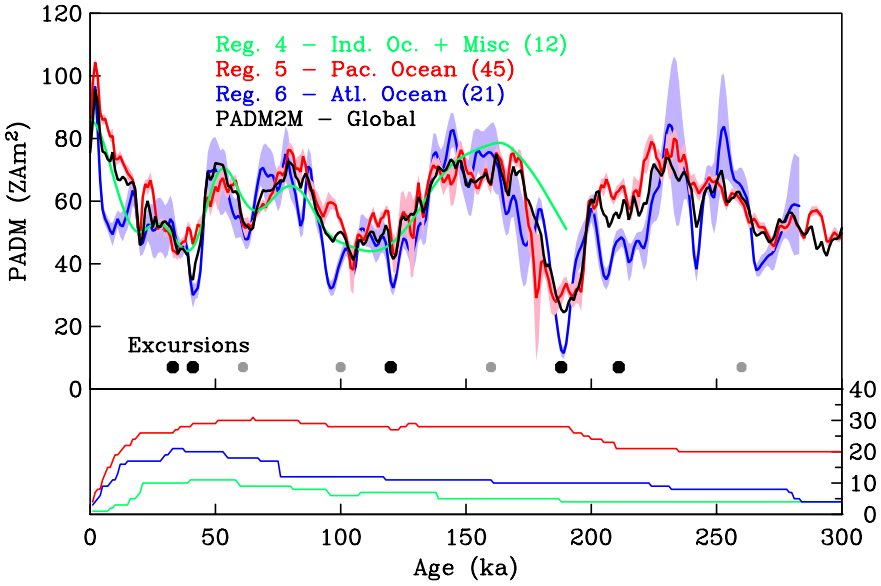

Figure 5.5: Regional Axial Dipole Moment models: Longitude bands. (Top) RADM models from Atlantic ocean longitude RPI data (blue), Pacific ocean longitude RPI data (red) and Indian ocean longitude RPI data (green) along with the PADM2M model. Shaded region surrounding the Pacific and Atlantic RADM models represents $\pm 2\sigma$ estimated from a delete-1 jacknife routine. Globally observed excursions (black circles) and additional excursions (gray circles) are marked at their estimated ages. (Bottom) Number of RPI records available for each latitudinal model (colors correspond to top plot).

5.4 Discussion

5.4.1 Statistics for Comparisons between Regions

Table 5.1 summarizes some statistical information for each regional model along with the global 0-2 Ma PADM2M model and the most recent 300 kyr of PADM2M, including the mean, standard deviation, minimum and maximum paleomagnetic axial dipole moment. By comparison to 2 Myr of paleointensity variations, the 300 kyr models show similar variability, which indicates they capture the general spectrum of paleosecular variation of field strength, despite the lack of reversals in this age range. The minimum of PADM2M is lower than the regional models though, and corresponds to a reversal outside the 0-300 ka range.

The differences between longitudinal regions are slightly more pronounced

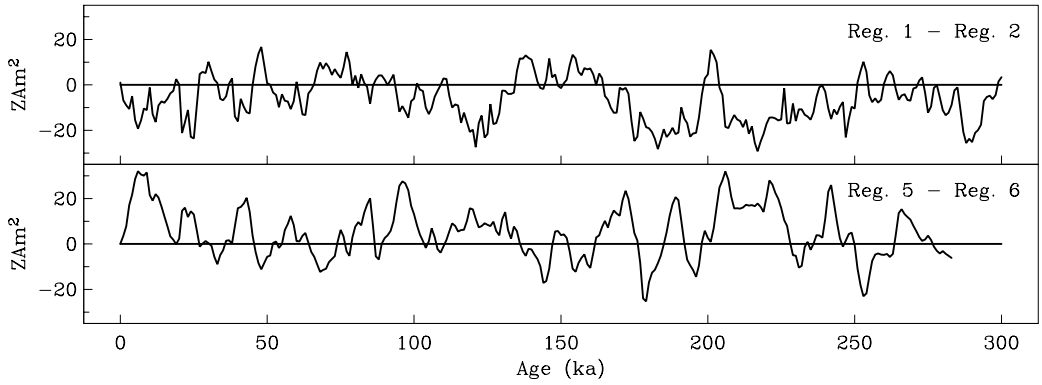

Figure 5.6: (Top) Difference between regions of different latitude ranges (Reg. 1 - Mid-High & Reg. 2 - Equatorial). (Bottom) Difference between Reg. 5 and Reg. 6 - the Pacific and Atlantic longitudinal regions.

than between the latitudinal regions (fig. 5.4 and table 5.1). The Atlantic longitudinal region shows the most variability, which is apparent both from visual observation and statistical calculations shown in table 5.1. PISO-1500, a global stack of RPI data which heavily drew from Atlantic records, has greater variability than other reconstructions of global axial dipole moment variations e.g (Valet et al., 2005; Ziegler et al., 2011), which are not as reliant on Atlantic records. The RADM here, made with the same algorithm as PADM2M using only different RPI data, suggests the difference in variability between PISO-1500 and other global axial dipole moment models is at least partially due to the regional biases of datasets going into the separate models. Alternatively, the higher variability could be in part due to the smaller number of records used in the Atlantic region. Future work will involve bootstrap analysis on each regional model for estimates of uncertainties. If uncertainties are on par with those for the global model (see Chapter 3), the higher variability is likely not entirely an artifact of the smaller number of data. Also, the Atlantic region is lower on average than the Pacific region, as mentioned in the Results section. Some previous literature has noted many regions

Table 5.1 Statistics of 0-300 ka in the regional models

0-300 ka:	Mean	Std	Min	Max
Reg. 1 (Mid-High Lat)	56.1	13.7	20.1	95.4
Reg. 2 (Equat. Lat)	62.3	10.9	32.8	104.4
Reg. 4 (Ind. Oc.)*	60.3	11.3	44.1	86.2
Reg. 5 (Pac. Oc.)	59.7	12.5	27.8	104.4
Reg. 6 (Atl. Oc.)**	55.2	14.4	11.5	96.6
PADM2M	57.7	11.4	24.5	95.7
0-2 Ma:				
PADM2M	53.2	14.8	10.7	95.7

Table 5.1: Statistics of 0-300 ka in the regional models discussed in this study along with PADM2M of Ziegler et al. (2011). * Ind. Ocean regional model extends only to 187 ka. ** Atl. Ocean regional model extends only to 283 ka. All units in ZAm^2

of the Pacific having higher VADMs on average over 0-20 ka, consistent with what we see here (Genevey et al., 2008).

5.4.2 Excursions

No reversals occur in the 0-300 ka time frame, but extreme lows in paleointensities are nonetheless present. Many correspond to directional excursions. Excursions are defined as brief ($< 10^4$ kyr) periods of extreme deviation of Virtual Geomagnetic Poles from GAD poles. The details of the cutoff between normal paleosecular variation in field directional data and excursional behavior is not standardized. Generally they are defined either as periods when virtual geomagnetic pole latitudes are less than 45^o or when they are fully reversed for a few thousand years (Laj and Channell, 2007). Excursional field events are hard to understand, in part because of the lack of precise definition, and relatedly, because no event seems exactly like another. Some events, such as the Laschamp, are well documented and present in many globally distributed RPI cores (Laj and Channell, 2007). Others are recorded in only a few locations, indicating the excursional event could be a regional field feature. Some studies indicate that excursions can be thought of as 'failed' reversals, indicating that they share similar generational

mechanisms, but with a failure of the field to stabilize in the reversed direction, instead returning to its original polarity (see e.g. (Hoffman, 1981)). Globally observed excursional events lend support to the idea that excursions are linked to reversals (another global phenomenon) at some level. However, excursions that are seen only in a few locations are more ambiguous: they might be global but too short for detection, or simply examples of very strong regional paleosecular variations, perhaps part of a continuum linking secular variations to reversals. Support for this comes from Ziegler and Constable (Submitted), who established a broad link between excursions and reversals. They evaluated long period oscillations seen in paleosecular variation, finding that a subtle version of the 'sawtooth' pattern (Valet and Meynadier, 1993) of slowly decaying field strength and comparably faster field growth existed throughout the excursion filled Brunhes chron and the reversal filled Matuyama chrons. Previously, such asymmetry in growth and decay had only been visually assessed and correlated exclusively to field reversals.

In figures 5.4 and 5.5 we have labeled excursions identified in the literature. Laj and Channell (2007) summarize compilations of excursions from a multitude of individual RPI cores and compilations and establish a set of well documented excursions with good age controls. In the past 300 kyr, there are 5: Mono Lake (33 ka), Laschamp (41 ka), Blake (120 ka), Iceland Basin (188 ka), and Pringle Falls (211 ka). These are indicated with black dots on the figures. Other, less certain excursions have been documented to a lesser extent, as mentioned in (Laj and Channell, 2007). These could be regional features, or events short enough that their signal was not clear through the natural filtering effects of the remanent magnetization recording process at most locations. In figures 5.4 and 5.5 we mark with gray dots additional excursions as listed in a recent compilation by Lund et al. (2006), to include the broadest set of 0-300 ka excursions.

Our RADM models do show some differences in their recording of excursions. The Laschamp event is clearer in the Atlantic longitudinal band with a much more pronounced low than the other longitudinal regions. This agrees with

other studies that also model the field with a more pronounced minimum in the Atlantic (Leonhardt et al., 2009). Regional differences in our results are apparent for other excursions, notably the Iceland basin event (190 ka). The Iceland basin event corresponds to a clear, sharp low in paleointensity in the Atlantic, but a broad low in the Pacific. This could reflect field dynamics, as suggested with the regional differences in the Laschamp event. Alternatively, the broad low in our model of a compilation of RPI cores could occur if age control issues led to misalignment of the low between records. However, there is no reason to suspect this time interval had particularly bad age controls in contrast to the rest of the model, where the Pacific model often has highs/lows of comparable width to the Atlantic model (though not neccessarily comparable amplitude).

Finally we note that our regional models have some distinct field intensity lows which do not correspond to known field excursions.

5.5 Conclusions

In our regional analysis of relative paleointensity data, we find that there is a clearer regional signal across models made from longitudinally grouped RPI data than latitudinally grouped data. The long period behavior across all models is very similar, but regional differences in RPI recorded are clearly present in the composite regional models, especially at periods of known excursional events. The Atlantic region has somewhat larger variability than others, with a very pronounced minimum during the Iceland basin excursional event. Departures from the GAD field are clearly observed through comparison of regional paleomagnetic axial dipole moment models.

References

Aubert, J., Tarduno, J. A., and Johnson, C. L., 2010: Observations and Models of the Long-Term Evolution of Earth's Magnetic Field. *Space Science Reviews*, **155**(1-4), 337–370. doi:10.1007/s11214-010-9684-5.

Biggin, A., Strik, G., and Langereis, C., 2009: The intensity of the geomagnetic field in the late-Archaean: new measurements and an analysis of the updated IAGA palaeointensity database. *Earth Planets and Space*, **61**(1), 9–22.

Channell, J. E. T., Xuan, C., and Hodell, D. A., 2009: Stacking paleointensity and oxygen isotope data for the last 1.5 Myr (PISO-1500). *Earth Planet. Sci. Lett.*, **283**(1-4), 14–23. doi:10.1016/j.epsl.2009.03.012.

Donadini, F., Korte, M., and Constable, C. G., 2009: Geomagnetic field for 0-3 ka: 1. New data sets for global modeling. *Geochem. Geophys. Geosyst.*, **10**, Q06007, 10.1029/2008GC002295. doi:10.1029/2008GC002295.

Finlay, C. C., Maus, S., Beggan, C. D., Bondar, T. N., Chambodut, A., Chernova, T. A., Chulliat, A., Golovkov, V. P., Hamilton, B., Hamoudi, M., Holme, R., Hulot, G., Kuang, W., Langlais, B., Lesur, V., Lowes, F. J., Luehr, H., Macmillan, S., Mandea, M., McLean, S., Manoj, C., Menvielle, M., Michaelis, I., Olsen, N., Rauberg, J., Rother, M., Sabaka, T. J., Tangborn, A., Toffner-Clausen, L., Thebault, E., Thomson, A. W. P., Wardinski, I., Wei, Z., Zvereva, T. I., and Int Assoc Geomagnetism Aeronomy Wo, 2010: International Geomagnetic Reference Field: the eleventh generation. *Geophys. J. Int.*, **183**(3), 1216–1230. doi:10.1111/j.1365-246X.2010.04804.x.

Genevey, A., Gallet, Y., Constable, C. G., Korte, M., and Hulot, G., 2008: ArcheoInt: An upgraded compilation of geomagnetic field intensity data for the past ten millennia and its application to the recovery of the past dipole moment. *Geochem. Geophys. Geosyst.*, **9**. doi:10.1029/2007GC001881.

Gubbins, D., and Kelly, P., 1995: On the analysis of paleomagnetic secular variation. *J. Geophys. Res.- Solid Earth*, **100**(B8), 14955–14964.

Gubbins, D., Willis, A. P., and Sreenivasan, B., 2007: Correlation of Earth's magnetic field with lower mantle thermal and seismic structure. *Phys. Earth Planet. Int.*, **162**(3-4), 256–260. doi:10.1016/j.pepi.2007.04.014.

Hoffman, K., 1981: Paleomagnetic excursions, aborted reversals and transitional fields. *Nature*, **294**, 67–69.

Johnson, C., and Constable, C., 1997: The time-averaged geomagnetic field: global and regional biases for 0-5 Ma. *Geophys. J. Int.*, **131**(3), 643+.

Korte, M., and Constable, C. G., Submitted: Improvements to millennial geomagnetic field reconstructions. *Phys. Earth Planet. Int.*

Korte, M., Constable, C. G., F., D., and Holme, R., In Prep.: Reconstructing the Holocene Geomagnetic Field. *Earth Planet. Sci. Lett.*

Laj, C., and Channell, J. E. T., 2007: Geomagnetic excursions. In *Geomagnetism*, editor M. Kono and G. Schubert, volume 5 of *Treatise on Geophysics*, 373–416. Elsevier, Amsterdam.

Laj, C., Kissel, C., Mazaud, A., Channell, J. E. T., and Beer, J., 2000: North Atlantic palaeointensity stack since 75 ka (NAPIS-75) and the duration of the Laschamp event. *Phil. Trans. Roy. Soc. Lond.*, **358**(1768), 1009–1025.

Leonhardt, R., Fabian, K., Winklhofer, A., M.and Ferk, Laj, C., and Kissel, C., 2009: Geomagnetic field evolution during the Laschamp excursion. *Earth Planet. Sci. Lett.*, **278**(1-2), 87–95. doi:10.1016/j.epsl.2008.11.028.

Lund, S., Stoner, J. S., Channell, J. E. T., and Acton, G., 2006: A summary of Brunhes paleomagnetic field variability recorded in Ocean Drilling Program cores. *Phys. Earth Planet. Int.*, **156**(3-4), 194–204. doi: 10.1016/j.pepi.2005.10.009.

McMillan, D. G., Constable, C. G., and Parker, R. L., 2004: Assessing the dipolar signal in stacked paleointensity records using a statistical error model and geodynamo simulations. *Phys. Earth Planet. Int.*, **145**(1-4), 37–54. doi: 10.1016/j.pepi.2004.02.011.

Olsen, N., Mandea, M., Sabaka, T. J., and Toffner-Clausen, L., 2009: CHAOS-2-a geomagnetic field model derived from one decade of continuous satellite data. *Geophys. J. Int.*, **179**(3), 1477–1487. doi:10.1111/j.1365-246X.2009.04386.x.

Stoner, J. S., Laj, C., Channell, J. E. T., and Kissel, C., 2002: South Atlantic and North Atlantic geomagnetic paleointensity stacks (0-80 ka): implications for inter-hemispheric correlation. *Quaternary Science Reviews*, **21**(10), 1141–1151.

Tauxe, L., 2005: Lectures in Paleomagnetism. *http://earthref.org/MAGIC/books/Tauxe/2005/*.

Tauxe, L., and Yamazaki, T., 2007: Paleointensities. In *Geomagnetism*, editor M. Kono and G. Schubert, volume 5 of *Treatise on Geophysics*, 509–563. Elsevier, Amsterdam.

Valet, J. P., and Meynadier, L., 1993: Geomagnetic-field intensity and reversals during the past 4 million years. *Nature*, **366**(6452), 234–238.

Valet, J. P., Meynadier, L., and Guyodo, Y., 2005: Geomagnetic dipole strength and reversal rate over the past two million years. *Nature*, **435**(7043), 802–805. doi:10.1038/nature03674.

Ziegler, L. B., and Constable, C. G., Submitted: Asymmetry in growth and decay of the geomagnetic dipole. *Earth Planet. Sci. Lett.*

Ziegler, L. B., Constable, C. G., Johnson, C. L., and Tauxe, L., 2011: PADM2M: a penalized maximum likelihood model of the 02 Ma palaeomagnetic axial dipole moment. *Geophys. J. Int.*, **184**(3), 1069–1089. doi:doi: 10.1111/j.1365-246X.2010.04905.x.

Chapter 6

Concluding Remarks and Future Outlook

This body of work features novel analytical methods for exploring in depth the growing collection of paleomagnetic field intensity data. Through the use of a unique bootstrap resampling technique which accommodates uneven temporal distribution of the data, a mean VADM for 0-1 Ma was estimated. I also found that paleointensities derived from archeologic objects and igneous samples differed by 10-15% on average. In further work, such as the creation of PADM2M in chapter 3, we treated both sources of paleointensities as reliable, but considered them as two distinct data compilations with different statistical properties.

The PADM2M model represents the best global picture to date of axial dipole moment variations over the last two million years. While earlier, comparable efforts stacked and averaged RPI data to build a composite model, PADM2M is the first model made using inverse methods. Advances in this regard are the ability of the new algorithm to incorporate both absolute and relative paleointensities into the resulting model, and the use of robust methods of estimation for a less biased result. Additionally, PADM2M is continuous and twice differentiable, allowing users to evaluate the model and its first and second derivative at any specified time. While reference models of axial dipole moment are useful for a variety of

applications including chronostratigraphy and exposure dating, this dissertation focuses on the implications of ADM variations for geodynamo processes. In chapter 4 through the evaluation of PADM2M derivatives we look in detail at growth and decay in the magnetic field strength on a variety of timescales. The subtle, distinct statistical differences between growth and decay rates led to firm support for connecting excursional and reverse events as part of a continuum of paleosecular variation.

I look beyond the axial dipole in chapter 5 and explore regional features in paleomagnetic field strength. While the signature long-period axial dipole variations are present in all regions, some moderate to large scale differences are clear. Understanding whether those difference reflect non-axial dipole signal, or are an artifact of errors and uncertainties in the data is an active area of investigation.

I expect and hope that the PADM2M model will serve as a useful reference tool for many paleomagnetic applications. Additionally, the associated algorithm developed to create it and the RADM models of chapter 5 can be incorporated into future modeling. The algorithm can be used to create PADM and RADM models on a variety of timescales for global or regional datasets with a flexible variety of resolutions (depending on the data). Pieces of the algorithm, such as the penalized maximum likelihood inversion with included parametric fitting of required pdf functions can be adapted for use in other geomagnetic models involving time-variations.

The research into RADM models in chapter 5 suggests many potential follow up studies. A useful place to start, for instance, would be creating higher resolution models RADM models spanning 0-40 ka, where data coverage is better than for older ages. These models would overlap with and have comparable temporal resolution to Holocene magnetic field models which describe the non-axial-dipole field, allowing for informative comparisons.